Towards On-demand Generation of Entangled Photons with Quantum Dots

by

Arash Ahmadi

A thesis
presented to the University of Waterloo
in fulfillment of the
thesis requirement for the degree of
Doctor of Philosophy
in
Physics (Quantum Information)

Waterloo, Ontario, Canada, 2019

Examining Committee Membership

The following served on the Examining Committee for this thesis. The decision of the Examining Committee is by majority vote.

External Examiner:	Mete Atatüre Professor, Dept. of Physics , University of Cambridge
Supervisor(s):	Michael E. Reimer Assistant Professor, Dept. of Electrical & Computer Engineering, University of Waterloo
	Thomas Jennewein Associate Professor, Dept. of Physics & Astronomy, University of Waterloo
Internal Member:	Kevin Resch Professor, Dept. of Physics & Astronomy, University of Waterloo
Internal Member:	Michal Bajcsy Assistant Professor, Dept. of Electrical & Computer Engineering, University of Waterloo
Internal-External Member:	Christopher Wilson Professor, Dept. of Electrical & Computer Engineering, University of Waterloo

I hereby declare that I am the sole author of this thesis. This is a true copy of the thesis, including any required final revisions, as accepted by my examiners.

I understand that my thesis may be made electronically available to the public.

Statement of Contributions

For acheiving the results presented in this thesis several people have been involved. Andreas Fognini led the project of measuring dephasing-free entanglement in nanowire quantum dots, **Chapter** 3. Under his leadership, we built the experimental setup and developed the software for controlling the measuring apparatus. The measurements were performed with the help from Mohd Zeeshan. The theoretical model was developed by A. Fognini, and together we analyzed the measurement results. The initial idea behind the proposed approach for erasing the fine-structure splitting of quantum dots, **Chapter** 5, was from A. Fognini, and together we developed the mathematical calculations, as well as, the discussion and analysis of the obtained results.

The resonant two-photon excitation scheme, **Chapter** 4, was performed together with Morgan Mastrovich and with contributions from Sara Hosseini. M. Mastrovich and I were involved in performing the measurements and analysis of the results. Klaus D. Jöns should be mentioned for his guidance at different stages, from building the experimental setup to analysis of the results. Moreover, Jeff Salvail should be noted for his contribution in building the 4f pulse shaper.

Abstract

The biexciton-exciton cascade in quantum dots (QDs) yields entangled photon pairs, and recent developments in engineering photonic structures around the dot for efficient light extraction and proper control of the fine-structure splitting, has led to significant breakthroughs in achieving an ideal entangled photon source – exhibiting properties such as high extraction efficiency, low multi-photon emission and high entanglement fidelity. This thesis presents our development in enhancing the performance of entangled photon generation of QDs towards near-unity efficiency and fidelity. We study InAsP quantum dots in photonic nanowires for efficient light extraction and to reveal the effect of a quantum dot with high nuclear spin on the entanglement fidelity.

Revealing the ultimate limit of entanglement in QDs is still a challenge, and it is generally believed that a sample made of atoms possessing high nuclear spins exhibits limited entanglement due to the dephasing caused by spin-spin interactions. Moreover, it is assumed that the fine-structure splitting of QDs degrades the entanglement fidelity, as it introduces a which-path information in the biexciton-exciton cascade. We have performed two-photon state tomography on InAsP QDs in InP nanowires, comprising of nuclear spin 9/2, and have realized that such a source is capable of generating entangled photon pairs with negligible dephasing during the emission lifetime, with a peak concurrence $\mathcal{C} = 77\%$ and a count-weighted average concurrence $\bar{\mathcal{C}} = 62\%$. This result was obtained by comparing the outcome of our measurements with a theoretical model that assumes no dephasing, however, takes into account the details of the detection system, i.e., dark-count rates and timing resolution, as well as, specific features of the QD, e.g., emission lifetime, fine-structure splitting, multi-photon emission probability, etc. Proper engineering of tapered nanowires allows for extraction of the emitted photons with high efficiency, which makes it possible to perform a complete two-photon state tomography and monitoring the evolution of the exciton state, as well as, the entanglement fidelity of the photon-pair, during the emission lifetime. This enabled us to reveal the effect of an imperfect detection system, as well as, multi-photon emission in recording low values for entanglement fidelity. Moreover, our calculations show that proper analysis of the time-energy uncertainty relation provides

the necessary means to measure a high entanglement fidelity even in the presence of fine-structure splitting; since, a detection system with high timing resolution can overlook the which-path information, as the uncertainty in measuring the energy of the photons will be larger than the fine-structure splitting. Therefore, realizing near-unity entanglement fidelity using QDs is merely a technical challenge, i.e., resonant excitation of the QD, in order to suppress multi-photon emission, and use of a detection system with low timing jitter and dark-count rates.

As a next step to achieve this goal, we have performed the resonant two-photon excitation scheme for the first time on a QD in a photonic nanowire, which resulted in an enhancement of the performance of our source. We managed to improve the single-photon purity of the source, $g^{(2)}(0)$, by two orders of magnitude; moreover, analysis of the emission spectrum reveals that this scheme increases the pair-production efficiency to values above 93% for the biexciton-exciton cascade. Taking the efficiency of our experimental setup into consideration, the results indicate an approximately eight-fold enhancement of the pair-extraction efficiency as compared to the quasi-resonant excitation scheme (12.55% vs. 1.6%). Based on these results, two-photon state tomography on our source, under resonant two-photon excitation and performed by a detection system with high timing resolution and low dark-count rates, yields near-unity entanglement fidelity. By considering the enhancement in pair-extraction efficiency that we obtained, QDs in photonic nanowires can surpass the performance of spontaneous parametric down conversion sources in terms of entanglement fidelity and pair-extraction efficiency.

Even though we have shown a finite fine-structure splitting does not degrade the entanglement fidelity in QDs, for various application in quantum information removing the fine-structure splitting is beneficial. Therefore, we have proposed a universal all-optical approach for removing the fine-structure splitting. In this scheme, the energy of the photons are shifted by using a pair of quarter-wave plates and fast-rotating half-wave plates after they have been emitted; and as a result, the energy difference between the two decay paths in the biexciton-exciton cascade is erased. This method is applicable to any QD source and can be easily implemented using the currently available technology; moreover, no further sample processing will be required in order to achieve zero fine-structure splitting.

Acknowledgements

I would like to acknowledge all the people who have helped me through my PhD studies. First of all, I should thank Dr. Michael E. Reimer for his perfect insight and valuable supervision. His supportive and positive attitude towards research, creates a warm environment suitable for learning and scientific collaboration. I am truly grateful for all of his support. I should also thank Andreas Fognini for his guidance and leadership. His attitude towards research taught me a great deal, and helped me to become a better researcher. I have to thank Morgan Mastrovich for being an understanding and positive lab partner, and making our research a joyful experience. I would also like to thank all the other, current and past, members of the Quantum Photonics Devices Lab for creating a welcoming and warm environment, and contributing to my work through their fruitful scientific discussions: Mohd Zeeshan, Nachiket Sherlekar, Simon Daley, Burak Tekcan, Bradly van Kasteren, Michael Kobiersky, Sara Hosseini, Lin Tian and Divya Bharadwaj, and Sandra Gibson. I should also mention all the great people whom I met by joining IQC, whose presence has created unforgettable memories, specially Jose de Ramon Rivera, Jùlia Amorós Binefa, and Maria Papageorgiou.

I should also thank all of my friends outside of IQC; specially the members, both current and past, of **The Foundation for Safekeeping and Distribution of Golvazhe**, whose humours make living in tough times bearable: Erfan Meskar (Golkar), Amir Masoud Khezrian (Amir Shams), Hamed Dashtpeyma (Dappashi), Mohsen Rafiee, Hadi Meshgi (Agha Meshgi), Sajad Salmanipour, and Mohsen Rahmani. Also, I should mention my friends in **Partov Cultural Club**, whose presence can make a city, as dead as Waterloo, feel like home: Neda Ensafi (Pilgrim), Pouneh Torabian and Ali Mostolizadeh.

Last but not least, I have to thank my family, specially my mother Vida, for their presence and support.

Dedication

This is dedicated to my family and friends.

Table of Contents

List of Figures

List of Tables

List of Abbreviations

APD Avelanch Photodiode

CB Conduction Band

e electron

FSS Fine-structure Splitting

h hole

HBT Hanbury Brown-Twiss

hh heavy-hole

MFD Mode Field Diameter

PL Photoluminescence

QD Quantum Dot

SMF Single-mode Fiber

SPDC Sontaneous Parametric Down Conversion

TPE Two-photon Excitation

VB Valence Band

List of Publications

1. A. Fognini, A. Ahmadi, M. Zeeshan, J. T. Fokkens, S. J. Gibson, N. Sherlekar, S. J.Daley, D. Dalacu, P. J. Poole, K. D. J ons, V. Zwiller, and M. E. Reimer. Dephasingfree photon entanglement with a quantum dot. ACS Photonics, 6(7):1656–1663, 2019.

2. M. Zeeshan, N. Sherlekar, A. Ahmadi, R.L. Williams, and M.E. Reimer. Proposed-Scheme to Generate Bright Entangled Photon Pairs by Application of a Quadrupole-Field to a Single Quantum Dot.Phys. Rev. Lett., 122(22):227401, 2019.

3. A. Fognini, A. Ahmadi, S. J. Daley, M. E. Reimer, and V. Zwiller. Universal finestructure eraser for quantum dots.Opt. Express, 26(19):25–28, 2017.

Chapter 1

Introduction

Photons can be easily manipulated and have negligible interaction with the environment [1]; thus, realization of entangled photon pairs has allowed for conduction of various experiments in quantum foundations [2, 3, 4, 5], quantum communication [6, 7], quantum key distribution [8, 9], and linear-optic quantum computing [10, 11]. Besides, photons are, in principle, capable of encoding infinite amount of information in different forms such as polarization, temporal and spatial modes [12]. Hence, engineering of high-quality entangled-photon sources has become one of the main goals of the quantum community.

1.1 Early Steps

The first successful realization of an entangled photon-pair source [13], used cascade transition of atoms. This achievement opened up new doors in quantum optics, including the very first tests of Bell-type inequalities [14, 15]. However, such sources exhibited a low photon generation efficiency, $\epsilon \sim$ E-10 [15], and their emission was governed by the density and transition times, $\tau \approx 5$ns [15], of the atoms which could not be controlled [1, 16].

A major breakthrough came about by the introduction of spontaneous parametric down conversion (SPDC) sources [17, 18, 19]. Shining a coherent laser on a non-linear crystal can

lead to absorption of a photon, and generation of a pair of photons, idler and the signal, with lower energies, according to conservation of energy and momentum. The emitted photons are strongly correlated in time, and exhibit high fidelity in polarization entanglement; also, detection of the idler photon can turn the signal photon into a heralded single-photon. For these reasons, such sources remained as the back-bone of experiments in quantum optics for decades [1]. However, SPDC sources suffer from some fundamental drawbacks which limit their applicability for quantum communication purposes. The number of photon-pairs generated per mode follows a thermal distribution during the coherence time of the photons and then a Poisson distribution for longer time scales [20]; this means that in order to keep the source operating at high single-photon purity and avoid emission of more than one photon-pair per excitation pulse, one has to use low intensity pulses resulting in extremely low efficiencies, i.e., pair-generation probability $p < 1\%$ per excitation pulse [21].

1.2 State-of-the-Art

There are certain features that we can attribute to an ideal entangled photon source:

- High entanglement fidelity: emitted photons should be entangled with near-unity entanglement fidelity;
- Single-photon purity: one, and only one, photon should be emitted in each emission mode;
- On-demand generation: excitation of the source and collection of the emitted photons should be possible with 100% efficiency;
- High brightness: high rates of photon-pairs are necessary in order to overcome noise from the environment;
- Coherence: each mode of the emitted photons should be monochromatic with no inhomogeneous broadening, i.e., Fourier-limited photons;

- Tunability: in order to interfere photons from different sources, e.g., for entanglement swapping, each emitter should be tunable separately;
- Gaussian emission mode: for efficient coupling to optical fibers, emitted photons should have a Gaussian emission mode;
- Indistinguishability: for performing quantum protocols, the successive photons in each emission mode should be indistinguishable, i.e., successive photons should exhibit the same energy, linewidth, coherence length, etc.;
- Compatibility with integrated photonics: a feature necessary for performing quantum computing on a chip.

To overcome the probabilistic generation process of SPDC and thus avoid multiphoton emission there has been extensive research in engineering on-demand entangled photon sources based on semiconductor quantum dots. These quantum dot based sources exhibit features closest to an ideal entangled photon source [16]; however, reaching near-unity entanglement fidelity and efficiency has remained elusive. The very first such sources developed were self-assembled QDs [22], which have been shown to generate pairs of entangled photons [23]. However, self-assembled QDs suffer from an extremely low light extraction efficiency since they are embedded in a bulk material with high refractive index. The emitted photons experience total internal reflection at the semiconductor-air interface and only a small fraction can be extracted, typically $\sim 1\%$ for each emission line [24].

In order to address this issue, different photonic structures have been engineered; as a result, photon extraction efficiencies up to 80%, by growing the QD inside a micropillar cavity [25], up to 72%, by embedding the QD inside a photonic nanowire [26], and up to 65%, by attaching the QD to a dielectric photonic antenna [24], have been reported. Moreover, Müller et al. [27], have succeeded in near-unity photon-pair generation, $\epsilon \approx 98\%$, and an extremely high single-photon purity, $g^2(0) \approx 7.5\,E\text{-}5$, has been achieved in QDs inside photonic cavities [28]. The micropillar cavities engineered by Somaschi et al. [29], allows for electrical control of the charge noise around the QD as well as enhancing its spontaneous

emission; as a result, emitted photons show near-unity photon indistinguishability upon resonant excitation. Bulgarini et al. [30], have shown that tapered nanowires can guide the emitted photons into a Gaussian emission mode with a fidelity of 99%, which paves the way for fiber-based quantum communication. Furthermore, Elshaari et al. [31], have managed to take an important step in performing on-chip quantum optics using nanowire QDs. Also, energy-tuning of exciton and biexciton emission lines, as well as, removal of the exciton fine-structure splitting have been demonstrated [32, 33, 34].

As for the generation of entangled photon-pairs, the first measurements performed on self-assembled QDs [35, 36] reported values $F \sim 0.70$ for entanglement fidelity. The early generations of self-assembled QDs suffered from a high value of fine-structure splitting, $FSS \sim 30\mu$ev, and therefore non-classical correlations could only be observed once the FSS was tuned to zero via application of electric or magnetic fields. However, the early measurements suffered from a large level of uncorrelated coincidence counts ($> 14\%$), which were rooted in either the environment light or multi-photon emission of the source, leading to a low measured fidelity. New generations of self-assembled QDs [37], have resulted in measuring entanglement fidelity values up to $F \approx 0.98$. However, as mentioned earlier, these structure suffer from a very low pair-extraction efficiency, $\epsilon_e \sim 0.0001(1\% \times 1\%)$. Detection of entangled photon-pairs from QDs in photonic structures was first reported in the work of Dousse et al. [38], where, by coupling a pair of micropillar cavities, they managed to extract both X's and XX's from the QD. They succeeded to extract 12% of the emitted photon pairs, with a measured entanglement fidelity $F = 67\%$. Even though, Micro-pillar cavities are proper structures for extraction of single-photons from QDs, the narrow bandwidth of the structures makes photon-pair extraction a huge challenge. Use of other alternative structures, together with resonant two-photon excitation, have helped researchers to generate entangled photon-pairs at much higher rates and fidelities. Chen et al., [24], and Wang et al., [39] managed to reach a pair-extraction efficiency $\epsilon_e \approx 36\%$ with fidelity $F = 0.90$, using a broadband dielectric antenna and circular Bragg grating bull's-eye cavity, respectively.

All of the aforementioned achievements suggest the extreme potential of QDs for quantum information and quantum computing purposes. In the research performed under

supervision of Dr. Michael E. Reimer, presented in this thesis, we have shown the path for generating entangled photon-pairs with near-unity entanglement fidelity for QDs embedded in photonic nanowires. We have managed to give a complete picture of the evolution of the state of the emitted photons, as well as, shedding light on the effect of the imperfections of the measuring apparatus on calculation of the entanglement fidelity, which was generally ignored in the community. Besides, we managed to enhance the performance of the QD by applying resonant two-photon excitation. Moreover, we have improved the pair-extraction efficiency of the source by one order of magnitude. The results obtained imply that it is possible to surpass the performance of the SPDC sources in terms of both entanglement fidelity and photon-pair extraction efficiency.

In **Chapter** 2, we lay the theoretical background for the materials presented in the following chapters. We will discuss the elementary features of a QD, e.g., electronic structure, emission spectrum, fine-structure splitting etc., as well as, measures of entanglement and the two-photon state tomography scheme for calculating the density matrix of the emitted photon-pair. **Chapter** 3 is concerned with entanglement measurements and quantum state tomography of our QD under quasi-resonant excitation. We show that the QD under study exhibits an entangled state which is free from dephasing during the emission lifetime of the exciton state. We infer that once the source is excited via a two-photon resonant excitation scheme, performing the two-photon tomography with a fast detector yields near-unity entanglement fidelity. Performance of our QD under resonant two-photon excitation (TPE) is presented in **Chapter** 4. The results indicate a strong suppression of multi-photon emission and an enhancement in pair-extraction efficiency. This is an important step towards measuring near-unity entanglement fidelity with unprecedented efficiency using QDs in photonic nanowires. In **Chapter** 5, we present the all-optical universal method for erasing the fine-structure splitting of a QD. We propose that combining a diffraction grating, a pair of quarter-wave plates, and two electro-optical modulators can tune the fine-structure splitting to zero. **Chapter** 6 summarizes the results presented in this thesis and future research directions are discussed.

Chapter 2

Background

This chapter lays out the theoretical background of the work presented in the following chapters. We start with explaining the general characteristics of the source; then, the definition used for measuring entanglement is explained; and lastly, the approach for calculating the density matrix of the two-photon state is presented.

2.1 General properties of semiconductor quantum dots

A quantum dot (QD) is a nanoscale region of three dimensional confinement, which can trap electrons and/or holes in discreet energy levels upon excitation and emit quantum states of light upon relaxation to the ground state. Such a structure can be obtained by embedding a low-bandgap semiconductor, e.g. InAs, inside a high-bandgap semiconductor, e.g. InP. Since the sample used in our study is an InAsP/InP QD in a wurtzite InP photonic nanowire [40], in this section we focus on type-I QDs, which show a perfect overlap between the conduction and valence band.

2.1.1 Quantum dot confinement

Confinement modifies the electronic structure of the conduction band, CB, and the valence band, VB. The continuous energy levels found in the bulk will be lifted and form discrete energy levels due to confinement. An excited QD will have at least one electron, e, in its CB. The absence of the electron in the VB can be treated as existence of a psuedo-particle of positive charge 'hole', h. Fig.2.1 shows a schematic energy band diagram (not to scale) of a typical wurtzite InAsP/InP QD and an SEM image of a wurtzite InP tapered nanowire.

(a) (b)

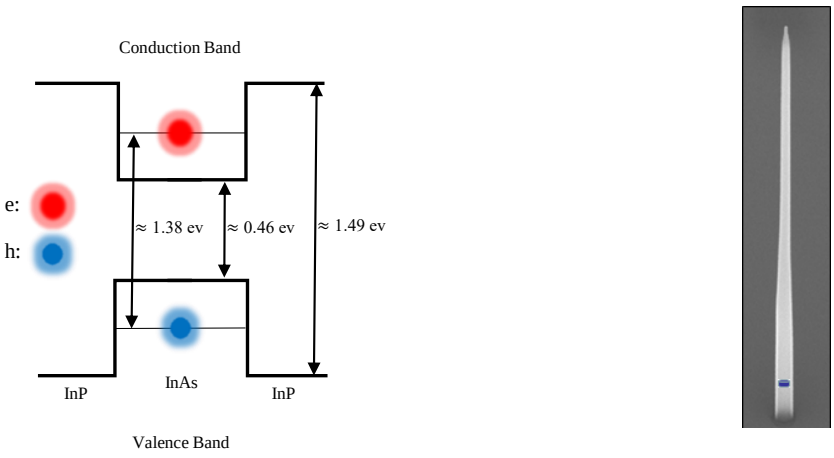

Figure 2.1: **Energy schematics and image of the source under study**. (**a**) Band energy diagram of wurtzite InAsP/InP QD. The strong confinement along the z direction allows for only one bound energy level, which is split further into a few sublevels according to the lateral confinement potential. Values for the bandgaps are taken from Ref.[41]. (**b**) SEM image of a typical nanowire which embeds the QD. The QD is depicted as a blue cylinder, $\approx$ 500 nm from the bottom. The tailoring of the nanowire tip allows for efficient photon extraction [40].

The degree of confinement in a QD is determined by the relative size of the QD, d, and the carriers' Bohr radius, a_0. As discussed in Ref.[42], a typical QD of this type has a height $h \approx 6$nm and a diameter $d \approx 30$nm. In this geometry, with $a_0 \approx 25$nm [43], the strongest confinement comes from the z-direction. Heights bellow 10nm allow for only one single z-confined energy level for electrons and holes inside the quantum dot. However, the weaker confinement in the lateral direction leads to formation of sublevels, $\{s\text{-}, p\text{-}, ...\}$ shells. In the lateral direction, the potential energy can be modeled as a simple two-dimensional harmonic oscillator, $V(r) = \frac{1}{2}m^*\omega^2 r^2$, with m^* being the effective mass of e or h [42]. This potential gives rise to states known as Fock-Darwin states, with the energy $E_{n,l} = (2n + |l| + 1)\hbar\omega$, in the absence of an external magnetic field. Here, $n(= 0, 1, 2, ...)$ represents the radial quantum number, $l(= 0, \pm 1, \pm 2, ...)$ represents the orbital angular momentum quantum number of the sublevel, and $\hbar\omega$ is the quantum of energy for e or h in the lateral degree of freedom. Now, using the convention in atomic physics, we can name the state with the lowest energy level, $E_{0,0}$, as the s-shell, the first excited degenerate states, $E_{0,1}$ and $E_{0,-1}$, as p-shell, and the second degenerate excited states, $E_{0,2}$, $E_{1,0}$ and $E_{0,2}$, as the d-shell, etc. In such a structure, the energy difference between the s-shell and p-shell is ≈ 25mev [42].

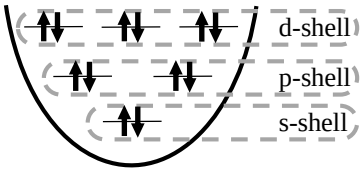

Figure 2.2: **Shell model for the CB**. Assuming a two-dimensional simple harmonic oscillator potential in the lateral direction results in Fock-Darwin states, which, can be grouped into different shells. A similar configuration can be represented for the VB as well.

The energy diagram of the electrons in the QD's CB is depicted in Fig.2.2. A similar diagram can be drawn for the VB addressing the holes.

2.1.2 QD's emission

In a simple scenario, excitation of the QD can lead to the generation of an electron-hole, e-h, pair. This pair is confined within the boundaries of the QD and has a particular lifetime. Relaxation of the electron back to the VB, e-h recombination, and photon generation should preserve the total angular momentum; therefore, a detailed study of the angular momentum of the electrons and holes in the QD is necessary.

Angular Momentum, Effective Mass & Energy Splitting

For each particle, the total angular momentum, $\mathbf{J}$, consists of three parts: the spin angular momentum, $\mathbf{S}$; the intrinsic band angular momentum, $\mathbf{L_{band}}$; and the orbital angular momentum from the shells of the Fock-Darwin states, $\mathbf{L_{shell}}$. Therefore, the total angular momentum operator can be written as:

$$\mathbf{J} = \mathbf{L_{band}} + \mathbf{L_{shell}} + \mathbf{S}, \tag{2.1}$$

with the quantum numbers j, l_{band}. l_{shell} and s, denoting each operator, respectively. Also, the projection of the total angular momentum along z direction, $\mathbf{J}_z$, can be represented by the quantum number $j_z \in \{-j, -j+1, \dots, j-1, j\}$.

Both electrons and holes are spin-$\frac{1}{2}$ particles, i.e., $s = \frac{1}{2}$. The lowest state of the CB exhibits an s-like orbital, thus for the excited electrons $\mathbf{L_{band}} = 0$. Now, by limiting ourselves to the s-shell of the QD, *i.e.*, $\mathbf{L_{shell}} = 0$, the total angular momentum quantum number of the electrons will be $\mathbf{J} = \mathbf{S}$; meaning $j = s = \frac{1}{2}$, and $j_z = \pm\frac{1}{2}$. On the other hand, the holes in the highest state of the VB occupy a p-like orbital, i.e., $l_{band} = 1$. Therefore, for the case of the QD's s-shell, the total angular momentum of the holes will be $\mathbf{J} = \mathbf{L_{band}} + \mathbf{S}$, with $\{j\} = \{|l_{band} + s|, |l_{band} - s|\} = \{\frac{3}{2}, \frac{1}{2}\}$, and $\{j_z\} = \{\{-\frac{3}{2}, -\frac{1}{2}, \frac{1}{2}, \frac{3}{2}\}, \{-\frac{1}{2}, \frac{1}{2}\}\}$ for the two possible j's [44].

The band structure for electrons and holes in the QD is depicted in Fig.2.3. The CB only shows one curve corresponding to an electron with $j = \frac{1}{2}$; however, the holes in the VB are split into three regimes each with a particular energy splitting.

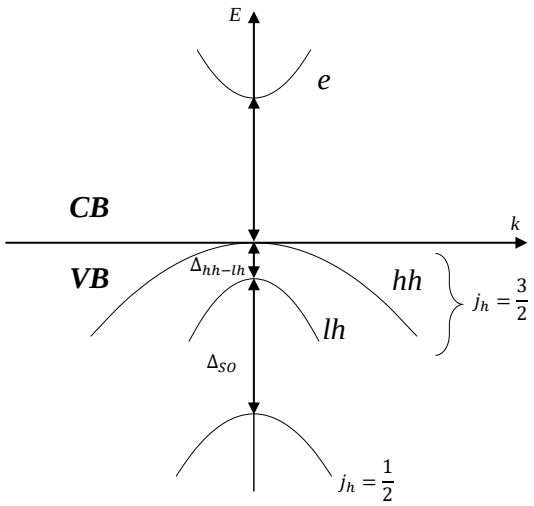

Figure 2.3: **Engery band structure for the CB and VB**. There is only one curve attributed to the electron in the CB with $j_z = \frac{1}{2}$. In the valence band, on the other hand, the holes with $j = \frac{1}{2}$ are separated from holes with $j = \frac{3}{2}$ by Δ_{SO} according to the spin-orbit coupling. Furthermore, the $j = \frac{3}{2}$ holes are split into heavy-holes, hh's, and light-holes, lh's, which are separated by Δ_{hh-lh}.

The spin-orbit coupling and strain play an important role in the energy level structure for holes possessing different angular momentum. In the case of a nearly isotropic interaction in the crystal, the spin-orbit coupling can be represented approximately by [44]:

$$H_{so} \approx \lambda_{so}\mathbf{L}.\mathbf{S} = \frac{1}{2}\lambda_{so}(\mathbf{J}^2 - \mathbf{L}^2 - \mathbf{S}^2) \tag{2.2}$$

where, λ_{so} is a constant determined by the atomistic details of the QD. Based on eq.2.2, it is easy to verify that the spin-orbit interaction leads to an energy difference of $\Delta_{so} = 3\hbar^2\lambda_{so}/2$

between holes with $j = 3/2$ and $j = 1/2$. In InAs/InP QDs, $\Delta_{so} > 100\,\text{mev}$ and thus can be neglected once dealing with the QD's lowest energy transitions [45, 46].

Furthermore, holes with $j = \frac{3}{2}$ can be divided into two categories; the heavy-holes, hh, with $j_z = \pm\frac{3}{2}$, and the light-holes, lh, with $j_z = \pm\frac{1}{2}$. In a crystal structure, the effective mass of a charge carrier in band b, m_b^*, along a particular direction $\alpha\beta$, is calculated from the curvature of its E-k energy band diagram [44]:

$$[(m_b^*)^{-1}]_{\alpha\beta} = \frac{1}{\hbar^2}\frac{\partial^2 E_b(\mathbf{k})}{\partial k_\alpha \partial k_\beta}. \tag{2.3}$$

The difference in the curvature of the energy band diagrams for hh's and lh's, Fig.2.3, results in a difference in their effective masses, with $m_{hh}^* \approx 8m_{lh}^*$ [42], and hence their names. Even though, in principle, the inter-subband interactions can lead to mixing of the lh and hh states, strain causes weakening of the strength of such interactions [42]; also, some experimental results suggest that the inter-subband interactions are negligible [47]. Lastly, due to strain and confinement, there's a energy difference between lh's and hh's, Δ_{hh-lh}, in the order of tens of meV [45, 46]; which, combined with the spin-orbit splitting of holes with $j = \frac{1}{2}$, means that the optical transitions for the lowest energy level can be solely attributed to electrons with $j_z = \pm\frac{1}{2}$, and heavy-holes with $j_z = \pm\frac{3}{2}$. Since we will only be dealing with the heavy-holes, from here onward, for the sake of simplicity, we will refer to the heavy-holes as simply holes.

Emission Spectrum

The CB electron and the VB hole, can become bound together via Coulomb interaction and form an e-h pair named an exciton, $|X\rangle$. Then, through the e-h recombination process, a circularly polarized photon will be emitted. For the case of InAs/InP QDs, with $m_h^* \approx 10m_e^*$ [42], one can think of $|X\rangle$ as the excited state of a hydrogen-like atom with a particular lifetime [44]. Different configurations of the electron and the hole in the e-h pair, will result in four possible exciton states with $j_z \in \{+2, +1, -1, -2\}$. Now, by representing the set of hole states as $\{|h\rangle\} = \{|\Uparrow\rangle, |\Downarrow\rangle\}$ for $j_z \in \{+\frac{3}{2}, -\frac{3}{2}\}$, and the set of electron states

as $\{|e\rangle\} = \{|\uparrow\rangle, |\downarrow\rangle\}$ for $j_z \in \{+\frac{1}{2}, -\frac{1}{2}\}$, respectively, the possible exciton states can be written as:

$$|+2\rangle \equiv |\uparrow\Uparrow\rangle = |\uparrow\rangle_e + |\Uparrow\rangle_h \,, \tag{2.4}$$

$$|+1\rangle \equiv |\downarrow\Uparrow\rangle = |\downarrow\rangle_e + |\Uparrow\rangle_h \,, \tag{2.5}$$

$$|-1\rangle \equiv |\uparrow\Downarrow\rangle = |\uparrow\rangle_e + |\Downarrow\rangle_h \,, \tag{2.6}$$

$$|-2\rangle \equiv |\downarrow\Downarrow\rangle = |\downarrow\rangle_e + |\Downarrow\rangle_h \,. \tag{2.7}$$

Since a circularly polarized photon carries a total angular momentum of $\pm\hbar$, and has a total spin of zero, the following selection rules should be obeyed so that the *e*-*h* recombination results in emission of a photon:

$$\Delta j_z = \pm 1, \tag{2.8}$$

$$\Delta s = 0. \tag{2.9}$$

As it is clear, out of the four possible exciton states only two, $|X\rangle = |\downarrow\Uparrow\rangle$ and $|X\rangle = |\uparrow\Downarrow\rangle$, can lead to emission of a photon, and thus are called *bright* excitons; the recombination of the other two states, which are called *dark* excitons, are optically forbidden.

In addition to the different spin configurations within an *e*-*h* pair, different charge configurations will result in different excitonic states. The *s*-shell can host up to two electrons and two holes. Formation of an $|X\rangle$ in the presence of extra charge carriers can lead to more sophisticated Coulomb interactions which can shift the energy of the emitted photon. Fig.2.4a, shows different charge configurations for the *s*-shell.

The simplest case is an *e*-*h* pair without any adjacent charges, $|X\rangle$. An exciton in the presence of an extra charge is called a trion, $|X^*\rangle$; which, can be either be $|X^+\rangle$ or $|X^-\rangle$, depending on whether the extra charge is a hole or an electron, respectively. Lastly, the *s*-shell can have two *e*-*h* pairs, or in other words a bi-exciton, $|XX\rangle$; we shall only consider a neutral biexciton, i.e., there are no other charge carriers in the higher shells. The energy

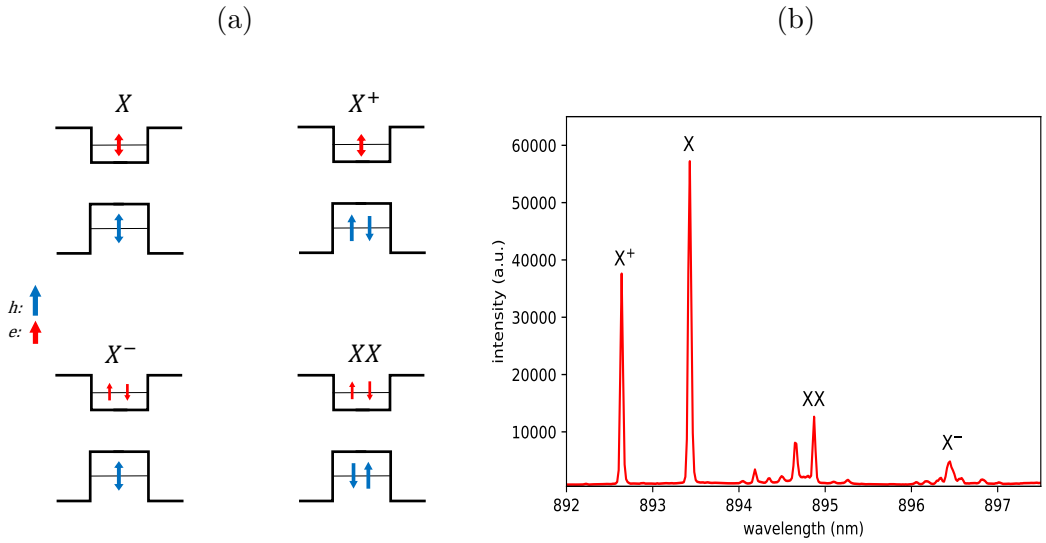

Figure 2.4: **Charge configurations of the *s*-shell and the emission spectrum of the QD.** (**a**) The four possible charge configurations in the *s*-shell. The double sided arrows indicate possibility of a spin-up and spin-down configuration. (**b**) Spectrum of an InAsP/InP QD in a wurtzite InP nanowire under quasi-resonant excitation [48]. The lines other than the four configurations may be associated with presence of charges in higher shells.

of these four possible configurations can be written as:

$$E_{|X\rangle} = E_e + E_h - V_{eh} \tag{2.10}$$

$$E_{|X^+\rangle} = E_e + 2E_h + V_{hh} - V_{eh} \tag{2.11}$$

$$E_{|X^-\rangle} = 2E_e + E_h + V_{ee} - V_{eh} \tag{2.12}$$

$$E_{|XX\rangle} = 2E_e + 2E_h + V_{ee} + V_{hh} - 2V_{eh}, \tag{2.13}$$

with E_e and E_h being the confinement energies of electrons and holes, respectively, and the Coulomb interaction energies represented by V_{eh}, V_{ee} and V_{hh} with the general form:

$$V_{ij} = \frac{e^2}{4\pi\epsilon} \langle \psi_i \psi_j | \frac{1}{|\mathbf{r}_i - \mathbf{r}_j|} | \psi_i \psi_j \rangle \,. \tag{2.14}$$

In order to investigate the emission spectrum of a QD we have to consider the change in the energy of these four states after recombination of an e-h pair. The transitions will be:

$$|X\rangle \rightarrow |G\rangle\,, \tag{2.15}$$

$$\left|X^{+}\right\rangle \rightarrow |h\rangle\,, \tag{2.16}$$

$$\left|X^{-}\right\rangle \rightarrow |e\rangle\,, \tag{2.17}$$

$$|XX\rangle \rightarrow |X\rangle\,, \tag{2.18}$$

with $|G\rangle$ being the ground state, $|e\rangle$ the s-shell with only one electron, and $|h\rangle$ the s-shell with only one hole. We shall call these transitions simply X, X^{+}, X^{-} and XX transition, respectively. Setting $E_G = 0$, it is straightforward to see that the energies of these four transitions are:

$$\Delta E_X \equiv \Delta E_{|X\rangle\rightarrow|G\rangle} = E_X, \tag{2.19}$$

$$\Delta E_{X^+} \equiv \Delta E_{|X^+\rangle\rightarrow|h\rangle} = E_X + V_{hh} - V_{eh}, \tag{2.20}$$

$$\Delta E_{X^-} \equiv \Delta E_{|X^-\rangle\rightarrow|e\rangle} = E_X + V_{ee} - V_{eh}, \tag{2.21}$$

$$\Delta E_{XX} \equiv \Delta E_{|XX\rangle\rightarrow|X\rangle} = E_X + V_{hh} + V_{ee} - 2V_{eh}. \tag{2.22}$$

Now, by considering the fact that the hole, due to its heavier mass, is more bound compared to the electron, according to eq.2.14, we will have the condition $V_{hh} > V_{eh} > V_{ee}$. Therefore, compared to the X transition, the X^{+} and X^{-} transitions will be blue-shifted and red-shifted respectively. The difference in the energies of the X and XX transitions, i.e., ΔE_X - ΔE_{XX}, is called the biexciton binding energy. Depending on the confinement conditions, we might have $V_{hh} + V_{ee} - 2V_{eh}$ greater or smaller than zero, i.e., a positive or negative biexciton binding energy [44]. Therefore, in the QD's spectrum the XX transition might have a higher or lower wavelength compared to that of the X transition. A typical spectrum of a QD is presented in Fig.2.4b.

The XX-X Cascade and Polarization Entanglement

Starting with a filled s-shell, the QD will emit a photon according to the energy and lifetime of $|XX\rangle$ and relax to $|X\rangle$. Now, depending on the charge environment and the possibility of trapping of either an electron or a hole, the QD can take different paths to reach the ground state:

$$|XX\rangle \rightarrow |X\rangle \rightarrow |G\rangle\,, \tag{2.23}$$

$$|XX\rangle \rightarrow |X\rangle \xrightarrow{+h} \left|X^{+}\right\rangle \rightarrow |h\rangle\,, \tag{2.24}$$

$$|XX\rangle \rightarrow |X\rangle \xrightarrow{+e} \left|X^{-}\right\rangle \rightarrow |e\rangle\,. \tag{2.25}$$

Among these different possible transitions, the direct one, $|XX\rangle \rightarrow |X\rangle \rightarrow |G\rangle$, has the highest probability; since, for all the other cases, a surrounding charge has to be trapped by the QD within the lifetime of $|X\rangle$. We shall call this transition sequence the biexciton-exciton, XX-X, cascade. Also, the cascade itself, by considering the spin configuration of $|XX\rangle$ and $|X\rangle$, can be represented by a superposition of two separate path-ways. This cascade is shown schematically in Fig.5.1.

The biexciton state is composed of two e-h pairs with opposite angular momentum, $j_z = \pm 1$, represented by $|+1\rangle$ and $|-1\rangle$ according to Eq.2.5 and Eq.2.6. Thus, the XX transition can either generate a left circularly polarized photon, $|L\rangle$, or a right circularly polarized photon $|R\rangle$, for the cases of $|+1\rangle$ and $|-1\rangle$ respectively. This leads to two different scenarios for the emission of the X transition as well; by emission of an $|L\rangle$ photon from the XX transition, we will end up with an e-h pair with $j_z = -1$, and emission of a subsequent $|R\rangle$ photon. And alternatively, emission of an $|R\rangle$ photon from the XX transition will lead to emission of an $|L\rangle$ photon from the X transition. In an ideal situation, there will be no which-path information regarding these two possible scenarios; and this lack of information, as first proposed by Benson et al. [23], will result in generation of a pair of polarization entangled photons with the wave function:

$$|\Psi\rangle = \frac{1}{2}(|RL\rangle + |LR\rangle). \tag{2.26}$$

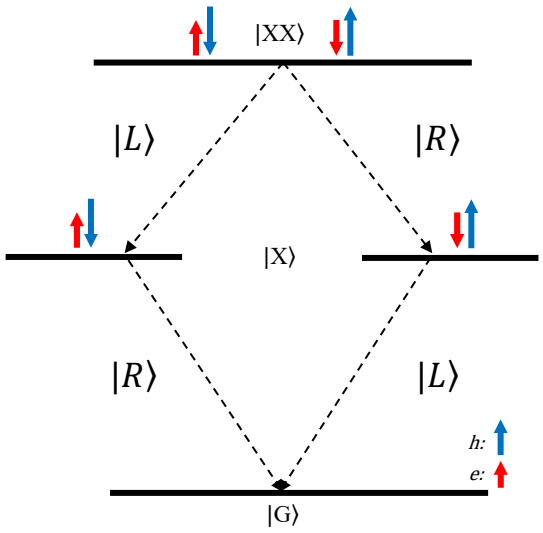

Figure 2.5: **The *XX*-*X* cascade.** Depending on which of the two e-h pairs recombine first, the cascade will follow two different path-ways. The final state will be a superposition of these two paths, i.e., $|\Psi\rangle = \frac{1}{\sqrt{2}}(|RL\rangle + |LR\rangle)$.

Trapping of extra charges after the XX transition, Eq.2.24 and Eq.2.25, will reduce the efficiency in generation of the entangled photon pairs; since, the polarization of the generated photon from X^+ and X^- transitions will no longer be correlated with the polarization of the photon generated from the XX transition, and the emission energies will also shift. Furthermore, it is possible that the QD traps another e-h pair and fill the s-shell again after it has relaxed to $|X\rangle$. This process, called re-excitation of the biexciton state, can lead to emission of two subsequent photons attributed to the XX transition. This scenario results in degradation of single-photon purity of the source and also the measured entanglement fidelity of the XX-X cascade [48].

Exciton's Fine-structure Splitting

In addition to the Coulomb interaction, the exchange interaction between the electron and the hole of the exciton state can give rise to finer changes in energy, i.e., the fine-structure splitting (FSS). The FSS is orders of magnitude smaller than the lh-hh and the spin-orbit splitting, and falls in a range from a few μeV up to a few hundred μeV [49, 50, 51]. Generally speaking, any sort of asymmetry in the QD, e.g., caused by strain, crystal structure, macroscopic geometry of the QD, etc., can result in lifting of the degeneracy of the X state, and, thus, observation of the FSS. Once dealing with generation of entangled photons with a QD, the FSS can be a significant challenge; since, in the case that the FSS is larger than line-widths of the emitted photons ($\sim 1\mu$ev), a which-path information between the two transition path-ways in the XX-X cascade will emerge, and the measured entanglement fidelity of the source degrades [48, 51, 52].

The e-h exchange interaction can be written as [51, 53]:

$$E_{ex} \propto \int\int d^3r_e d^3r_h \Psi_X^*(\mathbf{r}_e, \mathbf{r}_h) \frac{1}{|\mathbf{r}_e - \mathbf{r}_h|} \Psi_X(\mathbf{r}_h, \mathbf{r}_e), \tag{2.27}$$

where, $\mathbf{r}_{e/h}$ represent the position vector of electron/hole, and $\Psi_X(\mathbf{r}_h, \mathbf{r}_e)$ represents the exciton wave function. The integral can be split into two parts; (*i.*) the short-range interaction; which, deals with the electron and hole both existing in the same Wigner-Seitz unit cell, and (*ii.*) the long-range interaction; which, deals with finding the electron and

hole in different Wigner-Seitz unit cells. The short-range interaction is mainly affected by the symmetry of the QD at the atomistic level, i.e., crystal symmetry, whereas the long-range interaction deals with symmetry at the macroscopic geometry of the QD, i.e., circularity of QD's base [51].

The short-range interaction of Eq.2.27 can also be written in terms of coupling of the spins of the electron and hole forming the exciton [53, 54]:

$$H_{ex} = -\sum_{i=x,y,z} (a_i J_{h,i} S_{e,i} + b_i J_{h,i}^3 S_{e,i}) \tag{2.28}$$

where a_i and b_i, $\{i = x, y, z\}$, are the coupling constants, and $J_{h,i}$ and $S_{e,i}$ are the angular momentum and spin operators in three dimensions for the hole and electron, respectively. Here, the z direction is considered to be along the growth direction of the QD. The long-range interaction may as well be written in a similar form with the corresponding coupling constants. Now, by limiting ourselves to the heavy-holes, and choosing $|+1\rangle, |-1\rangle, |+2\rangle \,\&\, |-2\rangle$ (Eq.2.4 - Eq.2.7) as the basis, the short-range interaction can be represented by the matrix [53]:

$$H_{ex}^{short-range} = \frac{1}{2} \begin{pmatrix} +\delta_0 & +\delta_1 & 0 & 0 \\ +\delta_1 & +\delta_0 & 0 & 0 \\ 0 & 0 & -\delta_0 & +\delta_2 \\ 0 & 0 & +\delta_2 & -\delta_0 \end{pmatrix}, \tag{2.29}$$

where, $\delta_0 = 1.5(a_z + 2.25b_z)$, $\delta_1 = 0.75(b_x - b_y)$, and $\delta_2 = 0.75(b_x + b_y)$. We can refer to the top left 2×2 block as the bright-block, and the bottom right 2×2 block as the dark-block. The short-range interaction gives rise to splitting of energy between the bright and dark states, with $\Delta E = \delta_0$; as well as, mixing of the states within the bright- and dark-blocks, i.e., the off-diagonal terms δ_1 and δ_2.

The long-range part of the exchange Hamiltonian will only affect the bright states [53]; it will enhance the energy splitting between the bright and dark states by lifting the energy of the bright states; and also, strengthen the mixing of the states within the bright-block by

increasing the off-diagonal terms. Eventually, the overall exchange Hamiltonian of Eq.2.27 can be represented by:

$$H_{ex} = \frac{1}{2}\begin{pmatrix} +\delta_0' & +\delta_1' & 0 & 0 \\ +\delta_1' & +\delta_0' & 0 & 0 \\ 0 & 0 & -\delta_0 & +\delta_2 \\ 0 & 0 & +\delta_2 & -\delta_0 \end{pmatrix}, \tag{2.30}$$

with $\delta_0' = \delta_0 + \gamma_0$, where γ_0 is the contribution of the long-range interaction to the energy of the bright states; and $\delta_1' = \delta_1 + \gamma_1$, with $\gamma_1 = \gamma_x - \gamma_y$ being the contribution of the long-range interaction to FSS. γ_i $\{i = x, y\}$ are the coupling constants of the long-range interaction. The long-range e-h exchange interaction is shown to be the dominant factor in the exchange Hamiltonian [55], i.e., $\gamma_1 \gg \delta_1$, which means in terms of symmetry, the macroscopic geometry of the QD plays the main role.

In the case of a QD with high degree of symmetry, e.g. D_{2d} or C_{3V} symmetry groups which show an in-plane rotation invariance [51, 53], the x-y plane coupling constants follow the conditions:

$$b_x = b_y, \tag{2.31}$$

$$\gamma_x = \gamma_y. \tag{2.32}$$

In other words, $\delta_1 = \gamma_1 = 0$. In this case, the circularly polarized $|+1\rangle$ and $|-1\rangle$ states will not be coupled and remain as the degenerate eigenstates of the bright-block. In the case of a low degree of symmetry, e.g., C_{2V}, C_2, C_1 etc. [51, 53], $\delta_1' \neq 0$ and the bright states will be mixed into:

$$|+\rangle \equiv \frac{1}{\sqrt{2}}(|+1\rangle + |-1\rangle) \tag{2.33}$$

$$|-\rangle \equiv \frac{1}{\sqrt{2}}(|+1\rangle - |-1\rangle), \tag{2.34}$$

which will form the linearly polarized non-degenerate eigenstates of the bright-block, with energies equal to $E_+ = \frac{1}{2}\delta_0' + \frac{1}{2}\delta_1'$ and $E_- = \frac{1}{2}\delta_0' - \frac{1}{2}\delta_1'$, and an FSS $= E_+ - E_- = \delta_1'$. We

shall represent the fine-structure splitting simply as δ. In the case of an elliptical QD, the intrinsic polarizations $|+\rangle$ and $|-\rangle$ will lie along the major and minor axis, respectively [44]. We shall refer to these two polarization states simply as horizontal, $|H\rangle$, and vertical, $|V\rangle$.

FSS and XX-X cascade

The FSS and mixing of the bright $|X\rangle$ states will also affect the recombination of the e-h pairs in the XX transition. Mixing of the $|+1\rangle$ and $|-1\rangle$ can be thought of as precession of $|X\rangle$ between these two states at a rate proportional to the FSS. This precession is analogous to precession of S_x of an electron around a magnetic field $\mathbf{B} = B\hat{z}$. This means that once the XX transition results in an $|L\rangle$ photon the X transition will no longer emit solely an $|R\rangle$ photon. Instead, before its emission, $|X\rangle$ can precess to the other path-way and have a finite probability of emitting again another $|L\rangle$. A similar situation can take place starting with an $|R\rangle$ photon from the XX transition. This means that the XX-X cascade will no longer be a simple superposition of the two path-ways, $|LR\rangle + |RL\rangle$; instead, two other transition path-ways are possible in the XX-X cascade, i.e., $|R\rangle \rightarrow |R\rangle$ and $|L\rangle \rightarrow |L\rangle$, with oscillations between these two possible cascades, i.e., between $(|LR\rangle + |RL\rangle)$ and $(|LL\rangle + |RR\rangle)$. The oscillations can be observed in the $|R\rangle/|L\rangle$ basis; however, projections along the intrinsic polarizations of the QD will not show such oscillations, since $|H\rangle$ and $|V\rangle$ are the eigenstates of the bright-block in the exchange-interaction Hamiltonian matrix, Eq.2.30. But, such projections will yield photons with different energies separated by the FSS. Taking these facts into consideration, the two-photon state from the XX-X cascade represented by Eq.2.26 will be modified to:

$$\begin{aligned} |\tilde{\Psi}\rangle &= \frac{1}{\sqrt{2}}(|HH\rangle + e^{i\frac{\delta}{2\hbar}t}\,|VV\rangle) \\ &= \cos(\frac{\delta}{2\hbar}t)\,|\Psi\rangle + i\sin(\frac{\delta}{2\hbar}t)\,|\Phi\rangle\,, \end{aligned} \tag{2.35}$$

where $|\Psi\rangle = \frac{1}{\sqrt{2}}(|RL\rangle + |LR\rangle)$, $|\Phi\rangle = \frac{1}{\sqrt{2}}(|RR\rangle + |LL\rangle)$, and $\delta = FSS$. The schematics of the XX-X cascade in the presence of a non-zero FSS is represented in Fig.2.6. One important

point to consider is the fact that presence of FSS does not destroy the entanglement. The precession between the two entangled states $|\Psi\rangle$ and $|\Phi\rangle$, does not affect the entanglement; the two-photon state stays as a superposition of the two entangled states with oscillating probability amplitudes.

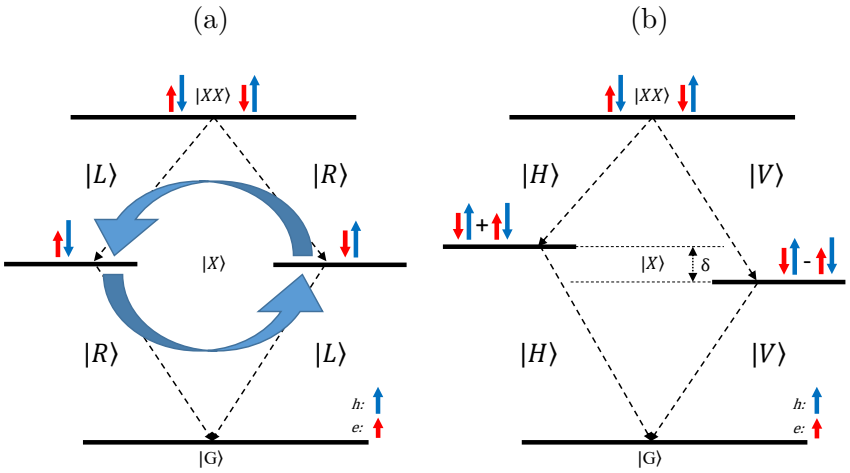

Figure 2.6: ***XX-X* cascade in presence of FSS.** (**a**) $|R\rangle$ and $|L\rangle$ basis will be mixed and a precession between the two path-ways will be observed. (**b**) In the $|H\rangle - |V\rangle$ basis, the transitions will be split by FSS=δ.

2.2 Second-order coherence measurement

In order to investigate whether an emitter is generating quantum states of light, one has to measure the second-order coherence function of the emitted light, defined as [56]:

$$g^{(2)}(\tau) = \frac{\langle I(t)I(t+\tau)\rangle}{\langle I(t)\rangle\langle I(t+\tau)\rangle} \tag{2.36}$$

where, $I(t)$ indicates the intensity of light at time t. The nominator corresponds to the correlation between the intensity of light at some time t and some later time $t+\tau$, and the

denominator serves as a normalization factor. Hanbury Brown and Twiss [57], motivated by improving stellar interferometry, pioneered a simple method for calculating $g^{(2)}(\tau)$. By correlating the intensities registered on the two separate photodiodes, Hanbury Brown and Twiss managed to improve the Michelson interferometer in terms of stability and resolution. The experimental setup is made of a beam-splitter, which divides the incoming light beam into two separate paths, and two detectors to timetag the intensity fluctuations in the field. A schematic view of the setup is given in Fig. 2.7.

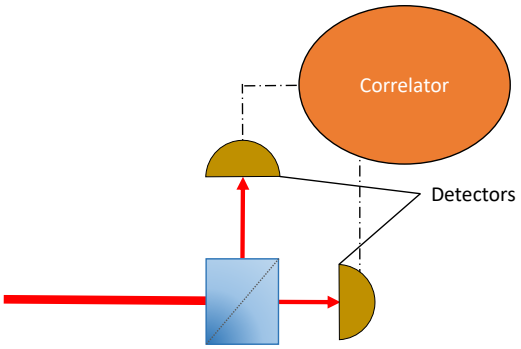

Figure 2.7: **Schematics of Hanbury Brown-Twiss setup.** Light is directed towards a beam-splitter, and the timetagged intensities measured by the two detectors are correlated in order to calculate the $g^{(2)}(\tau)$ function.

For a quantum state of light, written in terms of photon number states $|n\rangle\,(n \in \{0, 1, ...\})$, intensity of light in a time period is proportional to the average number of photons in that particular time bin. Therefore Eq. 2.36 can be rewritten as:

$$g^{(2)}(\tau) = \frac{\langle \hat{n}_1(t)\hat{n}_2(t+\tau)\rangle}{\langle \hat{n}_1(t)\rangle\langle \hat{n}_2(t+\tau)\rangle}, \tag{2.37}$$

where $\hat{n}_i (i = 1, 2)$ is the photon number operator for each path.

In practice, the value we are after is the value of the second-order coherence function at zero time delay, i.e., $\tau = 0$. Considering a single photon, once the photon hits the beam-splitter, the particle nature of the photon will dictate that the detection will be

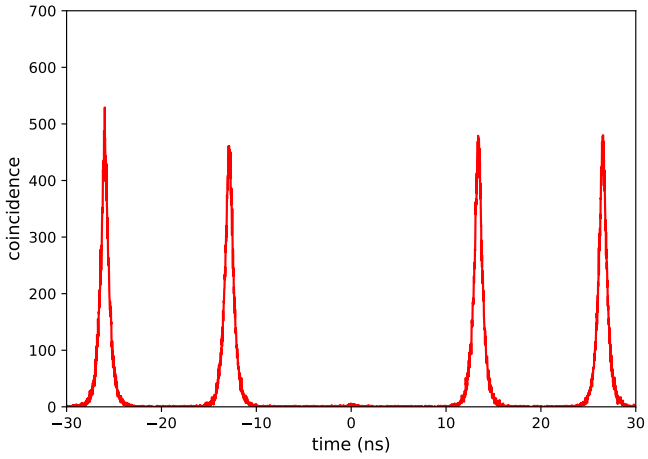

Figure 2.8: Results from HBT measuring setup. Upon excitation of the quantum light emitter by a pulsed laser source, one expects to detect single-photons at a certain frequency f, here $f \approx 76\,\mathrm{MHz}$. The nominator in Eq. 2.37 can be calculated by summing the coincidence counts in the proximity of $t = 0$, and the denominator in Eq. 2.37 is obtained by taking the averaged sum of the coincidence counts in the side peaks.

made by either detector 1, or detector 2, and never by both at the same time. In other words, once a single photon is sent to the Hanbury Brown-Twiss (HBT) setup, there will be no coincidence between the two detectors at zero time delay, i.e., $g^{(2)}(0) = 0$. Thus, any deviation of $g^{(2)}(0)$ from zero reveals the probability of multi-photon emission of the source. A typical histogram acquired from the HBT setup, with pulsed excitation of the source, is shown in Fig 2.8; $g^{(2)}(0)$ can be calculated by dividing the sum of the coincidence counts in the central region, by the averaged sum of coincidence counts in the adjacent side peaks. However, in a realistic scenario, one has to take the effect of detectors' dark-counts into consideration, as they will add false coincidence counts in each time bin.

2.3 Measuring Entanglement

Proper definition, measurement and analysis has to be presented in order to investigate the degree of entanglement in quantum light sources. Here, we will follow the works by Bennett et al. [58], S. Hill & W. K. Wootters [59], W. K. Wootters [60], and F. Verstraet & H. Verschelde [61], to introduce measures for entanglement of a pure state. Afterwards, following the work of James et al. [62], we present a method for calculating the density matrix of a pure state, which enables us to extract the strength of its entanglement. We limit our discussion to a two-qubit state, consisting of two particles each having only two degrees of freedom, e.g., two spin-$\frac{1}{2}$ electrons.

2.3.1 Entanglement Definition, Concurrence & Fidelity

A bipartite system of two subsystems Alice (A) & Bob (B) are called entangled, if and only if, the joint Hilbert space cannot be decomposed into a tensor product of two separate Hilbert spaces [58]. In other words, the overall state $|\Psi\rangle$ cannot be written as a product of two pure states, $|\psi\rangle_A \otimes |\psi\rangle_B$. A simple example of such a state is $|\Phi\rangle = \frac{1}{\sqrt{2}}(|\uparrow\downarrow\rangle - |\downarrow\uparrow\rangle)$, for a system of two electrons with two possible spin orientations along the z axis, $|\uparrow\rangle$ and $|\downarrow\rangle$. It is worth noting that an entangled state cannot be generated through any series of separate local operations on unentangled particles [58]. This definition can be easily extended to multi-particle systems.

The level of entanglement existent in a bipartite system is measured by calculating the entropy of the reduced density matrix [58, 60]:

$$E(\hat{\rho}) = S(\hat{\rho}_A) = S(\hat{\rho}_B) \tag{2.38}$$

where $E(\hat{\rho})$ is the level of entanglement in the pure state $|\Psi\rangle$ with density matrix $\hat{\rho} = |\Psi\rangle\langle\Psi|$, $\hat{\rho}_A = Tr_B |\Psi\rangle\langle\Psi|$ is Alice's reduced density matrix acquired by tracing the density matrix of the whole state over Bob's degrees of freedom, and $S(\hat{\rho}_A) = -Tr(\hat{\rho}_A \, log_2 \, \hat{\rho}_A)$ is the entropy of Alice's reduced density matrix. Similar definitions hold for $\hat{\rho}_B$ and $S(\hat{\rho}_B)$. The quantity $E(\hat{\rho})$, which from now on we simply call entanglement, can range from zero,

for a product state $|\psi\rangle_A \otimes |\psi\rangle_B$, up to $log_2 N$, for a system of two N-state particles [58]. In the case of the entangled state $|\Phi\rangle$, $E(\hat{\rho})$ will be equal to 1. Furthermore, entanglement of independent systems is additive, and also for each system the value of entanglement is invariant under local unitary transformations, $U = U_A \otimes U_B$ [58]. The motivation behind such a definition of entanglement comes from entanglement purification protocols. Consider n pairs of qubits, each in some arbitary state $|\Psi\rangle$. Alice and Bob, which are spatially separated, each possess one qubit of each pair. Now, if each pair of qubits has an entanglement value $E < 1$, it can be shown that, by means of purely local operations and classical communications between Alice and Bob, out of these n pairs, m pairs of qubits, each in the state $|\Phi\rangle$, can be extracted with $\frac{m}{n} \to E$ and fidelity of conversion approaching unity for large n [58, 59]. In other words, n pairs of non-maximally entangled qubits, with entanglement $E < 1$, are equivalent to m=nE pairs of maximally entangled qubit pairs, when n $\to \infty$.

The space of bipartite pure states can be spanned over four specific orthogonal entangled states, known as the Bell states:

$$|e_1\rangle = \frac{1}{\sqrt{2}}(|\uparrow\downarrow\rangle + |\downarrow\uparrow\rangle) \tag{2.39}$$

$$|e_2\rangle = \frac{1}{\sqrt{2}}(|\uparrow\downarrow\rangle - |\downarrow\uparrow\rangle) \tag{2.40}$$

$$|e_3\rangle = \frac{1}{\sqrt{2}}(|\uparrow\uparrow\rangle + |\downarrow\downarrow\rangle) \tag{2.41}$$

$$|e_4\rangle = \frac{1}{\sqrt{2}}(|\uparrow\uparrow\rangle - |\downarrow\downarrow\rangle). \tag{2.42}$$

Now, any pure state of a two-qubit system can be written as $|\Psi\rangle = \sum_i \alpha_i |e_i\rangle$ with $\alpha_i \in \mathbb{C}$. By defining the parameter $C(\hat{\rho}) = |\sum_i \alpha_i^2|$, as the concurrence of the state $|\Psi\rangle$, one can rewrite Eq.2.38 as [58]:

$$E(\hat{\rho}) = H(\frac{1 + \sqrt{1 - C(\hat{\rho})^2}}{2}) \tag{2.43}$$

where $H(x) = -xlog_2 x - (1-x)log_2(1-x)$, is the binary entropy function. Concurrence of a state lies in the range [0,1], with 0 being the concurrence of a pure product state and 1 being the concurrence of a pure entangled state; also, $E(\hat{\rho})$ is a monotonically increasing

function of $C(\hat{\rho})$ with the same range, [0,1]. Hence, one may as well use the quantity $C(\hat{\rho})$ as a measure of the entanglement of a state.

Alternatively, concurrence of a state can be calculated using the density matrix approach, which might be more suitable for analyzing the experimental results and addressing situations involving mixed states. For this matter, we first start with the spin-flipped wave function of the bipartite system, $|\tilde{\Psi}\rangle = \sigma_y |\Psi\rangle$, with the density matrix $\hat{\tilde{\rho}} = (\sigma_y \otimes \sigma_y)\hat{\rho}^*(\sigma_y \otimes \sigma_y)$, where $\hat{\rho}^* = (|\Psi\rangle \langle\Psi|)^*$, and σ_y being the y Pauli matrix. The concurrence can then be written as [60]:

$$C(\hat{\rho}) = \left|\left\langle \Psi \middle| \tilde{\Psi} \right\rangle\right|. \tag{2.44}$$

In other words, the concurrence is the absolute value of the overlap between $|\Psi\rangle$ and its spin-flipped counterpart. This relation can be shown to be equivalent to [60]:

$$C(\hat{\rho}) = max\{0, \lambda_1 - \lambda_2 - \lambda_3 - \lambda_4\}, \tag{2.45}$$

where λ_is are the eigenvalues of the matrix $R \equiv \sqrt{\sqrt{\hat{\rho}}\hat{\tilde{\rho}}\sqrt{\hat{\rho}}}$, in a descending order [60]. In the case of the maximally entangled state $|\Phi\rangle$ mentioned earlier, flipping the spins of the two particles yields $|\tilde{\Phi}\rangle = -|\Phi\rangle$, which indicates $C(\hat{\rho}) = 1$. The situation is the same for all the Bell states.

Another important parameter for defining the degree of entanglement of a quantum state, with density matrix $\hat{\rho}$, known as fidelity of entanglement, F, and is defined as the maximum overlap of $\hat{\rho}$ with a maximally entangled state $|\Theta\rangle$ [61]:

$$F(\hat{\rho}) = max \langle\Theta| \hat{\rho} |\Theta\rangle . \tag{2.46}$$

We may as well think of the states $|\Theta\rangle$ as any possible unitary transformation of any of the Bell states defined in Eq.2.39-Eq.2.42. An alternative representation of fidelity of entanglement has been obtained by Badziag et al. [63]:

$$F(\hat{\rho}) = \frac{1 + \lambda_1 + \lambda_2 - \text{sgn}[\det(\tilde{R})]\lambda_3}{4}, \tag{2.47}$$

where $\tilde{R}$ is a 3×3 matrix with elements defined as:

$$\tilde{R}_{i,j} \equiv Tr(\hat{\rho}\sigma_i \otimes \sigma_j). \tag{2.48}$$

Here, $\{\sigma_i, i = 1, 2, 3\}$ are the Pauli matrices, and $\{\lambda_i, i = 1, 2, 3\}$ are the ordered singular values of $\tilde{R}$, and sgn[det($\tilde{R}$)] is the sign of the determinant of $\tilde{R}$.

2.3.2 Two-photon State Tomography

As it is clear from Sec.2.3.1, in order to calculate the entanglement concurrence or fidelity of a two-qubit system, we have to first find its density matrix, $\hat{\rho}$. The method proposed by James et al. [62], starts with an initial guess for the density matrix, and then by optimizing a maximum likelihood function, that links the evaluated density matrix to the measurement results, a density matrix which best describes the system will be achieved.

General Form of the Density Matrix

A physical density matrix must satisfy the following conditions:

I. $\hat{\rho}$ is non-negative definite, i.e., for any state $|\psi\rangle$ we have:

$$\langle\psi|\,\hat{\rho}\,|\psi\rangle \geq 0. \tag{2.49}$$

II. $\hat{\rho}$ is Hermitian:

$$\hat{\rho}^\dagger = \hat{\rho}. \tag{2.50}$$

III. $\hat{\rho}$ is normalized,:

$$Tr(\hat{\rho}) = 1. \tag{2.51}$$

It is straightforward to show that any matrix written in the form $\hat{G} = \hat{T}^\dagger\hat{T}$ can exhibit the features we require. Regarding condition *I.*, we will find:

$$\langle\psi|\,\hat{G}\,|\psi\rangle = \langle\psi|\,\hat{T}^\dagger\hat{T}\,|\psi\rangle = \langle\psi'|\psi'\rangle \geq 0, \tag{2.52}$$

with $|\psi'\rangle = \hat{T}\,|\psi\rangle$. Also:

$$\hat{G}^\dagger = (\hat{T}^\dagger\hat{T})^\dagger = \hat{T}^\dagger(\hat{T}^\dagger)^\dagger = \hat{G}; \tag{2.53}$$

therefore, $\hat{G}$ is Hermitian. Now, division of $\hat{G}$ by its own trace will give us a normalized non-negative definite Hermitian operator:

$$\hat{g} \equiv \frac{\hat{G}}{Tr(\hat{G})} = \frac{\hat{T}^\dagger\hat{T}}{Tr(\hat{T}^\dagger\hat{T})}. \tag{2.54}$$

For a two-qubit system, $\hat{\rho}$ is a 4×4 matrix with 15 independent free parameters. One convenient representation of $\hat{T}$ is a tridiagonal matrix of the form:

$$\hat{T}(\mathbf{t}) = \begin{pmatrix} t_1 & 0 & 0 & 0 \\ t_5 + it_6 & t_2 & 0 & 0 \\ t_{11} + it_{12} & t_7 + it_8 & t_3 & 0 \\ t_{15} + it_{16} & t_{13} + it_{14} & t_9 + it_{10} & t_4 \end{pmatrix}, \tag{2.55}$$

with $\mathbf{t} = \{t_1, t_2, ..., t_{16}\}$ being the set of 16 parameters, out of which, 15 will be independent. Therefore, the density matrix of a two-qubit system will be written as:

$$\hat{\rho}(\mathbf{t}) = \frac{\hat{T}^\dagger(\mathbf{t})\hat{T}(\mathbf{t})}{Tr[\hat{T}^\dagger(\mathbf{t})\hat{T}(\mathbf{t})]}. \tag{2.56}$$

Projection Measurements

The Stokes parameters [64] can provide us with complete information about the polarization state of a light beam. Inspired by this fact, complete tomography of a two-qubit system can be achieved by performing multiple separate projection measurements in a combination of horizontal and vertical polarization basis, $|H\rangle\,\&\,|V\rangle$, diagonal and anti-diagonal polarization basis, $|D\rangle\,\&\,|A\rangle$, and right circular and left circular polarization basis, $|R\rangle\,\&\,|L\rangle$,

on the two subsystems. The polarization basis are defined as:

$$|H\rangle \equiv \begin{pmatrix} 1 \\ 0 \end{pmatrix} \tag{2.57}$$

$$|V\rangle \equiv \begin{pmatrix} 0 \\ 1 \end{pmatrix} \tag{2.58}$$

$$|D\rangle \equiv \frac{|H\rangle + |V\rangle}{\sqrt{2}}, \tag{2.59}$$

$$|A\rangle \equiv \frac{|H\rangle - |V\rangle}{\sqrt{2}}, \tag{2.60}$$

$$|R\rangle \equiv \frac{|H\rangle - i\,|V\rangle}{\sqrt{2}}, \tag{2.61}$$

$$|L\rangle \equiv \frac{|H\rangle + i\,|V\rangle}{\sqrt{2}}. \tag{2.62}$$

We shall represent the set of these six polarization basis as $\mathbb{P} = \{|H\rangle, |V\rangle, ..., |L\rangle\}$. These six basis, give rise to a maximum of 36 possible projection measurements for a two-qubit system to be performed, i.e., projections along the states $|HH\rangle, |HV\rangle$, etc. Use of a half-wave plate, HWP, a quarter-wave plate, QWP, and a linear polarizer provides us with all the sufficient needs to conduct such measurements. Fig.2.9 shows a schematic view of the experimental setup.

For a single-qubit, in the $|H\rangle / |V\rangle$ basis, the operators attributed to a HWP, $\hat{U}_{HWP}$, and a QWP, $\hat{U}_{QWP}$, can be written as [62]:

$$\hat{U}_{HWP}(\alpha) = \begin{pmatrix} \cos(2\alpha) & -\sin(2\alpha) \\ -\sin(2\alpha) & -\cos(2\alpha) \end{pmatrix}, \tag{2.63}$$

$$\hat{U}_{QWP}(\beta) = \frac{1}{\sqrt{2}} \begin{pmatrix} i - \cos(2\beta) & \sin(2\beta) \\ \sin(2\beta) & i + \cos(2\beta) \end{pmatrix}, \tag{2.64}$$

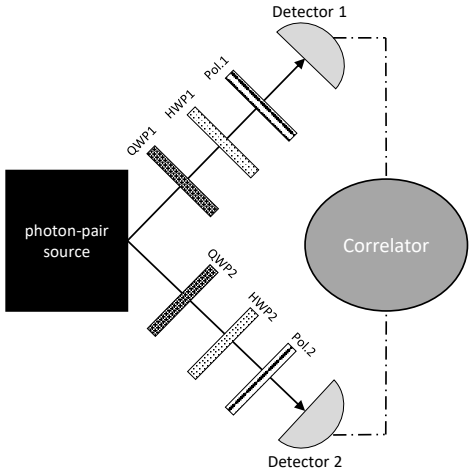

Figure 2.9: **Schematic veiw of the experimental setup for two-photon state tomography.** A half-wave plate, HWP, a quarter-wave plate, QWP, and a polarizer, Pol., is used to perform a projection measurement on each photon. The correlation between the separate projection measurements, gives the information we need to construct the density matrix of the two-qubit state. Image taken from Ref. [62].

where, α and β are the angles the HWP and the QWP make with the vertical axis, respectively. For any arbitary input polarization state $|\psi\rangle$, the effect of passing through a HWP$-$QWP setup can be written in the general form:

$$\hat{U}_{HWP}(\alpha).\hat{U}_{QWP}(\beta)\,|\psi\rangle = a(\alpha,\beta)\,|H\rangle + b(\alpha,\beta)\,|V\rangle\,, \tag{2.65}$$

where, a and b are complex-valued functions of α and β. The set of angles (α,β) gives us the complete freedom to project any arbitary input state onto a reference linear polarization state, e.g., $|H\rangle$, which matches the direction of the linear polarizer. In other words, one can think of a particular combination of the angles $(\alpha,\beta)_\nu$, as a projection measurement $\hat{\mu}_\nu = |\psi_\nu\rangle\langle\psi_\nu|$, with $|\psi_\nu\rangle \in \mathbb{P}$. For the case of having the linear polarizer aligned with $|H\rangle$, sets of angles for different projection measurements are given in Table.2.1.

Table 2.1: Set of angles for each single-qubit projection measurement. Note that in general the set of angles is not unique.

$\|\psi_\nu\rangle$	α	β
$\|H\rangle$	0°	0°
$\|V\rangle$	45°	0°
$\|D\rangle$	22.5°	-45°
$\|A\rangle$	-22.5°	-45°
$\|R\rangle$	0°	-45°
$\|L\rangle$	$-22.5°$	0°

The joint projection measurement of the two subsystems A and B, $\hat{M}_{\nu,\gamma} = |\Psi_{\nu,\gamma}\rangle\langle\Psi_{\nu,\gamma}|$, can be performed by the set of angles $[(\alpha_1,\beta_1)_\nu,(\alpha_2,\beta_2)_\gamma]$ for HWP1, QWP1, HWP2 and QWP2, respectively. Such a combination will project the two-qubit state $|\Psi\rangle$ onto $|\Psi_{\nu,\gamma}\rangle = |\psi_\nu\rangle_A \otimes |\psi_\gamma\rangle_B \in \mathbb{P}\otimes\mathbb{P} = \{|HH\rangle, |HV\rangle, ...\}$; where, the indices shows which subsystem is projected onto what state.

The Likelihood Function

In each case, the expectation value, $\bar{n}_{\nu,\gamma}$, of the projection measurement is given by:

$$\bar{n}_{\nu,\gamma} = \mathcal{N}\, Tr(\hat{\rho}, \hat{M}_{\nu,\gamma}) = \mathcal{N} \left\langle \Psi_{\nu,\gamma} | \hat{\rho} | \Psi_{\nu,\gamma} \right\rangle , \tag{2.66}$$

where $\hat{\rho}$ is the density matrix of the two-qubit state and $\mathcal{N}$ is a constant dependant on the emission rate of the source and the efficiency of the setup and detectors. The 15 independent parameters of the density matrix and the constant $\mathcal{N}$ make a total of 16 unknowns to be sought after. This means there should be a minimum of 16 projection measurements in order to achieve a full tomography of the two-qubit state. For the sake of simplicity, lets number the projection measurements $\hat{M}_{\nu,\gamma}$ as $\hat{M}_i$, projected states $\left|\Psi_{\nu,\gamma}\right\rangle$ as $|\Psi_i\rangle$ and the expectation values $\bar{n}_{\nu,\gamma}$ as $\bar{n}_i$; with $i \in \{1, 2, 3, ... N\}$, where N is the total number of performed projection measurements and in the range $16 \leq N \leq 36$.

By assuming a Gaussian probability distribution for the measured coincidence counts, the probability of gaining a particular value of coincidence count n_i for the projection measurement $\hat{M}_i$ is given by:

$$p_i \propto \exp\left[-\frac{(\bar{n}_i - n_i)^2}{2\sigma_i^2} \right], \tag{2.67}$$

where $\sigma_i \approx \sqrt{n_i}$ is the standard deviation of the coincidence counts. Now, for a given set of measured coincidence counts $\mathbf{n} = \{n_1, n_2, ..., n_N\}$, the probability that a density matrix $\hat{\rho}(\mathbf{t})$, described by Eq.2.56, will explain the measured results is given by:

$$P(\mathbf{t}, \mathbf{n}) \propto \prod_{i=1}^{N} \exp\left[-\frac{(\mathcal{N} \left\langle \Psi_i | \hat{\rho}(\mathbf{t}) | \Psi_i \right\rangle - n_i)^2}{2\mathcal{N} \left\langle \Psi_i | \hat{\rho}(\mathbf{t}) | \Psi_i \right\rangle} \right]. \tag{2.68}$$

The optimized set of parameters $\mathbf{t}^{opt} = \{t_1^{opt}, t_2^{opt}, ...\}$ will result in a maximum value for $P(\mathbf{t}, \mathbf{n})$, and the resultant density matrix $\hat{\rho}(\mathbf{t}^{opt})$ is the density matrix that *most likely* describes the two-qubit state. However, it is computationally much simpler, but, mathematically equivalent, to maximize

$$\ln\left[P(\mathbf{t}, \mathbf{n})\right] = -\sum_{i=1}^{N} \left[\frac{(\mathcal{N} \left\langle \Psi_i | \hat{\rho}(\mathbf{t}) | \Psi_i \right\rangle - n_i)^2}{2\mathcal{N} \left\langle \Psi_i | \hat{\rho}(\mathbf{t}) | \Psi_i \right\rangle} \right] + c, \tag{2.69}$$

instead of $P(\mathbf{t}, \mathbf{n})$ itself. With c being a constant, the optimization problem is reduced to finding the set $\mathbf{t}^{opt}$ which *minimizes* the function:

$$\mathcal{L}(\mathbf{t}) = \sum_{i=1}^{N} \left[\frac{(\mathcal{N} \langle \Psi_i | \hat{\rho}(\mathbf{t}) | \Psi_i \rangle - n_i)^2}{2\mathcal{N} \langle \Psi_i | \hat{\rho}(\mathbf{t}) | \Psi_i \rangle} \right]. \tag{2.70}$$

The optimization was carried out in `Python` computing language, by a routine `minimize()` function from the `scipy.optimize` library. We used the "Powell" method to execute the minimization function. Initially, the set of parameters $\mathbf{t}$ is set to 1, i.e., $\mathbf{t} = \{1, 1, ... 1\}$. At each iteration, the normalization factor $\mathcal{N}$ is calculated from the set $\mathbf{t}$ in the following way:

$$\mathcal{N} = \frac{\sum_{i=1}^{N} n_i}{\sum_{i=1}^{N} \langle \Psi_i | \hat{\rho}(\mathbf{t}) | \Psi_i \rangle}, \tag{2.71}$$

and substituted back to Eq.2.70.

Chapter 3

Dephasing free photon entanglement with a quantum dot

Generation of photon pairs from quantum dots with near-unity entanglement fidelity has been a long-standing scientific challenge. It is generally thought that the nuclear spins limit the entanglement fidelity through spin flip dephasing processes. However, this assumption lacks experimental support. Here, we show two-photon entanglement with negligible dephasing from an Indium rich single quantum dot comprising of nuclear spin 9/2 when excited quasi-resonantly. This finding is based on a significantly close match between our entanglement measurements and our model that assumes no dephasing and takes into account the detection system's timing jitter and dark-counts. We suggest that neglecting the detection system is responsible for the degradation of the measured entanglement fidelity in the past and not the nuclear spins. Therefore, the key to unity entanglement from quantum dots comprises of a resonant excitation scheme and a detection system with ultra-low timing jitter and dark-counts.

3.1 Introduction

Quantum dots can generate polarization entangled photons through the biexciton-exciton cascade [23, 65, 66]. Understanding how this process can yield perfect polarization entanglement has been a significant scientific challenge for more than a decade. Still, the experimental demonstration of perfect entanglement from quantum dots (QDs) remains elusive [67, 68]. The reason is twofold. First, QDs must emit perfectly entangled photons, and second, the detection system must be capable of measuring it without degrading its value [69]. Up to now, the detrimental effects of the detection system have been mostly ignored. Nonetheless, they are of equal importance to the photon generation process as timing jitter and dark-counts can spoil the measured entanglement. Here, we show that it is possible to reach entanglement with negligible dephasing from QDs by considering both the generation and detection processes of the entangled photons. We construct a model assuming no dephasing and demonstrate a high degree of agreement with our measurements indicating that the investigated quantum dot possesses negligible dephasing. The discovery of dephasing free entanglement generation from a QD makes reaching perfect entanglement in the future merely a technical one.

3.2 Results

3.2.1 Dephasing

We start by discussing the physics of how perfect entanglement between the biexciton and the exciton photon can be degraded. Due to the optical selection rules, the spin orientation of the decaying biexciton or exciton electron-hole pair projects onto a certain polarization state. Therefore, we must only analyze how the spins of the biexciton and exciton can loose their spin information.

For that, it is crucial to understand that the spin information, responsible for the entanglement generation, can only be destroyed through magnetic fields interacting with

the exciton spin. The biexciton remains unaffected as its singlet state does not allow spin flips nor is its energy split through magnetic fields. Thus, we can solely focus our analysis on the exciton with its net one spin. The exciton is influenced by two kinds of magnetic fields. First, nearby spins carried by free or trapped [70] charge carriers or nuclei can lead to an interaction via spin flips. Second, effective magnetic fields caused by electric fields through the spin-orbit coupling can interact with the exciton spin. These electric fields can be decomposed into a static and a time varying contribution. Static fields can reduce the symmetry of the crystal field and are responsible for the so-called fine-structure splitting [71] leading to a precession of the exciton spin [72, 73]. Still, this effect is only unitary and leaves the entanglement of the state unaffected, and the possibility of reducing it to approximately zero values ($\simeq 0.1\,\mu$eV) has been predicted theoretically as well as shown experimentally [74, 37, 43, 52, 75, 76, 77]. However, fluctuating fields from free charge carriers and their spins can lead to dephasing of the quantum state. With a (quasi)-resonant excitation scheme spin and charge noise from free carriers can be greatly suppressed [27]. Thus, under a (quasi)-resonant excitation scheme the magnetic field fluctuations from the nuclei should be the only remaining significant source of dephasing. In contrast to assumptions in other works [67, 68, 78] we find that this is not a significant source of dephasing and reveal that these interactions are negligible.

In a previous work, it was shown that the nuclear field affects neutral excitons much less than charged exciton complexes [79]. Therefore, the neutral exciton should dephase on an even longer timescale than a charged exciton complex and be negligible during the radiative exciton decay of $\sim 1\,$ns. This argumentation has been shown to be valid by a study revealing that the neutral exciton spin in InAs quantum dots is not affected by dephasing during the entire radiative lifetime of $\sim 2.5\,$ns [80]. Remarkably, this result was measured on a system with a large Indium content, an element with a significant nuclear spin of $9/2$, which has been previously thought to limit dephasing free entanglement [67, 68, 78]. Furthermore, spin-noise measurements [81] suggest a strong noise suppression at frequencies on the timescale of the exciton lifetime. Our measurements on a wurtzite InAsP quantum dot in a tapered InP nanowire [82] are in good agreement with the above argumentation and reveal that under quasi-resonant excitation the exciton spin does not

dephase over the entire exciton decay time of $\sim 5\,\text{ns}$. On the contrary, when excited non-resonantly the excess charges introduce significant dephasing setting in after ~ 0.5 ns.

3.2.2 Quasi-resonant versus non-resonant excitation

Fig.3.1(a) shows a photoluminescence (PL) spectrum of the QD under study indicating the resonances and the QD s-shell transitions. The peak at 830 nm is the wurtzite InP nanowire band-gap transition [82] and we excited the quantum dot at this wavelength to study the effect of dephasing. In contrast, for the dephasing free measurements we excited at $\sim 870\,\text{nm}$ where there are a manifold of peaks which stem from donor-acceptor transitions and not from the QD's p-shell transitions since these lines were uncorrelated with the QD s-shell transitions [46, 82]. Due to the background n-doping ($\approx 1 \cdot 10^{16}\,\text{cm}^{-3}$, Supplementary Information of Ref. [83]) of the nanowire the PL spectrum for the two excitation schemes is quite different. In the case of non-resonant excitation, shown in Fig.3.1(b), only three clean peaks from the QD are visible attributed to the exciton (X), the biexciton (XX), and the negatively charged exciton (X^-). In case of quasi-resonant excitation (870 nm), Fig.3.1(c), the X^- is suppressed as the quantum dot s-shell is already filled with electrons due to the background n-doping and holes are more mobile so they can more readily relax into the quantum dot. Here, the positively charged exciton (X^+) dominates the X^- line.

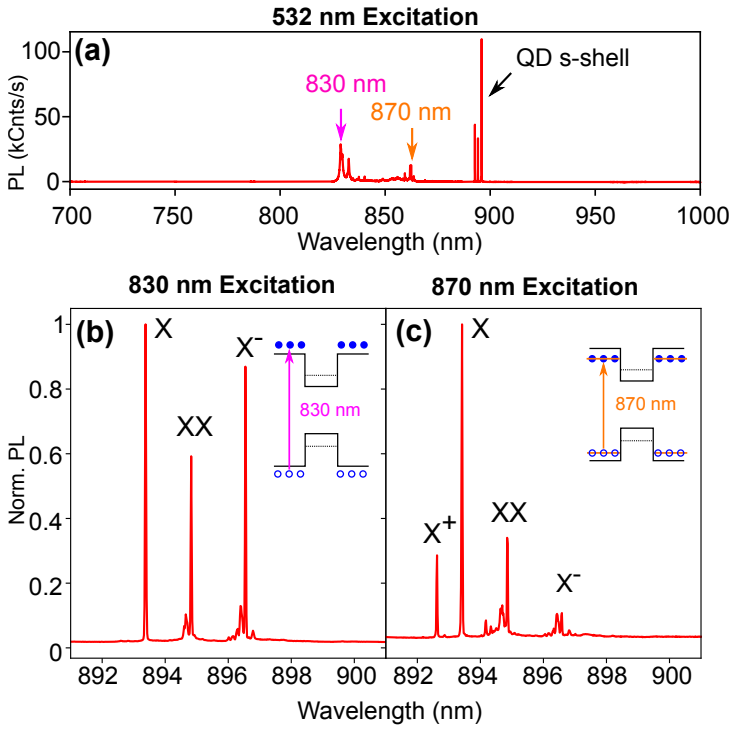

Figure 3.1: **QD emission spectra.** **(a)** Wideband emission spectrum excited with a green laser. For the entanglement measurements two excitation wavelengths have been used indicated by an arrow at 830 nm and at 870 nm. **(b)** Higher resolution spectrum of the QD emission at 830 nm excitation showing three clean peaks attributed to the exciton (X), biexciton (XX), and negatively charged exciton (X^-) at saturation. **(c)** Increasing the excitation wavelength to 870 nm leads to a different spectrum where X^- is suppressed and the positively charged exciton (X^+) appears. All spectra in panels a-c were recorded at saturation.

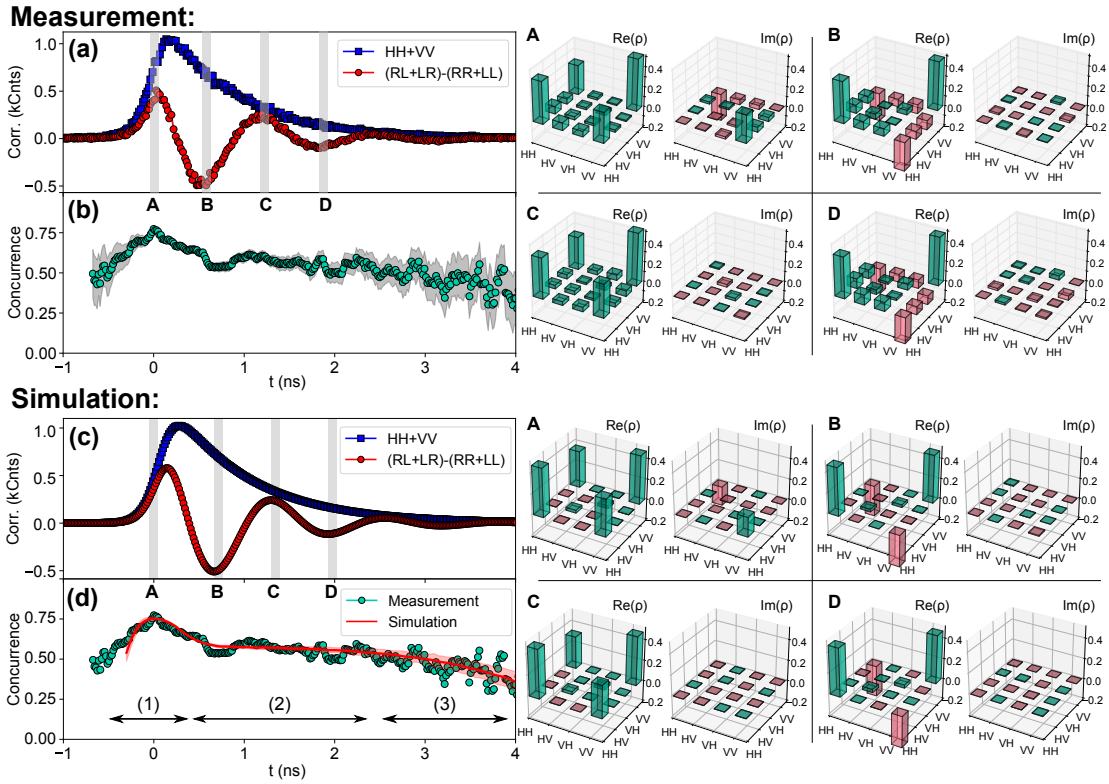

Figure 3.2: **Dephasing free entanglement.** **(a)** Two-photon correlation measurements depicting the sum of the HH plus VV projections together with $(RL + LR) - (RR + LL)$ showing quantum oscillations. The quantum oscillations appear because the latter term is proportional to the difference of the Bell states $\Phi^+ = 1/\sqrt{2}\,(|RL\rangle + |LR\rangle)$ and $\Phi^- = 1/\sqrt{2}\,(|RR\rangle + |LL\rangle)$. The gray shaded areas indicate times with the highest concurrence (**A**) and times with the smallest imaginary value of the density matrix (**B - D**). **(b)** The concurrence extracted from the measurement as a function of time delay, t, for all 36 projections. Each data point contains the correlation counts for a $\Delta t = 100\,\mathrm{ps}$ time window. The gray area indicates a 2σ concurrence error based on counting statistics. **(c)** The simulation shows the outcome of a fit free model of the quantum dot which is in close agreement with the measurement shown in **(a)**. The gray shaded areas indicate times with the highest concurrence (**A**) and times with the smallest imaginary value of the density matrix (**B - D**). **(d)** The concurrence measurement (green solid circles) is superimposed with the simulation (solid red line). The simulation is in very good agreement with the measurement over the entire exciton lifetime indicating dephasing free entangled photon generation.

At XX saturation, detected count rates of 940 kCnts/s for the X and 400 kCnts/s for the XX have been recorded with pulsed quasi-resonant excitation at a 76.2 MHz repetition rate and with the quantum state analysis optics removed. The setup efficiency in that case was 6.3 % from the first lens until a detected photon. This detected count rate corresponds to a high photon-pair source efficiency of 1.63 %, which is two orders of magnitude brighter than a quantum dot entangled photon source in the bulk [84].

In the following, we show that our results exhibit a strong indication of a dephasing free source of entangled photons. This finding suggests that it is possible to reach perfect entanglement from quantum dots, which is in stark contrast to the common understanding [67, 68, 78] that quantum dots cannot reach 'perfect' entanglement due to dephasing mechanisms such as interaction with nuclei. To explain our findings we use a model of a dephasing free biexciton-exciton cascade. First, we focus on the results of the quasi-resonant excitation scheme and find a close match to the dephasing free model. Second, we compare this quasi-resonant excitation scheme with non-resonant excitation at 830 nm to show the effect of dephasing.

3.2.3 Quasi-resonant excitation matches dephasing free model

The entanglement results of the quasi-resonant excitation scheme are shown in Fig. 3.2 while the comparison between these two excitation schemes will be discussed subsequently. For the biexciton-exciton cascade we expect to measure a quantum state of the form [69]:

$$|\Psi(t,\delta)\rangle = \frac{1}{\sqrt{2}}\left(|HH\rangle + e^{-i\frac{\delta}{\hbar}t}\,|VV\rangle\right)\Theta(t), \tag{3.1}$$

where δ represents the fine-structure splitting (FSS) energy, t the time after the biexciton emission, and $\Theta(t)$ the Heaviside step function accounting for the fact that the X photon is created after the XX photon. We denote here the 36 possible correlations within a time interval Δt as N_{ij} with $i,j \in \{H,V,D,A,R,L\}$ the measurement polarization projections as H/V (horizontal/vertical), D/A (diagonal/anti-diagonal), and R/L (right/left). Here, i and j represent polarization of the X and XX analyzer, respectively. With that, the

likelihood p_{ij} of measuring a correlation in the projection $\langle ij|$ within Δt reads as

$$p_{ij} = \left(|\langle ij|\Psi(t,\delta)\rangle|^2 \, n(t,\tau_X) \right) * g(t)\Delta t, \tag{3.2}$$

where $n(t,\tau_X) = 1/\tau_X e^{-t/\tau_X}$ describes the probability of an exciton decay with time constant τ_X, $*$ the convolution, and $g(t)$ denotes the detector systems' time resolution function. Therefore, the number of measured correlation counts per time bin becomes $N_{ij} = p_{ij} N_0 \Delta t$ where N_0 is the number of collected biexciton-exciton pairs.

Based on this mathematical description, the decay of the sum of the correlation counts $HH + VV$ is proportional to the exciton lifetime, τ_X. We plotted the sum of these correlation counts, $HH + VV$, with blue squares in Fig. 3.2 (a) from which we extracted $\tau_X = 847 \pm 6\,\text{ps}$. Furthermore, equation A.1 describes an oscillation of the quantum state between the two Bell states $|\Phi^+\rangle = \frac{1}{\sqrt{2}}(|RL\rangle + |LR\rangle)$ and $|\Phi^-\rangle = \frac{1}{\sqrt{2}}(|RR\rangle + |LL\rangle)$ with a period of $\hbar/\delta$. Therefore, plotting the measured correlations $(RL + LR) - (RR + LL)$ reveals quantum oscillations [72, 73] between the two Bell states as shown by red circles in Fig. 3.2 (a). The quantum oscillation allowed us to accurately measure the FSS to be $795.52 \pm 0.35\,\text{MHz}$, an accuracy which is unachievable with typical spectroscopic techniques [85]. We note that the exciton lifetime and FSS completely describe the quantum state evolution as noted in equation A.1.

For the entanglement measurements in Fig. 3.2 the QD was excited very close to saturation with an excitation power of 112 nW. The correlations between the X and XX photons were measured in all possible 36 projections [86] $|ij\rangle$, instead of the minimal necessary [62] 16. This enabled us to perform a better density matrix reconstruction based on a maximum likelihood approximation [62, 87]. We calculated the density matrices using multiple time windows with a width of $\Delta t = 100\,\text{ps}$ during the radiative decay of the exciton. Four representative density matrices are shown in the inset of Fig. 3.2. Inset A represents the density matrix at the highest measured concurrence. Interestingly, there is an imaginary contribution even though equation A.1 predicts no imaginary part at $t = 0$. The cause of this effect is the finite time resolution of the employed avalanche photodiode single photon detectors that averages the phase of the exciton spin precession. In contrast, the density matrices presented in insets B, C, and D were chosen with the

smallest imaginary parts. Similarly, the finite detector time resolution is responsible that smallest imaginary parts are not observed at the extrema of the quantum oscillations, but slightly time delayed.

For a complete picture of the entanglement time evolution the concurrence $\mathcal{C}(\rho)$, defined in Ref. [60], is a more suitable way of analyzing the entanglement strength of the density matrix ρ. The concurrence scales between zero and one [60], whereby it is one in the case of the system being fully entangled and zero if the system exhibits only classical correlations. Fig. 3.2 (b) shows the concurrence evolution as a function of time delay where each point was calculated based on the correlations within a $\Delta t = 100\,\mathrm{ps}$ time window. The concurrence reaches a maximum of $\mathcal{C} = 0.77 \pm 0.02$, while a counts weighted concurrence average over the whole time window yields $\bar{\mathcal{C}} = 0.62 \pm 0.03$.

In Fig. 3.2 (c-d) we compare the measured result with a simulation assuming a dephasing free QD without any free parameters. Our model, based on equation A.2, only considers the finite detection time response, the dark-counts, the FSS, the finite $g^{(2)}(0)$ of the XX photon, the detected count rates, and the exciton lifetime that were all determined from the experimentally measured ones. To get a more realistic implementation we added the detectors' dark-counts to the number of correlations of each projection (N_{ij}) before calculating the density matrix ρ_{dc} based on a maximum likelihood approximation. The finite $g^{(2)}_{XX}(0)$ of the biexciton will spoil the entanglement generation in $g^{(2)}_{XX}(0)$-fraction of the cases. This degrades the entanglement fidelity, but is not a source of dephasing. As shown in Fig. A.1 the power dependent $g^{(2)}$ remains flat at a level of $g^{(2)}(0) = 0.003 \pm 0.003$ for the X and $g^{(2)}(0) = 0.10 \pm 0.01$ for the XX up until the XX saturation point of 640 nW. Therefore, we can add-mix uncorrelated light to ρ_{dc} as

$$\rho_{sim}(t) = \left(1 - g^{(2)}_{XX}(0)\right) \rho_{dc}(t) + g^{(2)}_{XX}(0)\frac{\mathbb{I}}{4}, \tag{3.3}$$

where $\rho_{sim}(t)$ is the result of the simulation, and $\mathbb{I}/4$ is the density matrix for uncorrelated light, $\frac{1}{4}\left[|HH\rangle\langle HH| + |HV\rangle\langle HV| + |VH\rangle\langle VH| + |VV\rangle\langle VV|\right]$.

As it can be seen, a high degree of agreement between the model and measurement is achieved without any free parameters. To get a more quantitative number it is best to

compare the correlation counts weighted concurrence average $\bar{\mathcal{C}}$ over the full time window. From the simulation we obtain $\bar{\mathcal{C}}(\rho_{sim}) = 0.61 \pm 0.01$, whereas from the measurement this yields $\bar{\mathcal{C}}(\rho) = 0.62 \pm 0.03$. These results agree within their error bounds, further exemplifying their very good agreement. We therefore conclude that our quantum dot shows negligible dephasing over its entire lifetime.

In addition to the very good agreement of the concurrence, we also see that the density matrices match well between the measurement and the simulation as shown in the insets of A-D. Of particular interest is inset A. Both the simulation as well as the measurement exhibit non-vanishing imaginary parts. The reason for this observation is phase averaging during the exciton precession caused by the finite time resolution of the detectors. This effect has been seen before [73], but a convincing explanation has remained elusive.

Another supporting fact is the close to perfect agreement of the concurrence simulation with the concurrence extracted from the measurement depicted in Fig. 3.2 (d). Here, we identify three regimes: (1) the 'top'-part; (2) the 'flat'-part; and (3) 'roll-off'-part. The 'top'-part exhibits a concurrence maximum because the concurrence first rises as the detector response function $g(t)$ samples more and more correlation counts with evolving time, t. At a certain level; however, the phase averaging of the exponential term in equation A.1 dominates and the concurrence falls. Once the whole $g(t)$ function samples the state evolution, the phase averaging remains constant, named the 'flat'-part. With evolving time less correlations are measured due to the exponential decay of the X photon, which is when we enter the 'roll-off'-part where the concurrence drops due to the detector dark-counts. It is important to note that the whole entanglement evolution with its three parts can be completely described without any dephasing from the QD. The three regimes are solely caused by the finite time resolution and dark-counts from the detection system.

3.2.4 Non-resonant excitation induces dephasing

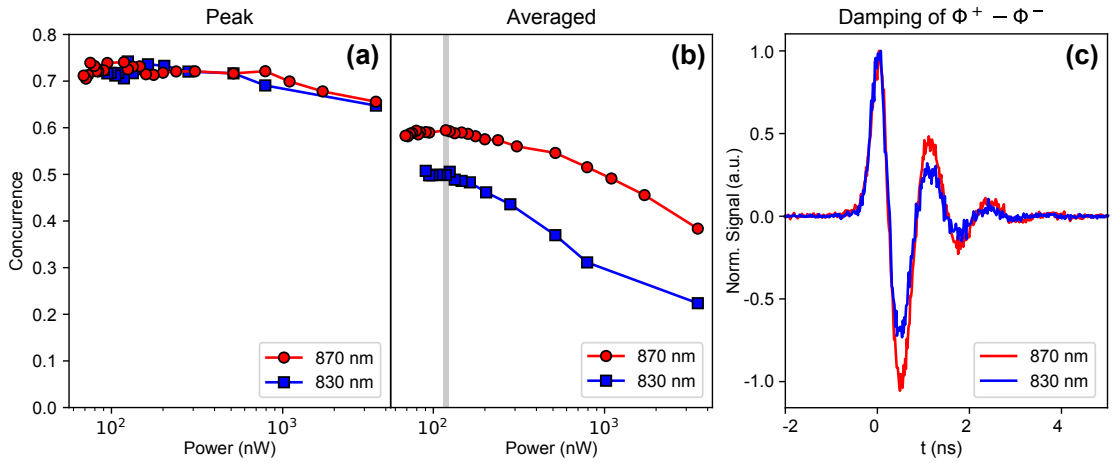

Figure 3.3: **Power dependent entanglement measurements.** **(a)** Peak concurrence calculated based on the two-photon correlation counts measured within a 200 ps wide window for both the quasi- and non-resonant case. There is no significant difference between the case of quasi-resonant excitation (870 nm) and non-resonant excitation (830 nm). **(b)** Counts averaged concurrence over the entire time window for 830 nm and 870 nm excitation. In this situation, the non-resonant (830 nm) is smaller than the quasi-resonant (870 nm) excitation highlighting the effect of exciton dephasing. **(c)** The dephasing can also be visualized directly based on the normalized quantum oscillations when comparing both excitation schemes. The data is taken at the same excitation power as highlighted in gray from panel (b).

We now repeat the experiment with non-resonant excitation and compare it with the quasi-resonant excitation scheme. Fig. A.1(a) depicts the peak concurrence for the two different excitation schemes as a function of excitation power. Each data point is constructed by analyzing the correlation counts within a $\Delta t = 200\,\text{ps}$ time window centered at $t = 0$. The integration window is increased here to better cope with count differences in the power dependent measurements spanning more than a decade, but does not influence the outcome of the analysis otherwise. The result reveals that both excitation schemes provide

the same power dependent peak concurrence measurement. The cause for the concurrence to drop at higher excitation power is the increase of the biexciton $g^{(2)}$-value which is not a dephasing effect. The situation is quite different when we compare the correlation weighted concurrence average over the full time window as presented in Fig. A.1 (b). Clearly, the data for 830 nm excitation shows $\sim 15\,\%$ smaller concurrence as compared to the quasi-resonant case at low powers, while deviating further at higher powers. This result is expected from the excess charges generated by non-resonant excitation. First, the spin of these charges can cause direct spin flip-flop processes with the exciton spin. Second, fluctuating electric fields caused by the excess charges can result in an effective magnetic field via the spin-orbit interaction and alter the exciton spin. This situation is directly visible in Fig. A.1 (c) where the normalized quantum oscillations are compared with each other. The two curves were recorded at the same power level highlighted by the shaded region in Fig. A.1 (b). The 830 nm data clearly damps out faster than the 870 nm one, which is the fingerprint for dephasing.

To show the dephasing effect more quantitatively we simulated the two cases as presented in Fig. 3.4. Please note that Fig. 3.4 (a)/(b) were recorded at the same excitation power (118 nW) indicated with the gray bar in Fig. A.1 (b) whereas the data in Fig. 3.2 (a) was recorded at a slightly lower power (112 nW). Again, the model in Fig. 3.4 (a) agrees with the quasi-resonant excitation scheme within error bars indicative for dephasing free entanglement. In contrast, the situation is very different for non-resonant excitation (Fig. 3.4 (b)) where the simulation clearly overestimates the measurement exemplifying dephasing.

3.2.5 The influence of the detection system

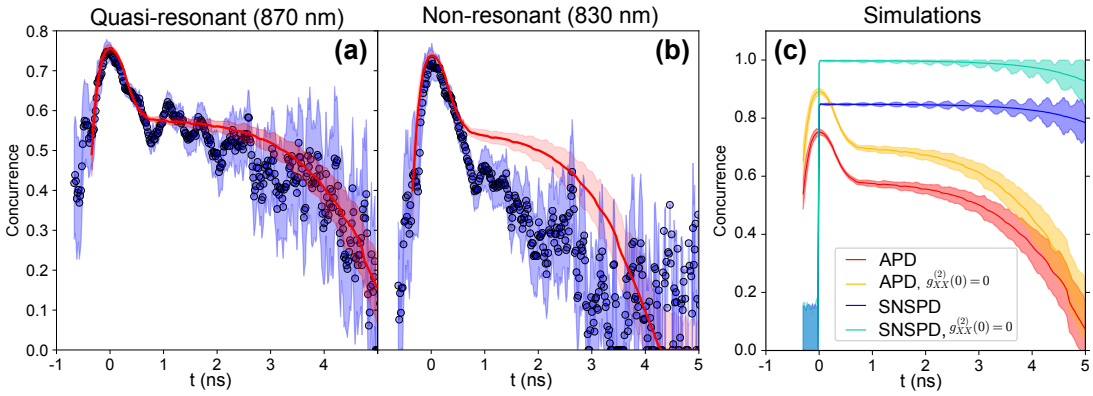

Figure 3.4: **Towards near-unity entanglement: comparison of dephasing and dephasing free entanglement. (a)** At quasi-resonant excitation the measured concurrence evolution agrees with the simulation within error bars, thus signifying dephasing free entanglement. **(b)** At non-resonant excitation the measured concurrence evolution does not match with the simulation indicating dephasing. The data in both (a) and (b) was taken from the two points highlighted in the gray region of Fig. 3b. **(c)** Four simulation curves illustrating the effect of finite detection time resolution and multiphoton emission of the biexciton photon. The red graph depicts the same simulation as already presented in Fig. 3.2 (d) with finite $g^{(2)}_{XX} = 0.1$ and the yellow graph the case for zero $g^{(2)}_{XX} = 0$ in both cases for a slow detection system based on an avalanche photodiode single-photon detector (APD) as a reference. The blue curve shows the outcome of a simulation similar to the red curve with finite $g^{(2)}_{XX} = 0.1$, but with a fast detection system based on a superconducting nanowire single photon detector (SNSPD) with 30 ps timing resolution. The cyan curve is the same as the blue curve with SNSPD, but for pure single photon emission of the biexciton photon (*i.e.*, with $g^{(2)}_{XX}(0) = 0$). Remarkably, with a fast detection system and perfect $g^{(2)}_{XX}$, near-unity entanglement is expected. dark-counts used in the simulation for the APDs are $36.3\,\mathrm{s}^{-1}$ and $18.2\,\mathrm{s}^{-1}$ for the X and XX detector respectively and for the SNSPDs are $1\,\mathrm{s}^{-1}$.

Finally, we investigate how the concurrence evolution of the data presented in Fig. 3.2 would look like if we were to measure with an emerging detection system employing a better timing resolution and lower dark-count rate. We assume a time resolution of 30 ps full width at half maximum and a dark-count rate of 1 Hz, values which can be met by recently available superconducting nanowire single photon detectors. The outcome of such simulations are plotted in Fig. 3.4 (c) for $g^{(2)}_{XX}(0) = 0$ and $g^{(2)}_{XX}(0) = 0.1$ and are compared to the case when measuring with our APDs in the situation of zero or finite $g^{(2)}_{XX}(0) = 0.1$ (*i.e.*, with the same plot as in Fig. 3.2 (d)). With APDs we get a peak concurrence of $\mathcal{C} = 0.75 \pm 0.01$ at finite $g^{(2)}_{XX}(0)$ and in case of zero $g^{(2)}_{XX}(0)$ the simulation predicts that we would measure a peak concurrence of $\mathcal{C} = 0.89 \pm 0.01$ but maintain the overall shape of the concurrence evolution. In both cases with 30 ps timing resolution, *i.e.*, with zero $g^{(2)}_{XX}(0)$ and finite $g^{(2)}_{XX}(0)$, the difference to the simulation with APDs is quite striking. First, the peak concurrence for finite $g^{(2)}_{XX}(0) = 0.1$ ($\mathcal{C} = 0.849 \pm 0.001$) and $g^{(2)}_{XX}(0) = 0$ ($\mathcal{C} = 0.999 \pm 0.001$) is significantly larger than for the case of measuring with APDs and finite $g^{(2)}_{XX}(0)$. Remarkably, the concurrence reaches near-unity for zero $g^{(2)}(0)$. Second, the shape of the curves have changed significantly. The 'top'-part is completely suppressed. Instead, only the 'flat'- and 'roll-off'-parts remain. It is interesting to note that even the small dark-count rate of 1 Hz is inducing a resolvable entanglement roll-off. However, this decrease at the end has minimal effect to the overall concurrence and a count averaged concurrence of $\bar{\mathcal{C}} = 0.996^{+0.004}_{-0.008}$ for zero $g^{(2)}_{XX}(0)$ and $\bar{\mathcal{C}} = 0.847 \pm 0.007$ in case of finite $g^{(2)}_{XX}(0)$ is obtained. The slight oscillations visible in the concurrence's error for the high temporal resolution simulation are not artefacts. They are caused by counting statistics since every time one of the 36 simulated correlations reaches zero the concurrence can be less accurately estimated. This happens with a frequency four times larger then the FSS. In fact, this effect is visible in other groups' measurements, for example in the fidelity evolution of Ref. [72]. For a slower detection system, such as our APDs, this effect is averaged out.

3.3 Discussion

We have shown that our model is capable of explaining our measurement results in great detail. The question arises why dephasing free entanglement from QDs has not been observed before. The reason is that a QD with a long X decay time of $\tau_X \sim 1\,\mathrm{ns}$ is needed in conjunction with a (quasi)-resonant excitation scheme. For example, in Refs. [27, 67] a resonant excitation scheme was employed, but the QDs had a $\tau_X \sim 200\,\mathrm{ps}$ which makes it very difficult to separate the detrimental effects from the detection system. However, based on model calculations, we predict that the QDs investigated in these aforementioned works of Refs. [27, 67] should also be dephasing free. Therefore, the occurrence of dephasing free entanglement is not at all limited to InAsP QDs, but should be equally achievable in other QD materials such as InGaAs [27], and GaAs [67].

Even though our results suggest existence of dephasing free entanglement, we have not yet shown unity concurrence. The reduction of the measured concurrence from unity comes mainly from the detectors' timing resolution, finite $g^{(2)}_{XX}$-value of the QD, and dark-counts. Still, $g^{(2)}$-values of both the exciton and biexciton can be brought to zero by resonant excitation [27, 67, 29]. Therefore, in principle, the problem of reaching perfect entanglement using QDs should now be merely a technical one, which, in future work, can be resolved by combining the right source and excitation scheme with a state-of-the-art detection system. However, there are always challenges regarding the re-excitation of the s-shell[88], which may be addressed by using proper protocols [28, 89, 90].

3.4 Conclusion

We have established a precise model of the entanglement measurement in which the generation and the detection processes of entangled photon pairs are of equal importance. Based on this knowledge we could show that a QD containing Indium generates photon entanglement with negligible dephasing over the entire exciton decay time even though its large nuclear spin of 9/2. This result is remarkable as it indicates that perfect entanglement is

achievable in QDs in spite of interaction with nuclei possessing large nuclear spins. The conditions needed to resolve dephasing free entanglement are (quasi)-resonant excitation and a precise knowledge of the employed detection system. This new insight will allow to make an ideal entangled photon source based on QDs. Based on our model, we suggest that dephasing free entanglement should also be found in materials other than InAsP, such as InGaAs [27] and GaAs [67] QDs. However, the actual evidence can be presented once the resonant excitation schemes, as well as fast detectors with low dark-counts, are used to repeat the measurements.

3.5 Methods

3.5.1 Quantum Dot

The quantum dot growth is described in the Methods section of Ref. [85].

3.5.2 Measurement

We used a standard micro-PL setup where the nanowire sample was kept at a base temperature of 4.5 K. The light from a picosecond pulsed laser was filtered with a 1200 lines/mm grating to reduce the effect of laser background fluorescence before it was used to excite the QD. For the quantum state tomography we used a similar system as in Ref. [84] with the difference that the waveplates where mounted in high-precision motorized mounts crucial for the repeatability of the experiment. The first beam splitter used to excite the QD had 30 % reflection and 70 % transmission. The excitation was performed in all cases with s-polarized light to prevent nuclear polarization [91]. All correlation data was sampled with 16 ps resolution.

The data presented in Fig. 3.2 was excited with a power of 112 nW and integrated for 370 s per projection. Count rates were in HH projection 71 kCnt/s for the X and 8 kCnts/s for the XX. The data presented in Fig. 3.4 (a)/(b) was excited with a power of 118 nW and

integrated for 342 s per projection. In case of Fig. 3.4 (a) this resulted in a HH projection count rate of 85 kCnt/s for the X and 11 kCnts/s for the XX and for (b) in a HH projection count rate of 73 kCnt/s for the X and 4.4 kCnts/s for the XX.

The employed avalanche single-photon detectors (APDs) had a dark-count rate of $36.3\,\mathrm{s}^{-1}$ for the detector measuring the exciton and $18.2\,\mathrm{s}^{-1}$ for the biexciton detector with a time resolution of 290 ps full width at half maximum, compare Fig. 10 in the Supporting Information.

3.5.3 Simulation

For the simulation in the text we used a FSS = 795.520 MHz, a dark-count rate of $36.3\,\mathrm{s}^{-1}$ for the exciton and $18.2\,\mathrm{s}^{-1}$ of the biexciton detector, a exciton lifetime of $\tau_X = 847$ ps, a $g^{(2)}_{XX} = 0.1$, $g^{(2)}_{X} = 0$, and a laser repetition rate of 76.2 MHz. The used count rates and integration times are stated in the Measurement section. In case of Fig. 3.2 (b) an exciton lifetime of $\tau_X = 753$ ps was used.

The density matrix reconstruction was performed based on the code from Ref. [87]. The method of how to acquire the system's time resolution $g(t)$ is described in the Supporting Information.

The error of the concurrence is estimated based on a Monte-Carlo simulation assuming counting statistics. For each concurrence value the simulation was performed with 1000 repetitions.

Chapter 4

Resonant Two-photon Excitation

Here, we analyze the emission properties, e.g., pair-production efficiency, single-photon purity, etc., of an InAsP quantum dot (QD) in an InP photonic nanowire under resonant two-photon excitation (TPE). It is a first time report on resonant TPE of such sources. We have observed that, the multi-photon emission probability of the source is suppressed significantly as compared to non-resonant excitation of the same source, $g^{(2)}(0) = 0.0024$ and $g^{(2)}(0) = 0.0055$ for exciton and biexciton emissions, respectively; also, pair-production efficiencies above 93% is achieved. Moreover, by considering the efficiency of the setup, a pair-extraction efficiency $\epsilon = 12.55\%$ is achieved which suggests QDs can outperform spontaneous parametric down conversion sources in terms of entanglement fidelity vs. pair-extraction efficiency. These results indicate the powerful features of nanowire QDs, and bring us one step closer to a bright entangled photon source with near-unity entanglement fidelity.

4.1 Introduction

During the past couple of decades quantum dots (QDs) have been shown to be promising candidates for an ideal photon source [92], showing a high degree of single-photon purity

[28] and high degree of photon indistinguishability [29, 24]. In addition, it is possible to control different features of the QDs such as the wavelength of emitted photons [34, 33], flow and level of free charge carriers [29, 90], and remove the fine-structure splitting (FSS) [43, 52, 93, 76]. These features combined with the fact that QDs are capable of deterministic generation of pairs of entangled photons, through the biexciton(XX)-exciton(X) cascade, with high fidelity and negligible dephasing [37, 48], puts QDs as one of the most reliable photon sources for various applications in quantum information, quantum computing and quantum sensing.

Enhancing the emission quality of the QDs is done through both the improvement of the growth procedures, as well as excitation methods. Proper engineering of photonic structures around the QD can enhance the photon extraction efficiency [29, 24, 40], and also can reduce the emission time jitter by accelerating the spontaneous emission rate [29, 24, 94]. By applying an electric field to such structures the charge environment surrounding the QDs can also be controlled, which has been utilized to suppress the inhomogenous broadening of the emission lines and strengthen the indistinguishability of the photons [29].

On the other hand, proper schemes for excitation of the QDs are also needed to reveal the ultimate potential qualities of these quantum light sources. Until recently, off-resonant excitation was the main method used to excite the QDs. During this process, the charge carriers are excited to energy levels above the QD's s-shell, e.g., higher electronic shells (p-, d-) or band-gap of the host material, and then, through interaction with the phonons, the carriers will relax into the s-shell of the QD, recombine and emit light. This process, due to being incoherent, introduces detrimental effects originated in the abundance of the excessive charge carriers and their interaction with phonons; leading to flaws such as broadening of the emission lines [83], low single-photon purity due to re-excitation processes [95], emission time jitter [96], and low entanglement fidelity [48].

In order to overcome these challenges, specifically suppression of multi-photon emission and enhancing the pair-production efficiency of the QDs, a resonant two-photon excitation (TPE) scheme has been proposed. Over the past few decades, the two-photon absorption of

the neutral biexciton state, $|XX\rangle$, has been extensively studied in different semiconductor structures [97, 98, 99, 100]. Whereas, direct resonant excitation of $|XX\rangle$ is forbidden due to the optical selection rules, two-photon absorption, which is rooted in the specific symmetry of $|XX\rangle$ [101], can be used to coherently couple the ground state of the QD to its biexciton state and is referred to as resonant two-photon excitation (TPE). This process, exhibits the familiar Rabi oscillations in the population of the states with increasing excitation pulse area; however, in contrast to single-exciton Rabi oscillations, it is not purely sinusoidal [102]. Fig.4.1 shows a schematic view of the process. Initially, a laser pulse is tuned to a virtual state with the energy equal to $(E_{|XX\rangle} - E_{|G\rangle})/2$, where $E_{|XX\rangle}$ corresponds to the total energy of the biexciton state and $E_{|G\rangle}$ corresponds to the energy of the ground state. This energy level may as well be thought of as the energy level half-way between the energy of neutral exciton transition, $X \equiv |X\rangle \rightarrow |G\rangle$, and neutral biexciton transition, $XX \equiv |XX\rangle \rightarrow |X\rangle$. In other words, a laser pulse excites $|XX\rangle$ without being resonant to either X nor XX transition lines. This fact gives two-photon resonant excitation an advantage over the usual resonant excitation, since there will be no need for extinguishing the reflected laser pulse via polarizatoin suppression methods which can alter the polarization state of the emitted photons [103]. Furthermore, in order to create two electron-hole pairs with $j_z = \pm 1$, the laser pulse should be linearly polarized, a superposition of $|L\rangle \equiv |+1\rangle$ and $|R\rangle \equiv |-1\rangle$ polarizations.

In order to describe the dynamics of the system under resonant TPE, one can consider a Hamiltonian of the form:

$$H = \frac{\hbar\Omega(t)}{2}(\sigma_{G,X} + \sigma^{\dagger}_{G,X}) + \frac{\hbar\Omega(t)}{2}(\sigma_{X,XX} + \sigma^{\dagger}_{X,XX}) + \hbar\Delta_X\sigma_{X,X} \tag{4.1}$$

where $\Omega(t)$ is the Rabi frequency of the driving field, $\sigma_{i,j} = |i\rangle\langle j|$, represent the transition operators, and Δ_X is the difference between the energy of the TPE resonance and the X state. This difference can also be thought of as a detuning of the laser to the direct resonant excitation of the exciton state [103].

Furthermore, coupling of the carriers to the acoustic phonons, which are shown to be the dominant source of dephasing [104, 105], should also be considered. The strength of this coupling, and thus the attributed dephasing, depends on temperature and the driving

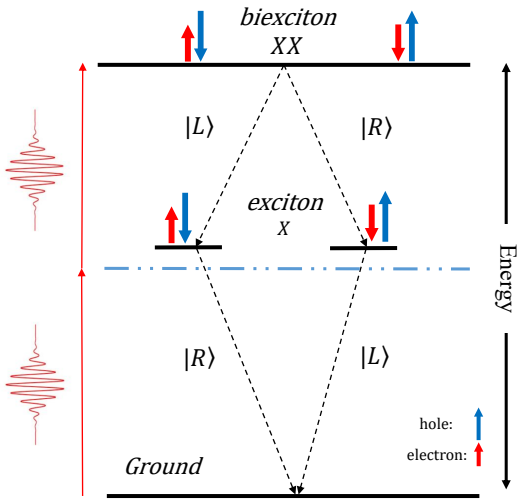

Figure 4.1: The scheme for resonant two-photon excitation. Mediated by a virtual state, dashed blue line, the ground state is coherently coupled to the XX state via absorption of two photons from a linearly polarized laser pulse. The laser pulse is tuned to the energy half-way between that of the X and XX emission lines.

field intensity. As a result, for higher field intensities, $\Omega(t) > \pi$, and higher temperatures a reduction in state population efficiency is observed [104, 106]. However, the same phenomenon creates states at the proximity of QD's s-shell, with $\delta E \sim$ 1mev, which can be used to populate $|XX\rangle$ through an incoherent two-photon process, referred to as phonon-assisted two-photon excitation[107, 108]. This method can in principle populate the $|XX\rangle$ with near unity fidelity, and slight fluctuations in field intensity and energy is not detrimental to state population; whereas, for resonant TPE, a proper control over the field intensity and energy is needed in order to achieve a high population efficiency [109, 110].

In this work, we present the results of resonant two-photon excitation of a QD inside a photonic nanowire for the first time, and investigate different features of the emitted photons under this scheme. The results indicate an enhancement in the quality of the QD in terms of pair-production efficiency as well as single-photon purity. We observe a significant suppression of multi-photon emission of the source, up to two orders of magnitude; as well

as, more than a five-fold enhancement in the pair-extraction efficiency as compared to non-resonant excitation [48].

4.2 Results

The Source

The source under study is an InAsP QD embedded in a wurtzite InP nanowire [40]. The emission spectrum exhibits an emission line at $\lambda \approx 830$nm, belonging to the wurtzite InP; and two s-shell emission lines at $E_{s\text{-shell}} \approx 1.38$ev, $\lambda_X = 893.32$nm and $\lambda_{XX} = 894.77$nm for X and XX transitions, respectively. Based on these values, the resonant TPE occurs at $\lambda = 894.05$nm. There are also emission lines due to charged exciton states. In addition, there are several lines attributed to donor/acceptor transitions in the range $\lambda_{D./A.} \approx 860\text{nm} - 870\text{nm}$, which can also be used to excite the quantum dot [48]. We call excitation at the wurtzite InP bandgap and the donor/acceptor levels, off-resonant excitation and quasi-resonant excitation, respectively.

Fig.4.2a shows the emission spectrum of the source under excitation above the wurtzite InP bandgap. The three emission regimes, i.e., wurtzite InP, donor/acceptor levels, and QD's s-shell, are clearly observed. Fig.4.2b focuses on the s-shell's emission under different excitation schemes, i.e., non-resonant, quasi-resonant, and resonant TPE. Under non-resonant excitation, the emission of the negatively charged exciton, X^-, is significantly higher as compared to X. Under quasi-resonant excitation, the charge environment surrounding the QD changes, and more emission lines appear in the spectrum. Here, there is an emission line which is attributed to a positively charged exciton, X^+, transition. Moreover, there is another emission line adjacent to XX transition which may be due to a charged biexciton transition. Overall, the charge noise under quasi-resonant excitation is believed to be lower than the non-resonant excitation, since, the entanglement fidelity measurements yield values equal to that of a source exhibiting no dephasing, even though, the imperfect $g^{(2)}(0)$ of XX photons limits the measured entanglement fidelity [48]. In

(a)

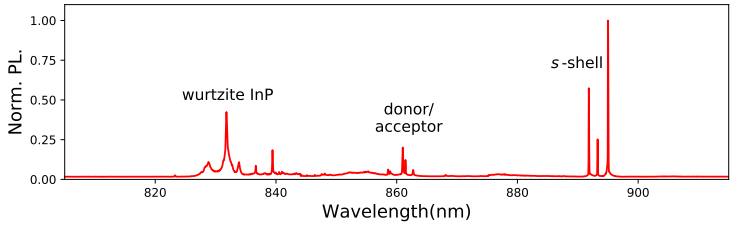

(b)

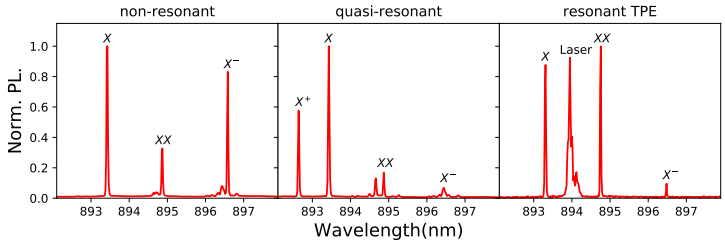

Figure 4.2: **QD's emission spectrum under different excitation schemes**. **(a)** Spectrum for above-bandgap excitation via a green laser, $\lambda_{\text{exc.}} = 530\text{nm}$. From the spectrum the emission lines attributed to the wurtzite InP nanowire, $\lambda \approx 830\text{nm}$, the emission lines attributed to the donors and acceptors, $\lambda_{D./A.} \approx 860\text{nm} - 870\text{nm}$, and QD's s-shell emission are visible. **(b)** QD's s-shell emission under non-resonant excitation, left, quasi-resonant excitation, middle, and resonant TPE, right.

both of these cases, the intensity of the XX transition is relatively low as compared to the X transition, which shows a poor pair-production efficiency. In other words, only a small fraction of X photons belong to a XX-X cascade. Under resonant TPE, the charge noise is substantially suppressed, and also, the intensities of XX and X transitions are close to each other, meaning, most of the excitons and biexcitons belong to the same cascade and are correlated.

4.2.1 State Population

In order to investigate the behavior of the QD under resonant excitation, both phonon-assisted and two-photon resonance excitation was conducted. For this matter, the pulsed laser is passed through a regular 4f-pulse-shaper, by which the bandwidth of the pulse was varied in order to reach efficient population.

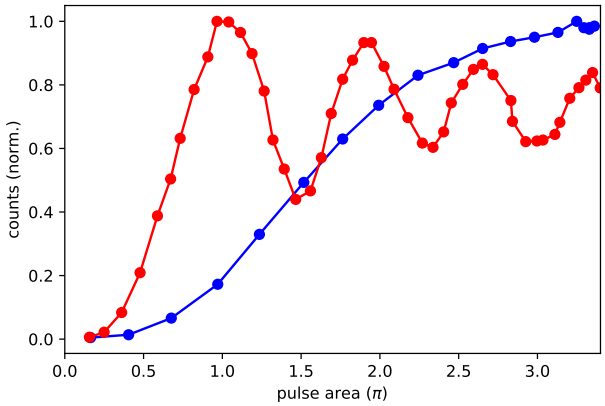

Figure 4.3: Comparison between XX power dependent count rate using TPE (red) and phonon-assisted (blue) excitation. The laser was tuned to 893.95nm for the case of phonon-assisted excitation.

Fig.4.3 shows the comparison between the power-dependant count rate measurement for XX when excited via resonant TPE (blue curve) and phonon-assisted TPE (red curve) excitation. The count rates are normalized to the maximum number of counts for each case and does not indicate 100% population of $|XX\rangle$. By a slight shift from the two-photon resonant point (≈0.15mev) the behavior of the QD changes and Rabi oscillations, which are indications of the resonance TPE, disappear. With the pulse area being proportional to the square root of the excitation power, it is seen that the phonon-assisted two-photon excitation reaches its saturation point at a power ≈10 times that of the π pulse. A similar behavior and a state population as high as 80% via phonon-assisted TPE has been previously reported [109]. In the case of resonant two-photon excitation, population efficiencies

as high as 98% has been reported [27]. In addition to the energy of the exciting pulse, the length and bandwidth of the pulse should also be optimized in order to suppress the interaction with phonons and populate the XX state solely through resonant TPE. In the latter case, reduction of the laser pulse bandwidth from 0.49mev, 119.64GHZ, down to 0.30mev, 72.65GHz resulted in the highest biexciton state population at the π-pulse. The temporal length of the pulse was not measured directly; however, considering a close to Fourier-limited pulse, which is justified by absence of chirp in the 4f-pulse-shaper and a r^2 value of greater than 0.99 by fitting the intensity profile of the pulse to a Gaussian distribution, the temporal length, Δt, can be estimated to be $\approx$ 7ps, since the time-bandwidth product, $\Delta t \Delta \nu$, for such a pulse is 0.441.

4.2.2 Linewidth and Pair-production

In order to see the effect of different excitation schemes on the emission linewidth, the QD emission lines were fitted to a Voigt distribution, $V(x, \sigma, \gamma) = G(x, \sigma) * L(x, \gamma)$, which is a convlution between a Gaussiang distribution, $G(x, \sigma)$, with the variance equal to σ, and a Cauchy-Lorentz distribution, $L(x, \gamma)$, with the linewidth equal to 2γ.

Upon resonant two-photon excitation, the linewidths for XX and X transition lines are measured to be 8.05GHz, 33.24μev, and 11.62GHz, 48.06μev, respectively. It should be noted that the resolution of the spectrometer is $\approx$ 7GHz. Under phonon-assisted TPE the linewidths are 10.10GHz and 7.10GHz for X and XX lines, respectively. Comparison of these values with the spectrum of the QD from off-resonant excitation yields interesting results. In the latter case an increase in excitation power can reduce the charge noise by filling the charge traps and thus shrink the emission linewidth [83]. For this sample, the emission spectrum from off-resonant and quasi-resonant excitation were analyzed. For the case of off-resonant excitation, linewidths as low as 10.29GHz and 9.00GHz, for X and XX lines, respectively, are observed. Previously, by using Michelson interferometry, linewidths as low as $\approx$ 1GHz for the X emission line has been reported for a similar source upon off-resonant excitation [83]. But, for the case of quasi-resonant excitation, X and XX linewidths are 10.89GHz and 10.20GHz, respectively.

Furthermore, we calculated the QD's pair-production efficiency, total XX emission divided by total X emission [111]. This was done by calculating the area under the Voigt distributions fitted to the emission lines. Basically, this number specifies what percentage of excitons belong to a XX-X cascade. We have achieved pair-production efficiencies as high as 84.09%($\pm$2.40%) and 93.66%($\pm$2.56%), for the cases of phonon-assited TPE and resonant TPE respectively. A degradation of pair-production efficiency in the phonon-assisted scheme is expected; since, the two-photon excitation can simultaneously be thought of as a detuned excitation of the $|X\rangle$ state. As the detuning is reduced and the probability of direct excitation of the exciton state through a detuned direct resonant excitation, increases. By considering the total efficiency of the experimental setup, in the case of resonant TPE at π-pulse, an overall pair extraction efficiency of 12.55% is obtained which shows an enhancement by a factor of $\approx$ 8 as compared to the case of quasi-resonant excitation in the same quantum dot sample [48].

4.2.3 Second-order Correlation

Lastly, we investigated the single-photon purity of our source under resonant TPE excitation. Considering a time window according to the lifetime of the emission lines, $\pm$1ns for X and $\pm$0.5ns for XX, yields values of $g^{(2)}(0) = 0.0024(\pm 0.0002)$ and $g^{(2)}(0) = 0.0055(\pm 0.0005)$ for X and XX lines, respectively, under resonant TPE at the π-pulse. Values are without any background subtraction and show more than one order of magnitude enhancement in the single-photon purity as compared to quasi-resonant excitation, which shows $g^{(2)}(0) = 0.10$ and $g^{(2)}(0) = 0.01$ for XX and X, respectively, with a time window of $\pm$50ps [48]. Fig.4.4a and Fig.4.4b show comparisons between the $g^{(2)}(0)$ measurements obtained under resonant TPE and quasi-resonant excitation for the X and XX emission lines, respectively.

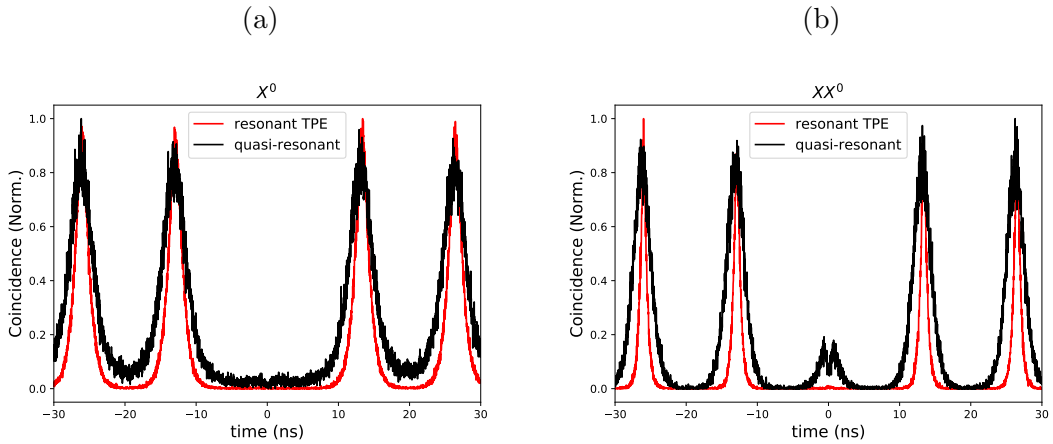

Figure 4.4: **Second-order correlation measurements** Comparison of $g^{(2)}(0)$ measurements obtained under resonant TPE and quasi-resonant excitation for X, **(a)**, and XX, **(b)**. The results clearly show the significant enhancement of the single-photon purity under resonant TPE.

4.3 Conclusion and Discussion

In this work we have investigated a QD inside a photonic nanowire under resonant two-photon excitation, which occurs at the energy half-way between that of X and XX transitions, as well as phonon-assisted two-photon excitation, which occurs at energies slightly blue-shifted from that of the resonant TPE. In both of these schemes, the linewidth for the X line exhibits a larger linewidth as compared to XX line, $\approx$ 10.8GHz vs. $\approx$ 7.5GHz. phonon-assisted TPE is observed to bring the XX to saturation at powers equal to $\approx 10\pi$, and the population efficiency at saturation is more stable upon slight changes in pulse power or energy. However, we have observed that phonon-assisted TPE is less efficient in pair-production as compared with resonant TPE, 84.09% vs. 93.66%. Resonant TPE shows a pair extraction efficiency of 12.55%, which is almost an eight-fold enhancement as compared to quasi-resonant excitation. In terms of single-photon purity, resonant TPE has improved the quality of our source by two orders of magnitude. Second-order correlation, $g^{(2)}(0)$, of the emission lines yields values as low as $24\,E^{-4}$ and $55\,E^{-4}$ for X and XX

respectively. These results show the potential of QDs embedded in photonic nanowires as a promising quantum light source; where, proper engineering of a photonic waveguide and excitation scheme results in a high pair-production and extraction efficiency, narrow emission linewidths, and low multi-photon emission probability.

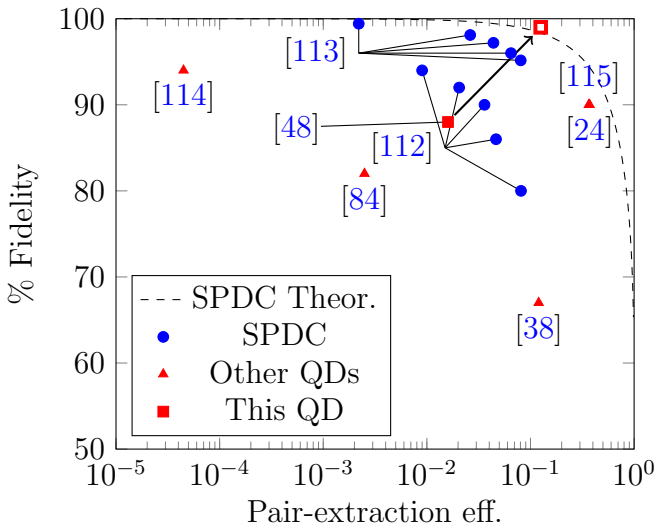

Figure 4.5: **Entanglement fidelity of quantum light sources.** Comparison of the performance of entangled photon sources consisting of quantum dots embedded in different nanostructures, red triangles, and actual performance of SPDC sources, blue circles. The dashed line indicates the theoretical upper limit for the performance of SPDC sources. The results obtained here and the analysis performed by Fognini et al. [48], suggest that the source under study, red square, is capable of surpassing the limit imposed on the SPDC sources, the hollow red square. This graph is adapted and modified from Ref.[84].

Fig.4.5 shows a comparison of the measured entanglement fidelity for different quantum light sources vs. their reported pair-extraction efficiency. Spontaneous parametric down-conversion (SPDC) sources has been the main sources of entangled photon pairs. However, such sources show a degradation of single-photon purity for high brightness, and thus, a reduction in entanglement fidelity. For QDs there is no theoretical limit on entanglement fidelity and extraction efficiency; however, engineering a photonic structure to have the QD

exhibit a high extraction efficiency, vanishing FSS, and near-unity entanglement fidelity is still a huge challenge. Based on the analysis performed by Fognini et al. [48], the sample under study is capable of generating entangled photon pairs with near-unity fidelity once the source is excited resonantly, resulting in $g^{(2)}(0) \ll 1$, and measured by single-photon detectors with a low timing jitter, e.g., super conducting nanowire single-photon detectors. The results obtained here suggests that this sample is capable of surpassing the limit imposed on SPDC sources; however, a measurement of entanglement fidelity of the source via resonant TPE and low-jitter detectors is yet to be performed.

Chapter 5

Universal finestructure eraser for quantum dots

We analyze the degree of entanglement measurable from a quantum dot via the biexciton-exciton cascade as a function of the exciton fine-structure splitting and the detection time resolution. We show that the time-energy uncertainty relation provides means to measure a high entanglement even in presence of a finite fine-structure splitting when a detection system with high temporal resolution is employed. Still, in many applications it would be beneficial if the finestructure splitting could be compensated to zero. To solve this problem, we propose an all optical approach with rotating waveplates to erase this fine-structure splitting completely and allows to obtain a high degree of entanglement with near-unity efficiency. Our optical approach is possible with current technology and is also compatible with any quantum dot showing finestructure splitting. This bears the advantage that for example the finestructure splitting of quantum dots in nanowires and micropillars can be directly compensated without the need for further sample processing.

5.1 Introduction

Semiconductor quantum dots (QDs) allow for the generation of polarization entangled photons [23, 66, 65] through the biexciton-exciton cascade [116]. Effects such as QD shape elongation [117, 71], piezoelectric fields [117], inhomogeneous alloy composition [73, 71], strain fields [118], or more generally all effects lowering the symmetry of the exciton's trapping potential [71] lead to a splitting of the exciton state. The spin-degeneracy of the bright exciton level is therefore normally split in QDs due to the spin-orbit interaction [119]. This splitting is called the fine-structure splitting (FSS) and its energy scale typically lies between $0 - 100\,\mu$eV in the case of III-V semiconductor quantum dots [73]. The FSS introduces a which-path information during the biexciton-exciton decay but only in the limit of slow photon detection. Yet, it was argued as being one of the main reasons for lowering the polarization entanglement [120, 35]. QD growth methods have been successfully developed to minimize the FSS [78, 121, 85], but reaching vanishing FSS remains a significant challenge. Consequently, several post-growth techniques have been developed to solve this problem by tuning the FSS to zero. Compensation has been achieved through external strain fields [118, 33], magnetic fields [35], electric fields [122, 123], annealing [124], or a combination of these approaches [77]. Typically, these techniques act macroscopically on the sample and only fully compensate *one* out of millions of QDs. Scaling up to many quantum dots on the same sample is a challenge. Furthermore, the well established strain compensation technique [118, 33] is difficult to adapt for QDs embedded in photonic nanostructures [85, 73, 29, 125, 126] due to strain relaxation over a length scale of $\approx 100\,$nm [125]. Quantum dots embedded in nanowires [85, 126, 125, 73] and micropillar cavities [25, 29]; however, possess several benefits such as enhanced photon extraction due to directional emission and near-unity single mode fiber coupling [30, 127]. Therefore, a universal FSS compensation technique easily applicable to QDs would be of great value.

In this chapter we introduce a novel FSS universal eraser technique which solves above problems and enhances the measurable entanglement towards unity by using frequency shifting capabilities of rotating $\lambda/2$-waveplates applied to both X and XX photons. Of particular significance, this frequency conversion process occurs without loss of photons due

to only unitary optical manipulations. FSS compensation techniques [128, 75, 129, 130, 131] have been proposed but our approach differs from Ref. [128] as it can be implemented with current technology, is not intrinsically slow ($\approx 10\,\mathrm{kHz}$) due to high voltage sweeps, and does not rely on the splitting of different polarization modes [75]. Furthermore, we are not suffering from photon loss and can compensate an arbitrarily small FSS in contrast to the scheme proposed in Ref. [129]. The reason is that we are not relying on stochastic sideband scattering [130] and don't need an additional filter system to select the right scattered lines preventing compensation in case the FSS is comparable with the QD linewidth. In addition, our approach differs from the phase compensation technique outlined in Ref. [131] as it allows to reach unity fidelity regardless of the FSS value, whereas with the phase compensation technique the fidelity can only be enhanced but cannot be brought to unity with a finite FSS.
We start our analysis by discussing the influence of the detection system's time resolution on the measurable entanglement.

5.2 The influence of time resolution on entanglement

The term detection system includes every component used to detect the arrival time of the two photons from the cascade, e.g., detector time jitter, the electronics to correlate the arrival times of the biexciton and exciton photons, and dispersion in optical components. We define the full width at half maximum of the correlation time distribution of such a system as the time resolution τ. For the sake of clarity we only consider FSS for reducing the measurable entanglement by phase averaging and do not consider dephasing mechanisms [132]. Fig. 5.1 (a) depicts the biexciton-exciton cascade without FSS. The cascade starts by the radiative decay of the biexciton (XX) state. Either a right- or left polarized *single* photon is emitted (R, L) [117]. After the emission of the XX photon the system is in the exciton state (X). This level is degenerate and $\uparrow\Downarrow$, $\downarrow\Uparrow$ are the state's eigenfunctions in spin space [117]. Here, $\uparrow,\downarrow$ and $\Uparrow,\Downarrow$ denote the electron and hole spins, respectively. Since we assumed zero FSS, it is impossible to know whether a spin up or down electron has recombined. This lack of knowledge entangles the photons to $\Phi = \frac{1}{\sqrt{2}}(RL + LR)$.

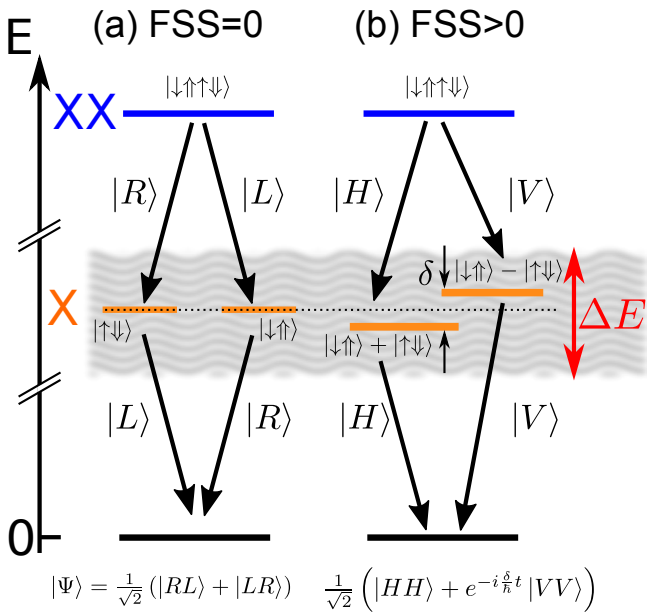

Figure 5.1: Representation of the biexciton (XX) exciton (X) emission. (a) In case of zero FSS the X-levels are degenerate and the two decay paths are indistinguishable which creates the entangled photon state $\frac{1}{\sqrt{2}}(RL + LR)$. (b) For non-zero FSS the X-level is split by δ and the quantum state will precess between these two states. However, with a fast measurement ($\Delta E \geq \delta$) the two X states (in H/V basis) cannot be resolved anymore and removes the which-path information. The uncertainty introduced through the measurement process is indicated by the wavy gray background.

In this situation, the detection system's time resolution does not affect the measurable entanglement of this state since it does not change over time. The situation is quite different in the case of finite FSS, as illustrated in Fig. 5.1 (b). Due to spin-orbit interaction the exciton states mix and the new eigenfunctions become $\frac{1}{\sqrt{2}}(\downarrow\Uparrow - \uparrow\Downarrow)$ and $\frac{1}{\sqrt{2}}(\downarrow\Uparrow + \uparrow\Downarrow)$ [133]. After the XX decay the X will precess between these two eigenfunctions until it also decays. This evolution makes the quantum state time dependent [69] and reads as

$$\Psi(t, \delta) = \frac{1}{\sqrt{2}}\left(HH + e^{-i\frac{\delta}{\hbar}t}VV\right), \tag{5.1}$$

where δ is the FSS energy, and H and V denote horizontally and vertically polarized single photon states. Equation 5.1 describes a fully entangled state even with finite FSS as shown by Stevenson et al. [69]. In fact, a slow detection system ($\tau \gg \hbar/\delta$) will average out the exponential phase term [69] in equation 5.1 and only classical correlations are detected [134]. In contrast, a fast detection system ($\tau \ll \hbar/\delta$) will render the two decay pathways indistinguishable since the energy uncertainty relation $\Delta E \geq \frac{\hbar}{2\tau}$ does not allow for a precise energy measurement anymore. This point of view is complementary to spectral filtering [135, 136] where only states with the same energy are analyzed but at the expense of filtering off many entangled photons. Please note that compared to employing spectral filtering a detection system with a high time resolution does not loose any photons, only each time bin will have a different phase (compare equation 5.1), as shown by several experiments [73, 69] resolving the so-called quantum oscillations. Nevertheless, a finite detector time resolution *always* introduces phase averaging and inevitably reduces the measurable entanglement.

In the following we will quantify this effect of reduced measured entanglement between the excitons in case of finite FSS with a photon detector of finite time resolution. In a quantum state tomography measurement [62] the state described in equation 5.1 is projected on the measurement basis ij, where $\mathrm{i,j} \in H, V, D, A, R, L$ with D, A denoting the diagonal and antidiagonal polarization states, respectively. We define the time evolution of the measured biexciton-exciton pair rate as $n(t, \tau_X) = \frac{N_0}{\tau_X} e^{-t/\tau_X}$ for $t \geq 0$ and $n(t, \tau_X) = 0$ otherwise. Here, t denotes the time after biexciton emission, τ_X the lifetime of the exciton level, and N_0 the number of detected photon pairs. In case of perfect time resolution we get a time dependent correlation rate in each projection i, j as

$$n_{i,j}(t, \delta, \tau_X) = |ij|\Psi(t, \delta)|^2 n(t, \tau_X). \tag{5.2}$$

The effect of finite time resolution of the detection system is modeled by $g(t, \tau)$, a Gaussian with full width at half maximum of τ. In such circumstances the detected projections are given by a convolution of the detection time resolution with equation 5.2 yielding

$$m_{i,j}(t, \delta, \tau, \tau_X) = n_{i,j}(t, \delta, \tau_X) * g(t, \tau). \tag{5.3}$$

The amount of entanglement which remains in $m_{i,j}(t, \delta, \tau, \tau_X)$ can be quantified by its concurrence $\mathcal{C}$ which lies between zero and one [60]. One in case the system is fully

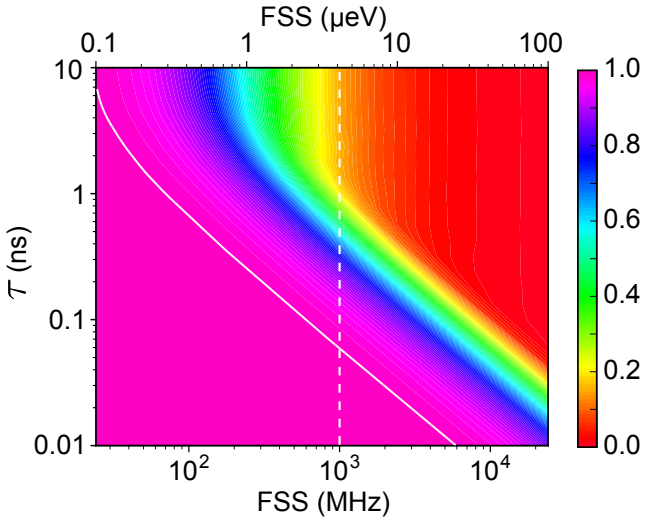

Figure 5.2: The measurable entanglement represented as the averaged concurrence $\bar{\mathcal{C}}$ as a function of the detector time resolution (τ) and fine-structure splitting (FSS) in case of an exciton lifetime of $\tau_X = 1\,\text{ns}$. The white dashed line is a guide to the eye for the examples in the text and the white solid line highlights the 0.99 contour line.

entangled and zero if there are only classical correlations present. Since the state with finite FSS is evolving in time we define the time averaged concurrence $\bar{\mathcal{C}}$ weighted with the amount of detected photons per infinitesimal time bin as

$$\bar{\mathcal{C}}(\delta, \tau, \tau_X) := \lim_{T\to\infty} \frac{1}{N_0} \int_{-T}^{T} n(t)\mathcal{C}\left(\rho\left(m_{i,j}\right)\right) dt, \tag{5.4}$$

where $\rho(m_{i,j})$ denotes the density matrix reconstructed from $m_{i,j}(t, \delta, \tau, \tau_X)$. Equation 5.4 is evaluated numerically[1] for an exciton lifetime of $\tau_X = 1\,\text{ns}$ and the result is presented in Fig. 5.2. The result indicates that with sufficiently fast detection, perfect entanglement can be reconstructed. With a state of the art detection system a time resolution of $\tau = 20\,\text{ps}$ is possible. A FSS of $\delta = 1\,\text{GHz}$ (white dashed line in Fig. 5.2), yields a measurement of $\bar{\mathcal{C}} = 0.999$ very close to unity. With regular avalanche photodiodes of $\tau = 300\,\text{ps}$ this value already reduces to $\bar{\mathcal{C}} = 0.77$. Worsening the detection system resolution further to a time

[1]Tomography library: https://github.com/afognini/Tomography

resolution of $\tau = 1\,\mathrm{ns}$ yields almost no entanglement. In this latter case, the concurrence significantly reduces to $\bar{\mathcal{C}} = 0.19$. However, the latter nanosecond time resolution would be preferred in applications regarding secure communication protocols where accurate timing on picoseconds over kilometers [6] becomes difficult. To solve this issue, we developed a fully optical compensation technique which reduces the FSS to zero. This allows the application of a photon detection system with less stringent time resolution requirements while maintaining near unity concurrence measurements.

5.3 Compensating the FSS

In the following we introduce a method to compensate the FSS, making it possible to employ detection systems with any timing resolution smaller than the QD's photon repetition period such that no overlap between adjacent pulses occur. The evolution of equation 5.1 with finite FSS is unitary due to the time evolving exponential phase factor. Thus, it must be possible [69] to undo this phase evolution by suitable unitary optical components. The main component to achieve complete removal is a rotating $\lambda/2$-waveplate. Such an optical component acts on circularly polarized light as a single sideband frequency shifter [137, 138]. A $\lambda/2$-waveplate spinning with angular frequency ω acting on a photon state can thus be described by the following operator

$$\Lambda_{1/2}(\omega) = \sum_k a^\dagger_{k+\frac{2\omega}{c},L} a_{k,R} + a^\dagger_{k-\frac{2\omega}{c},R} a_{k,L}, \tag{5.5}$$

where only k-vectors (k) perpendicular to the plane of the waveplate are considered. Here, c denotes the speed of light, and $a_{k,\lambda}$, $a^\dagger_{k,\lambda}$ denote anhilation and creation operators of photons with wavevector of length k and right or left circular polarization $\lambda \in \{R, L\}$, respectively. The action of a rotating $\lambda/2$-waveplate as described by equation 5.5 will up-convert R photons by the energy $2\hbar\omega$ and down-convert L photons by the same amount. Remarkably, this process can be achieved with unity efficiency. With the help of two

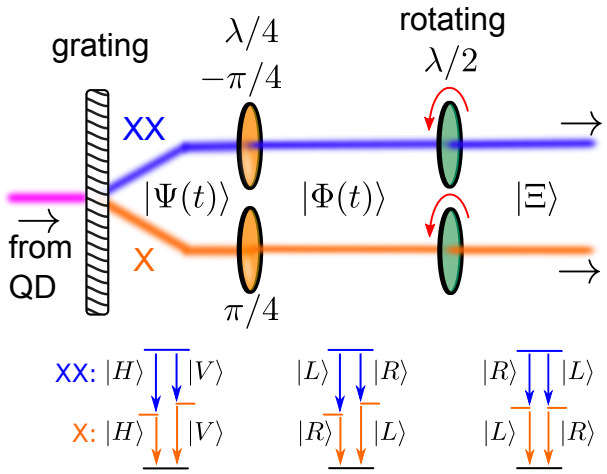

Figure 5.3: Proposed optical setup to compensate for a finite FSS. First, a polarization insensitive transmission grating splits the biexciton (XX) from the exciton (X) line. Next, a $\lambda/4$-plate transforms the X and XX photons into the circular basis. Finally, a $\lambda/2$-plate (one for each photon) rotating with an angular frequency of $f = \frac{\delta}{8\pi\hbar}$ compensates for the FSS. The polarization of the photons are indicated underneath the optical path after each waveplate. The length of the arrows is indicative for the photon energy. For convenience possible mirrors have been omitted.

$\lambda/4$-waveplates the XX and the X state transform into

$$\begin{aligned}\Phi(t,\delta) &= \Lambda_{1/4}(-\pi/4) \otimes \Lambda_{1/4}(\pi/4)\Psi(t,\delta) \\ &= \frac{1}{\sqrt{2}}\left(LR + e^{-i\frac{\delta}{\hbar}t}RL\right),\end{aligned} \tag{5.6}$$

where the angles $\pm\pi/4$ are oriented with respect to the horizontal orientation.

Now, sending this new state $\Phi(t,\delta)$ through a spinning $\lambda/2$-waveplate rotating with angular frequency of $\omega = \frac{\delta}{4\hbar}$ yields an entangled Bell state

$$\begin{aligned}\Xi &= \Lambda_{1/2}\left(\frac{\delta}{4\hbar}\right) \otimes \Lambda_{1/2}\left(\frac{\delta}{4\hbar}\right)\Phi(t,\delta) \\ &= \frac{1}{\sqrt{2}}\left(RL + LR\right),\end{aligned} \tag{5.7}$$

where the time dependent phase factor has been completely removed. Here, $\Lambda_{1/2}(\omega)$ represents the operator from equation 5.5. For a detailed derivation of equation 5.7 see the Appendix. A possible setup to erase the FSS is depicted in Fig. 5.3. First, a dispersive element, such as a high efficiency transmission grating, splits the XX line from the X line. Next, the XX (X) photon is sent through a fixed $\lambda/4$ waveplate offset from the horizontal direction by $-\pi/4$ ($\pi/4$). The photon state at this stage is represented by equation 5.6. Finally, letting them both pass through a rotating $\lambda/2$-waveplate with angular frequency $\omega = \frac{\delta}{4\hbar}$ removes the FSS completely. A rotating $\lambda/2$-waveplate can be implemented with electro-optical modulators (EOM) [139, 140]. In this case, the conversion efficiency is only limited by the transmission through the EOM. In fact, owing to the high transparency of EOMs a 95 % conversion efficiency was achieved [141].

Note, in contrast to a rotating $\lambda/2$-waveplate the EOM approach needs twice the angular frequency to obtain the same frequency shift [139]. For example, the RF frequency ($f = \frac{\omega}{\pi} = \frac{\delta}{4\pi\hbar}$) necessary to compensate a FSS of 10 μeV with the EOM approach is 1209 MHz, which is easily achievable with current EOM technology [139] reaching tens of GHz modulation bandwidth.

As the proposed technique is not invasive on the sample containing the QDs it is possible to compensate for the FSS of every QD as long as the EOM's frequency can be tuned to

compensate the FSS of the QD under study. This feature renders our approach universally applicable as simply a different RF frequency needs to be applied to compensate the FSS of a different QD.

5.4 Conclusions

In summary, we have analyzed the effect of finite FSS and the influence of the detection time resolution on the measurable entanglement from a single QD via the biexciton-exciton cascade. The uncertainty in energy and time in the measurement allows the emitted QD photons to be entangled when a detection system with sufficient timing resolution is employed. However, the precise timing requirement on a picosecond level is hampering the progress in making the entanglement useful for applications and research. We have proposed a universal optical setup to completely remove the FSS based on a rotating $\lambda/2$-plate, which can be implemented with current EOM technology. The proposed technique will allow to make the entanglement created from QDs available for many applications like quantum communication, sensing, and imaging.

Chapter 6

Conclusions and outlook

6.1 Summary

The work presented in this thesis reveals the potential quality of a InAs/InP QDs embedded inside a wurtzite InP photonic nanowire, for quantum information and quantum computing purposes. High brightness of the source, due to a tapered nanowire which acts a waveguide for the emitted light from the QD, allows for performing a complete two-photon tomography of the source and recording a detailed evolution of its state. Furthermore, the performance of the source was enhanced upon a resonant two-photon excitation. The results obtained can be listed as:

- Charge noise surrounding the QD can alter the biexciton and exciton state by introducin dephasing via spin-spin interactions and generating fluctuating electromagnetic fields. However, it was observed that proper excitation scheme, quasi-resonant vs. off-resonant, can reduce the charge noise to a level where dephasing becomes negligible and the source acts as a dephasing-free entangled-photon source. A fact which was inferred by comparing the measurement with a theoretical model which does not include any dephasing terms.

- Exciton state's fine-structure splitting does not lead to degredation of the entanglement fidelity of the source, as it is a unitary process and only causes the precession of the state. However, a detector with low timing resolution can lead to introduction of a which-path information between the two eigen-states of exciton, leading to a low measured entanglement fidelity value. Using a fast detector will erase the which-path information and the entanglement will be retrieved.

- Exciting the QD via resonant TPE scheme, results in a substantial suppression of multi-photon emission, which in turn leads to an enhancement of the measured entanglement fidelity. Moreover, the pair-production efficiency of the source will be improved to a degree, that performing two-photon tomography under resonant TPE and by using a fast detector with low dark-counts, can yield results surpassing the performance of SPDC sources.

- An all-optical approach is possible in order to achieve a universal method for removing the FSS of the exciton state, after the photons are emitted from the source. This approach is feasible, as it does not require manipulation of the source and can be performed using the available technology.

6.2 Future outlook

The research presented in this thesis, opens room for further investigations on QDs in photonic nanowires. The first obvious research to be performed is conducting two-photon state tomography, once the source is excited via resonant TPE and detected exhibiting low timing jitter and low dark count rates, e.g., superconducting nanowire detectors [28], in order to test the prediction that QDs in nanowires are capable of generating photon-pairs exhibiting near-unity entanglement fidelity under such conditions. In order to enhance the efficiency of the setup, notch filters and tunable band-pass filters can be used in order to bypass the spectrometers, which exhibit low transmission efficiencies, $\epsilon < 10\%$. A proposed setup for performing the two-photon state tomography is presented in Fig. 6.1.

The emitted photons pass through a set of notch filters, which will block the reflected laser pulse, and then will pass through the state tomography optics, quarter-wave plates, half-wave plates, and polarizers. These optics are put along the transmission path of the non-polarizing beam-splitter, since, on the reflection path photons will gain an arbitary phase and the projection measurement will no longer be accurate. Lastly, since the tunable band-pass filters available to the lab are fiber coupled, the photons are coupled to single-mode fibers. At the last stage, fiber-coupled detectors collected the projected photons and are in turn correlated to build statistics on the correlation of different two-photon basis.

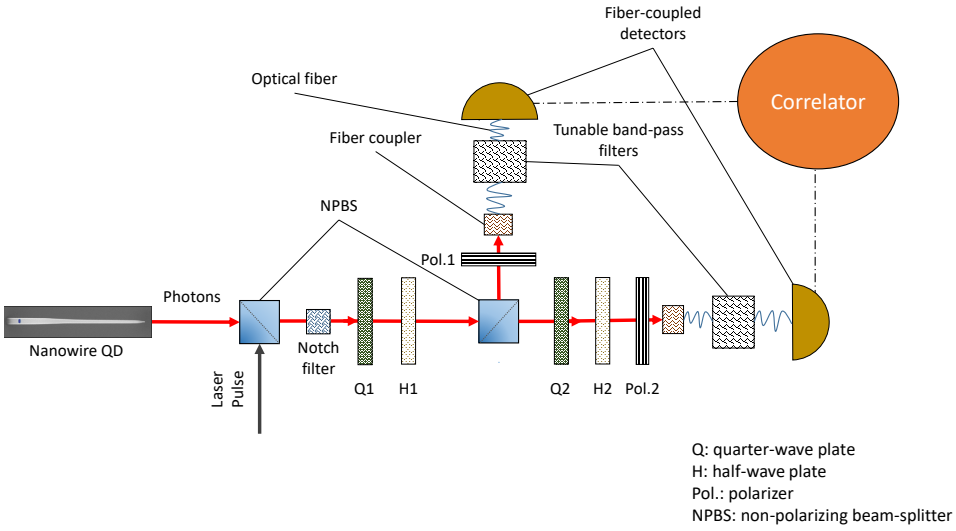

Figure 6.1: **Schematic setup for two-photon state tomography under resonant TPE.** The notch filter helps with suppression of the reflected laser light. The wave plates are all put along the transmission of the second NPBS, since the photons gain some phase upon reflection and the projection will no longer be accurate. Based on the tunable band-pass filters available, the photons have to be first coupled to a single-mode fiber and then passed through the band-pass filters, and then fed to fiber-coupled detectors.

Another experiment to be run as an extension to the results presented in this thesis, is implementing the all-optical approach for removing the FSS of exciton state. An electro-

optic modulator base on lithium niobate [142] can act as a fast rotating half-wave plate by applying an oscillating electric field through its electrodes. Such a device, similar to the device used by Qin et al., [139], is now available in our lab. Three electrodes adjacent to the zinc oxide difused waveguide control the refractive index of the crystal in two dimensions as explained by Simon Daley [143]. As proposed by fognini et al., [52], in order to perform the experiment, the exciton and biexciton photons have to be separated, passed through a quarter-wave plate, and then enter the fast-rotating half-wave plate. Success of the protocol can be tested by monitoring the frequency of oscillations observed in Fig. 3.2, for which projection measurements in $|R\rangle$ / $|L\rangle$ basis is required.

Besides the immediate experiments along the lines of this thesis, QDs in nanowires open different possibilities for quantum communication. One line of research can be dedicated to combining QDs in nanowires with quantum memories in order to build quantum repeaters [144]. Recently conversion of a near infrared photon to telecom-wavelength, as well as, storage of the photon in a quantum memory with high fidelity and lifetime as been achieved [145]; also, resonant TPE of QDs in nanowires can provide us with photon-pairs exhibiting high single-photon purity and entanglement fidelity. A long term project can be entanglement swapping between two separate sources [146]. Two single photons, each part of an entangled photon pair emitted from two different sources, can be stored in a quantum memory in order to achieve perfect timing, then retrieved and interfered in a Bell measurement, in order to entangled the two other photons which have not interacted. For this purpose, some initial steps has to be taken. First, the two sources have to be manipulated in order to emit photon-pairs at exactly similar wavelengths. Trotta et al., [33], have proposed a method in order to achieve entangled photon-pairs with on-demand wavelength for self-assembled quantum dots; however, such a scheme has not yet been provided for QDs in nanowires. Besides, experiments for measuring indistinguishability of the successive photons from one source, as well as, photons from separate sources have to be performed under resonant TPE. A previous study [83] on indistinguishability of such a source, relied on off-resonant excitation and low laser repetition rate, $f = 20$MHz, which intensifies photon emission jitter and the detrimental effects of the charge noise around the QD, as well as, the environment in which each photon has to be delayed. Under such

circumstances, visibilities above 80% has been reported, by inclusion of $< 4\%$ of the total counts; however, these results does not reveal the ultimate value achievable with QDs in nanowires. Using resonant TPE and a pump laser with a repetition rate of 76MHz, can enhance the results significantly.

References

[1] Brahim Lounis and Michel Orrit. Single-photon sources. *Reports Prog. Phys.*, 68:1129–1179, 2005.

[2] Morgan M Weston, Michael JW Hall, Matthew S Palsson, Howard M Wiseman, and Geoff J Pryde. Experimental test of universal complementarity relations. *Physical review letters*, 110(22):220402, 2013.

[3] Sacha Kocsis, Boris Braverman, Sylvain Ravets, Martin J Stevens, Richard P Mirin, L Krister Shalm, and Aephraim M Steinberg. Observing the average trajectories of single photons in a two-slit interferometer. *Science*, 332(6034):1170–1173, 2011.

[4] Vincent Jacques, E Wu, Frédéric Grosshans, François Treussart, Philippe Grangier, Alain Aspect, and Jean-François Roch. Experimental realization of wheeler's delayed-choice gedanken experiment. *Science*, 315(5814):966–968, 2007.

[5] Lynden K Shalm, Evan Meyer-Scott, Bradley G Christensen, Peter Bierhorst, Michael A Wayne, Martin J Stevens, Thomas Gerrits, Scott Glancy, Deny R Hamel, Michael S Allman, et al. Strong loophole-free test of local realism. *Physical review letters*, 115(25):250402, 2015.

[6] Rupert Ursin, F Tiefenbacher, T Schmitt-Manderbach, H Weier, Thomas Scheidl, M Lindenthal, B Blauensteiner, T Jennewein, J Perdigues, P Trojek, et al. Entanglement-based quantum communication over 144 km. *Nature physics*, 3(7):481, 2007.

[7] Dik Bouwmeester, Jian-Wei Pan, Klaus Mattle, Manfred Eibl, Harald Weinfurter, and Anton Zeilinger. Experimental quantum teleportation. *Nature*, 390(6660):575, 1997.

[8] Edo Waks, Kyo Inoue, Charles Santori, David Fattal, Jelena Vuckovic, Glenn S Solomon, and Yoshihisa Yamamoto. Secure communication: Quantum cryptography with a photon turnstile. *Nature*, 420(6917):762, 2002.

[9] Alexios Beveratos, Rosa Brouri, Thierry Gacoin, André Villing, Jean-Philippe Poizat, and Philippe Grangier. Single photon quantum cryptography. *Physical review letters*, 89(18):187901, 2002.

[10] Xiaogang Qiang, Xiaoqi Zhou, Jianwei Wang, Callum M Wilkes, Thomas Loke, Sean O'Gara, Laurent Kling, Graham D Marshall, Raffaele Santagati, Timothy C Ralph, et al. Large-scale silicon quantum photonics implementing arbitrary two-qubit processing. *Nature photonics*, 12(9):534, 2018.

[11] Jeremy L O'Brien, Geoffrey J Pryde, Andrew G White, Timothy C Ralph, and David Branning. Demonstration of an all-optical quantum controlled-not gate. *Nature*, 426(6964):264, 2003.

[12] Mario Krenn, Mehul Malik, Thomas Scheidl, Rupert Ursin, and Anton Zeilinger. Quantum communication with photons. *Optics in Our Time*, 18:455, 2016.

[13] John F. Clauser. Experimental distinction between the quantum and classical field-theoretic predictions for the photoelectric effect. *Phys. Rev. D*, 9:853–860, Feb 1974.

[14] John F Clauser and Abner Shimony. Bell's theorem. experimental tests and implications. *Reports on Progress in Physics*, 41(12):1881, 1978.

[15] Alain Aspect, Philippe Grangier, and Gérard Roger. Experimental tests of realistic local theories via bell's theorem. *Physical review letters*, 47(7):460, 1981.

[16] Igor Aharonovich, Dirk Englund, and Milos Toth. Solid-state single-photon emitters. *Nat. Photonics*, 10(10):631–641, 2016.

[17] David C Burnham and Donald L Weinberg. Observation of simultaneity in parametric production of optical photon pairs. *Physical Review Letters*, 25(2):84, 1970.

[18] CK Hong and Leonard Mandel. Experimental realization of a localized one-photon state. *Physical Review Letters*, 56(1):58, 1986.

[19] YH Shih, AV Sergienko, Morton H Rubin, TE Kiess, and CO Alley. Two-photon entanglement in type-ii parametric down-conversion. *Physical Review A*, 50(1):23, 1994.

[20] DF Walls and GJ Milburn. *Quantum Optics*. Berlin: Springer, 1994.

[21] Xi-Lin Wang, Luo-Kan Chen, Wei Li, H-L Huang, Chang Liu, Chao Chen, Y-H Luo, Z-E Su, Dian Wu, Z-D Li, et al. Experimental ten-photon entanglement. *Physical review letters*, 117(21):210502, 2016.

[22] PM Petroff and SP DenBaars. Mbe and mocvd growth and properties of self-assembling quantum dot arrays in iii-v semiconductor structures. *Superlattices and microstructures*, 15(1):15, 1994.

[23] Oliver Benson, Charles Santori, Matthew Pelton, and Yoshihisa Yamamoto. Regulated and Entangled Photons from a Single Quantum Dot. *Phys. Rev. Lett.*, 84(11):2513–2516, 2000.

[24] Yan Chen, Michael Zopf, Robert Keil, Fei Ding, and Oliver G. Schmidt. Highly-efficient extraction of entangled photons from quantum dots using a broadband optical antenna. *Nat. Commun.*, 9(1):1–7, 2018.

[25] O Gazzano, S Michaelis De Vasconcellos, C Arnold, A Nowak, E Galopin, I Sagnes, L Lanco, A Lemaître, and P Senellart. Bright solid-state sources of indistinguishable single photons. *Nature communications*, 4:1425, 2013.

[26] Julien Claudon, Joël Bleuse, Nitin Singh Malik, Maela Bazin, Périne Jaffrennou, Niels Gregersen, Christophe Sauvan, Philippe Lalanne, and Jean-Michel Gérard. A

highly efficient single-photon source based on a quantum dot in a photonic nanowire. *Nature Photonics*, 4(3):174, 2010.

[27] M. Müller, S. Bounouar, K. D. Jöns, M. Glässl, and P. Michler. On-demand generation of indistinguishable polarization-entangled photon pairs. *Nature Photonics*, 8(3):224–228, 2014.

[28] Lucas Schweickert, Klaus D. Jöns, Katharina D. Zeuner, Saimon Filipe Covre Da Silva, Huiying Huang, Thomas Lettner, Marcus Reindl, Julien Zichi, Rinaldo Trotta, Armando Rastelli, and Val Zwiller. On-demand generation of background-free single photons from a solid-state source. *Appl. Phys. Lett.*, 112(9):0–4, 2018.

[29] N. Somaschi, V. Giesz, L. De Santis, J. C. Loredo, M. P. Almeida, G. Hornecker, S. L. Portalupi, T. Grange, C. Antón, J. Demory, C. Gómez, I. Sagnes, N. D. Lanzillotti-Kimura, A. Lemaítre, A. Auffeves, A. G. White, L. Lanco, and P. Senellart. Near-optimal single-photon sources in the solid state. *Nat. Photonics*, 10(5):340–345, 2016.

[30] Gabriele Bulgarini, Michael E Reimer, Maaike Bouwes Bavinck, Klaus D Jons, Dan Dalacu, Philip J Poole, Erik PAM Bakkers, and Val Zwiller. Nanowire waveguides launching single photons in a gaussian mode for ideal fiber coupling. *Nano letters*, 14(7):4102–4106, 2014.

[31] Ali W Elshaari, Iman Esmaeil Zadeh, Andreas Fognini, Michael E Reimer, Dan Dalacu, Philip J Poole, Val Zwiller, and Klaus D Jöns. On-chip single photon filtering and multiplexing in hybrid quantum photonic circuits. *Nature communications*, 8(1):379, 2017.

[32] Santosh Kumar, Rinaldo Trotta, Eugenio Zallo, JD Plumhof, P Atkinson, Armando Rastelli, and Oliver G Schmidt. Strain-induced tuning of the emission wavelength of high quality gaas/algaas quantum dots in the spectral range of the 87rb d2 lines. *Applied Physics Letters*, 99(16):161118, 2011.

[33] Rinaldo Trotta, Javier Martín-Sánchez, Istvan Daruka, Carmine Ortix, and Armando Rastelli. Energy-tunable sources of entangled photons: A viable concept for solid-state-based quantum relays. *Phys. Rev. Lett.*, 114(15):1–5, 2015.

[34] Yan Chen, Jiaxiang Zhang, Michael Zopf, Kyubong Jung, Yang Zhang, Robert Keil, Fei Ding, and Oliver G. Schmidt. Wavelength-tunable entangled photons from silicon-integrated III-V quantum dots. *Nat. Commun.*, 7:1–7, 2016.

[35] R. M. Stevenson, R. J. Young, P. Atkinson, K. Cooper, D. A. Ritchie, and A. J. Shields. A semiconductor source of triggered entangled photon pairs. *Nature*, 439(7073):179–182, 2006.

[36] Robert J Young, R Mark Stevenson, Paola Atkinson, Ken Cooper, David A Ritchie, and Andrew J Shields. Improved fidelity of triggered entangled photons from single quantum dots. *New Journal of Physics*, 8(2):29, 2006.

[37] Daniel Huber, Marcus Reindl, Saimon Filipe, Christian Schimpf, Javier Martín-sánchez, Huiying Huang, Giovanni Piredda, Johannes Edlinger, Armando Rastelli, and Rinaldo Trotta. Strain-Tunable GaAs Quantum Dot : A Nearly Dephasing-Free Source of Entangled Photon Pairs on Demand. *Phys. Rev. Lett.*, 121(3):33902, 2018.

[38] Adrien Dousse, Jan Suffczynski, Alexios Beveratos, Olivier Krebs, Aristide Lemaître, Isabelle Sagnes, Jacqueline Bloch, Paul Voisin, and Pascale Senellart. Ultrabright source of entangled photon pairs. *Nature*, 466:217, Jul 2010.

[39] Hui Wang, Hai Hu, T-H Chung, Jian Qin, Xiaoxia Yang, J-P Li, R-Z Liu, H-S Zhong, Y-M He, Xing Ding, et al. On-demand semiconductor source of entangled photons which simultaneously has high fidelity, efficiency, and indistinguishability. *Physical Review Letters*, 122(11):113602, 2019.

[40] Michael E Reimer, Gabriele Bulgarini, Nika Akopian, Moïra Hocevar, Maaike Bouwes Bavinck, Marcel A Verheijen, Erik P A M Bakkers, Leo P Kouwenhoven, and Val Zwiller. Bright single-photon sources in bottom-up tailored nanowires. *Nat. Commun.*, 3:737, 2012.

[41] Vladimir Roger Miranda La Hera. *Optical Properties of Wurtzite Phase InAsP/InP Heterostructure Nanowires*. Master's thesis, Universidade Estadual de Campinas, 2015.

[42] Maarten van Weert. *Quantum Dots in Vertical Nanowire Devices*. PhD dissertation, Delft University of Technology, 2010.

[43] M. Zeeshan, N. Sherlekar, A. Ahmadi, R.L. Williams, and M.E. Reimer. Proposed Scheme to Generate Bright Entangled Photon Pairs by Application of a Quadrupole Field to a Single Quantum Dot. *Phys. Rev. Lett.*, 122(22):227401, 2019.

[44] Oliver Gywat, Hubert J. Krenner, and Jesse Brezovsky. *Spins in Optically Active Quantum Dots. Concepts and Methods*. WILEY-VCH, KGaA, Weinheim, 2010.

[45] Ming Gong, Kaimin Duan, Chuan-Feng Li, Rita Magri, Gustavo A Narvaez, and Lixin He. Electronic structure of self-assembled in as/ in p quantum dots: Comparison with self-assembled in as/ ga as quantum dots. *Physical Review B*, 77(4):045326, 2008.

[46] E. G. Gadret, G. O. Dias, L. C. O. Dacal, M. M. de Lima, C. V. R. S. Ruffo, F. Iikawa, M. J. S. P. Brasil, T. Chiaramonte, M. A. Cotta, L. H. G. Tizei, D. Ugarte, and A. Cantarero. Valence-band splitting energies in wurtzite inp nanowires: Photoluminescence spectroscopy and ab initio calculations. *Phys. Rev. B*, 82:125327, Sep 2010.

[47] Brian D Gerardot, Daniel Brunner, Paul A Dalgarno, Patrik Öhberg, Stefan Seidl, Martin Kroner, Khaled Karrai, Nick G Stoltz, Pierre M Petroff, and Richard J Warburton. Optical pumping of a single hole spin in a quantum dot. *Nature*, 451(7177):441, 2008.

[48] A. Fognini, A. Ahmadi, M. Zeeshan, J. T. Fokkens, S. J. Gibson, N. Sherlekar, S. J. Daley, D. Dalacu, P. J. Poole, K. D. Jöns, V. Zwiller, and M. E. Reimer. Dephasing free photon entanglement with a quantum dot. *ACS Photonics*, 6(7):1656–1663, 2019.

[49] H. Y. Ramirez, C. H. Lin, C. C. Chao, Y. Hsu, W. T. You, S. Y. Huang, Y. T. Chen, H. C. Tseng, W. H. Chang, S. D. Lin, and S. J. Cheng. Optical fine structures of highly quantized ingaas/gaas self-assembled quantum dots. *Phys. Rev. B*, 81:245324, Jun 2010.

[50] A. J. Bennett, M. A. Pooley, R. M. Stevenson, M. B. Ward, R. B. Patel, A. Boyer De La Giroday, N. Sköd, I. Farrer, C. A. Nicoll, D. A. Ritchie, and A. J. Shields. Electric-field-induced coherent coupling of the exciton states in a single quantum dot. *Nat. Phys.*, 6(12):947–950, 2010.

[51] Ranber Singh. Tuning fine structure splitting and exciton emission energy in semiconductor quantum dots. *J. Lumin.*, 202(February):118–131, 2018.

[52] A. Fognini, A. Ahmadi, S. J. Daley, M. E. Reimer, and V. Zwiller. Universal finestructure eraser for quantum dots. *Opt. Express*, 26(19):25–28, 2017.

[53] M Bayer, G Ortner, O Stern, A Kuther, A A Gorbunov, A Forchel, P Hawrylak, S Fafard, K Hinzer, T L Reinecke, S N Walck, J P Reithmaier, F Klopf, and F. Schäfer. Fine structure of neutral and charged excitons in self-assembled In(Ga)As/(Al)GaAs quantum dots. *Phys. Rev. B*, 65(19):195315, 2002.

[54] H. W. Van Kesteren, E. C. Cosman, W. A.J.A. Van Der Poel, and C. T. Foxon. Fine structure of excitons in type-II GaAs/AlAs quantum wells. *Phys. Rev. B*, 41(8):5283–5292, 1990.

[55] A. Franceschetti, L. W. Wang, H. Fu, and A. Zunger. Short-range versus long-range electron-hole exchange interactions in semiconductor quantum dots. *Phys. Rev. B*, 58:R13367–R13370, Nov 1998.

[56] Christopher Gerry, Peter Knight, and Peter L Knight. *Introductory quantum optics*. Cambridge university press, 2005.

[57] R Hanbury Brown, Richard Q Twiss, et al. Correlation between photons in two coherent beams of light. *Nature*, 177(4497):27–29, 1956.

[58] Charles H. Bennett, David P. DiVincenzo, David P. DiVincenzo, John a. Smolin, John a. Smolin, William K. Wootters, and William K. Wootters. Mixed-state entanglement and quantum error correction. *Phys. Rev. A (Atomic, Mol. Opt. Physics)*, 54(5):3824, 1996.

[59] Scott Hill and William K Wootters. Entanglement of a Pair of Quantum Bits. *Phys. Rev. Lett.*, 78(26), 1997.

[60] William K. Wootters. Entanglement of formation of an arbitrary state of two qubits. *PRL*, 14(3):199–212, 1998.

[61] F Verstraete and H Verschelde. Fidelity of mixed states of two qubits. *Phys. Rev. A*, 66(2):22307, 2002.

[62] Daniel F. V. James, Paul G. Kwiat, William J. Munro, and Andrew G. White. Measurement of qubits. *Phys. Rev. A*, 64:052312, 2001.

[63] Piotr Badziąg, Michał Horodecki, Paweł Horodecki, and Ryszard Horodecki. Local environment can enhance fidelity of quantum teleportation. *Phys. Rev. A*, 62:012311, Jun 2000.

[64] George Gabriel Stokes. On the composition and resolution of streams of polarized light from different sources. *Transactions of the Cambridge Philosophical Society*, 9:399, 1851.

[65] R. Hafenbrak, S. M. Ulrich, P Michler, L. Wang, A. Rastelli, and O. G. Schmidt. Triggered polarization-entangled photon pairs from a single quantum dot up to 30 K. *New J. Phys*, 9(315):315, 2007.

[66] C. L. Salter, R. M. Stevenson, I. Farrer, C. A. Nicoll, D. A. Ritchie, and A. J. Shields. An entangled-light-emitting diode. *Nature*, 465(7298):594–597, 2010.

[67] Daniel Huber, Marcus Reindl, Yongheng Huo, Huiying Huang, Johannes S. Wildmann, Oliver G. Schmidt, Armando Rastelli, and Rinaldo Trotta. Highly indistin-

guishable and strongly entangled photons from symmetric GaAs quantum dots. *Nat. Commun.*, 8:15506, May 2017.

[68] Robert Keil, Michael Zopf, Yan Chen, Bianca Höfer, Jiaxiang Zhang, Fei Ding, and Oliver G. Schmidt. Solid-state ensemble of highly entangled photon sources at rubidium atomic transitions. *Nat. Commun.*, 8:15501, 2017.

[69] R. Mark Stevenson, Andrew J. Hudson, Anthony J. Bennett, Robert J. Young, Christine A. Nicoll, David A. Ritchie, and Andrew J. Shields. Evolution of entanglement between distinguishable light states. *Phys. Rev. Lett.*, 101:170501, Oct 2008.

[70] Wayne M. Witzel, Malcolm S. Carroll, Andrea Morello, Łukasz Cywiński, and S. Das Sarma. Electron spin decoherence in isotope-enriched silicon. *Phys. Rev. Lett.*, 105:187602, Oct 2010.

[71] Ranber Singh and Gabriel Bester. Nanowire quantum dots as an ideal source of entangled photon pairs. *Phys. Rev. Lett.*, 103:063601, Aug 2009.

[72] M.B. Ward, M.C. Dean, R.M. Stevenson, A.J. Bennett, D.J.P. Ellis, K. Cooper, I. Farrer, C.A. Nicoll, D.A. Ritchie, and A.J. Shields. Coherent dynamics of a telecom-wavelength entangled photon source. *Nat. Commun.*, 5:3316, February 2014.

[73] Tobias Huber, Ana Predojević, Milad Khoshnegar, Dan Dalacu, Philip J. Poole, Hamed Majedi, and Gregor Weihs. Polarization entangled photons from quantum dots embedded in nanowires. *Nano Lett.*, 14(12):7107–7114, 2014.

[74] Jianping Wang, Ming Gong, Guang-Can Guo, and Lixin He. Eliminating the fine structure splitting of excitons in self-assembled inas/gaas quantum dots via combined stresses. *Appl. Phys. Lett.*, 101(6):063114, 2012.

[75] Nick S. Jones and T. M. Stace. Photon frequency-mode matching using acousto-optic frequency beam splitters. *Phys. Rev. A*, 73:033813, Mar 2006.

[76] Rinaldo Trotta, Javier Martín-Sánchez, Johannes S. Wildmann, Giovanni Piredda, Marcus Reindl, Christian Schimpf, Eugenio Zallo, Sandra Stroj, Johannes Edlinger,

and Armando Rastelli. Wavelength-tunable sources of entangled photons interfaced with atomic vapours. *Nat. Commun.*, 7:1–7, 2016.

[77] R Trotta, E Zallo, C Ortix, Paola Atkinson, JD Plumhof, J Van den Brink, A Rastelli, and OG Schmidt. Universal recovery of the energy-level degeneracy of bright excitons in ingaas quantum dots without a structure symmetry. *Physical review letters*, 109(14):147401, 2012.

[78] Takashi Kuroda, Takaaki Mano, Neul Ha, Hideaki Nakajima, Hidekazu Kumano, Bernhard Urbaszek, Masafumi Jo, Marco Abbarchi, Yoshiki Sakuma, Kazuaki Sakoda, Ikuo Suemune, Xavier Marie, and Thierry Amand. Symmetric quantum dots as efficient sources of highly entangled photons: Violation of bell's inequality without spectral and temporal filtering. *Phys. Rev. B*, 88:041306, Jul 2013.

[79] Bernhard Urbaszek, Xavier Marie, Thierry Amand, Olivier Krebs, Paul Voisin, Patrick Maletinsky, Alexander Högele, and Atac Imamoglu. Nuclear spin physics in quantum dots: An optical investigation. *Rev. Mod. Phys.*, 85:79–133, Jan 2013.

[80] M. Sénés, B. L. Liu, X. Marie, T. Amand, and J. M. Gérard. *Spin Dynamics of Neutral and Charged Excitons in InAs/GaAs Quantum Dots*, pages 79–88. Springer Netherlands, Dordrecht, 2003.

[81] Andreas V. Kuhlmann, Julien Houel, Arne Ludwig, Lukas Greuter, Dirk Reuter, Andreas D. Wieck, Martino Poggio, and Richard J. Warburton. Charge noise and spin noise in a semiconductor quantum device. *Nat. Phys.*, 9(9):570–575, September 2013.

[82] Dan Dalacu, Khaled Mnaymneh, Jean Lapointe, Xiaohua Wu, Philip J. Poole, Gabriele Bulgarini, Val Zwiller, and Michael E. Reimer. Ultraclean emission from InAsP quantum dots in defect-free wurtzite InP nanowires. *Nano Lett.*, 12(11):5919–5923, 2012.

[83] M. E. Reimer, G. Bulgarini, A. Fognini, R. W. Heeres, B. J. Witek, M. A.M. Versteegh, A. Rubino, T. Braun, M. Kamp, S. Höfling, D. Dalacu, J. Lapointe, P. J.

Poole, and V. Zwiller. Overcoming power broadening of the quantum dot emission in a pure wurtzite nanowire. *Phys. Rev. B*, 93(19):1–9, 2016.

[84] Klaus D. Jöns, Lucas Schweickert, Marijn A. M. Versteegh, Dan Dalacu, Philip J. Poole, Angelo Gulinatti, Andrea Giudice, Val Zwiller, and Michael E. Reimer. Bright nanoscale source of deterministic entangled photon pairs violating bell's inequality. *Scientific Reports*, 7(1):1700, 2017.

[85] Marijn A. M. Versteegh, Michael E. Reimer, Klaus D. Jöns, Dan Dalacu, Philip J. Poole, Angelo Gulinatti, Andrea Giudice, and Val Zwiller. Observation of strongly entangled photon pairs from a nanowire quantum dot. *Nat. Commun.*, 5:5298, October 2014.

[86] Mark D. de Burgh, Nathan K. Langford, Andrew C. Doherty, and Alexei Gilchrist. Choice of measurement sets in qubit tomography. *Phys. Rev. A*, 78:052122, Nov 2008.

[87] T. Fokkens, A. Fognini, and V. Zwiller, 2016-2017. Tomography Library, available at GitHub.

[88] Kevin A Fischer, Lukas Hanschke, Jakob Wierzbowski, Tobias Simmet, Constantin Dory, Jonathan J Finley, Jelena Vučković, and Kai Müller. Signatures of two-photon pulses from a quantum two-level system. *Nature Physics*, 13(7):649, 2017.

[89] Yu Jia Wei, Yu Ming He, Ming Cheng Chen, Yi Nan Hu, Y. He, Dian Wu, Christian Schneider, Martin Kamp, Sven Höfling, Chao Yang Lu, and Jian Wei Pan. Deterministic and robust generation of single photons from a single quantum dot with 99.5% indistinguishability using adiabatic rapid passage. *Nano Lett.*, 14(11):6515–6519, 2014.

[90] Lukas Hanschke, Kevin A Fischer, Stefan Appel, Daniil Lukin, Jakob Wierzbowski, Shuo Sun, Rahul Trivedi, Jelena Vu, Jonathan J Finley, and Kai Müller. Quantum dot single-photon sources with ultra-low multi- photon probability. (August), 2018.

[91] Thomas Belhadj, Takashi Kuroda, Claire-Marie Simon, Thierry Amand, Takaaki Mano, Kazuaki Sakoda, Nobuyuki Koguchi, Xavier Marie, and Bernhard Urbaszek. Optically monitored nuclear spin dynamics in individual GaAs quantum dots grown by droplet epitaxy. *Phys. Rev. B*, 78:205325, Nov 2008.

[92] Pascale Senellart, Glenn Solomon, and Andrew White. High-performance semiconductor quantum-dot single-photon sources. *Nat. Nanotechnol.*, 12(11):1026–1039, 2017.

[93] B. D. Gerardot, S. Seidl, P. A. Dalgarno, R. J. Warburton, D. Granados, J. M. Garcia, K. Kowalik, O. Krebs, K. Karrai, A. Badolato, and P. M. Petroff. Manipulating exciton fine structure in quantum dots with a lateral electric field. *Appl. Phys. Lett.*, 90(4):88–91, 2007.

[94] Je-Hyung Kim, Tao Cai, Christopher J. K. Richardson, Richard P. Leavitt, and Edo Waks. Two-photon interference from a bright single-photon source at telecom wavelengths. *Optica*, 3(6):577–584, Jun 2016.

[95] Edward B. Flagg, Sergey V. Polyakov, Tim Thomay, and Glenn S. Solomon. Dynamics of nonclassical light from a single solid-state quantum emitter. *Phys. Rev. Lett.*, 109(16):1–5, 2012.

[96] Peter Michler. *Quantum dots for quantum information technologies*, volume 237. Springer, 2017.

[97] G. M. Gale and A. Mysyrowicz. Direct creation of excitonic molecules in CuCl by giant two-photon absorption. *Phys. Rev. Lett.*, 32(13):727–730, 1974.

[98] Q. Fu, D. Lee, A. Mysyrowicz, A. V. Nurmikko, R. L. Gunshor, and L. A. Kolodziejski. Excitonic molecules in ZnSe quantum wells. *Phys. Rev. B*, 37(15):8791–8794, 1988.

[99] Koch SW. Banyai L, Hu YZ, Lindberg M. Third-order optical nonlinearities in semiconductor microstructures L. 38(12):8142–8153, 1988.

[100] K. Brunner, G. Abstreiter, G. Bohm, G. Trankle and G. Weimann. Sharp-Line Photoluminescence and Two-Photon Absorption of Zero-Dimensional Biexcitons in a GaAs/AlGaAs Structure. *Appl. Phys. Lett.*, 20(4):1830, 2004.

[101] Bernd Hönerlage, R Levy, JB Grun, C Klingshirn, and K Bohnert. The dispersion of excitons, polaritons and biexcitons in direct-gap semiconductors. *Physics Reports*, 124(3):161–253, 1985.

[102] S. Stufler, P. Machnikowski, P. Ester, M. Bichler, V. M. Axt, T. Kuhn, and A. Zrenner. Two-photon Rabi oscillations in a single Inx Ga1-x As GaAs quantum dot. *Phys. Rev. B - Condens. Matter Mater. Phys.*, 73(12):1–7, 2006.

[103] Ana Predojević. Resonant excitation and photon entanglement from semiconductor quantum dots. In *Engineering the Atom-Photon Interaction*, pages 303–324. Springer, 2015.

[104] A. J. Ramsay, T. M. Godden, S. J. Boyle, E. M. Gauger, A. Nazir, B. W. Lovett, A. M. Fox, and M. S. Skolnick. Phonon-induced Rabi-frequency renormalization of optically driven single InGaAs/GaAs quantum dots. *Phys. Rev. Lett.*, 105(17):1–4, 2010.

[105] S. Lüker, K. Gawarecki, D. E. Reiter, A. Grodecka-Grad, V. M. Axt, P. MacHnikowski, and T. Kuhn. Influence of acoustic phonons on the optical control of quantum dots driven by adiabatic rapid passage. *Phys. Rev. B - Condens. Matter Mater. Phys.*, 85(12):2–5, 2012.

[106] A. J. Ramsay, Achanta Venu Gopal, E. M. Gauger, A. Nazir, B. W. Lovett, A. M. Fox, and M. S. Skolnick. Damping of exciton rabi rotations by acoustic phonons in optically excited InGaAs/GaAs quantum dots. *Phys. Rev. Lett.*, 104(1):20–23, 2010.

[107] M. Glässl, A. M. Barth, and V. M. Axt. Proposed robust and high-fidelity preparation of excitons and biexcitons in semiconductor quantum dots making active use of phonons. *Phys. Rev. Lett.*, 110:147401, Apr 2013.

[108] J. H. Quilter, A. J. Brash, F. Liu, M. Glässl, A. M. Barth, V. M. Axt, A. J. Ramsay, M. S. Skolnick, and A. M. Fox. Phonon-assisted population inversion of a single InGaAs/GaAs quantum dot by pulsed laser excitation. *Phys. Rev. Lett.*, 114:137401, Mar 2015.

[109] Marcus Reindl, Klaus D. Jöns, Daniel Huber, Christian Schimpf, Yongheng Huo, Val Zwiller, Armando Rastelli, and Rinaldo Trotta. Phonon-Assisted Two-Photon Interference from Remote Quantum Emitters. *Nano Letters*, 17(7):4090–4095, 2017.

[110] M. Glässl, A. M. Barth, K. Gawarecki, P. MacHnikowski, M. D. Croitoru, S. Lüker, D. E. Reiter, T. Kuhn, and V. M. Axt. Biexciton state preparation in a quantum dot via adiabatic rapid passage: Comparison between two control protocols and impact of phonon-induced dephasing. *Phys. Rev. B - Condens. Matter Mater. Phys.*, 87(8):1–8, 2013.

[111] Timo Kaldewey, Sebastian Lüker, Andreas V Kuhlmann, Sascha R Valentin, Arne Ludwig, Andreas D Wieck, Doris E Reiter, Tilmann Kuhn, and Richard J Warburton. Coherent and robust high-fidelity generation of a biexciton in a quantum dot by rapid adiabatic passage. *Phys. Rev. B*, 95(16):1–5, 2017.

[112] Scarani, V., de Riedmatten, H., Marcikic, I., Zbinden, H., and Gisin, N. Four-photon correction in two-photon bell experiments. *Eur. Phys. J. D*, 32(1):129–138, 2005.

[113] Xi-Lin Wang, Luo-Kan Chen, W. Li, H.-L. Huang, C. Liu, C. Chen, Y.-H. Luo, Z.-E. Su, D. Wu, Z.-D. Li, H. Lu, Y. Hu, X. Jiang, C.-Z. Peng, L. Li, N.-L. Liu, Yu-Ao Chen, Chao-Yang Lu, and Jian-Wei Pan. Experimental ten-photon entanglement. *Phys. Rev. Lett.*, 117:210502, Nov 2016.

[114] Daniel Huber, Marcus Reindl, Johannes Aberl, Armando Rastelli, and Rinaldo Trotta. Semiconductor quantum dots as an ideal source of polarization-entangled photon pairs on-demand: a review. *Journal of Optics*, 20(7):073002, Jun 2018.

[115] Hui Wang, Hai Hu, T.-H. Chung, Jian Qin, Xiaoxia Yang, J.-P. Li, R.-Z. Liu, H.-S. Zhong, Y.-M. He, Xing Ding, Y.-H. Deng, Qing Dai, Y.-H. Huo, Sven Höfling,

Chao-Yang Lu, and Jian-Wei Pan. On-demand semiconductor source of entangled photons which simultaneously has high fidelity, efficiency, and indistinguishability. *Phys. Rev. Lett.*, 122:113602, Mar 2019.

[116] E. Moreau, I. Robert, L. Manin, V. Thierry-Mieg, J. M. Gérard, and I. Abram. Quantum cascade of photons in semiconductor quantum dots. *Phys. Rev. Lett.*, 87:183601, Oct 2001.

[117] R. Seguin, A. Schliwa, S. Rodt, K. Pötschke, U. W. Pohl, and D. Bimberg. Size-dependent fine-structure splitting in self-organized InAs/GaAs quantum dots. *Phys. Rev. Lett.*, 95:257402, Dec 2005.

[118] Stefan Seidl, Martin Kroner, Alexander Högele, Khaled Karrai, Richard J. Warburton, Antonio Badolato, and Pierre M. Petroff. Effect of uniaxial stress on excitons in a self-assembled quantum dot. *Appl. Phys. Lett.*, 88(20):203113, 2006.

[119] Gabriel Bester, Selvakumar Nair, and Alex Zunger. Pseudopotential calculation of the excitonic fine structure of million-atom self-assembled $In_{1-x}Ga_xAs$/GaAs quantum dots. *Phys. Rev. B*, 67:161306, Apr 2003.

[120] T. M. Stace, G. J. Milburn, and C. H. W. Barnes. Entangled two-photon source using biexciton emission of an asymmetric quantum dot in a cavity. *Phys. Rev. B*, 67:085317, Feb 2003.

[121] Gediminas Juska, Valeria Dimastrodonato, Lorenzo O. Mereni, Agnieszka Gocalinska, and Emanuele Pelucchi. Towards quantum-dot arrays of entangled photon emitters. *Nat Photon*, 7(7):527–531, July 2013.

[122] K. Kowalik, O. Krebs, A. Lemaître, S. Laurent, P. Senellart, P. Voisin, and J. A. Gaj. Influence of an in-plane electric field on exciton fine structure in inas-gaas self-assembled quantum dots. *Appl. Phys. Lett.*, 86(4):041907, 2005.

[123] Andreas Muller, Wei Fang, John Lawall, and Glenn S. Solomon. Creating polarization-entangled photon pairs from a semiconductor quantum dot using the optical stark effect. *Phys. Rev. Lett.*, 103:217402, Nov 2009.

[124] W. Langbein, P. Borri, U. Woggon, V. Stavarache, D. Reuter, and A. D. Wieck. Control of fine-structure splitting and biexciton binding in $In_xGa_{1-x}As$ quantum dots by annealing. *Phys. Rev. B*, 69:161301, Apr 2004.

[125] P. E. Kremer, A. C. Dada, P. Kumar, Y. Ma, S. Kumar, E. Clarke, and B. D. Gerardot. Strain-tunable quantum dot embedded in a nanowire antenna. *Phys. Rev. B*, 90:201408, 2014.

[126] Mathieu Munsch, Nitin S. Malik, Emmanuel Dupuy, Adrien Delga, Joël Bleuse, Jean-Michel Gérard, Julien Claudon, Niels Gregersen, and Jesper Mørk. Dielectric GaAs antenna ensuring an efficient broadband coupling between an InAs quantum dot and a gaussian optical beam. *Phys. Rev. Lett.*, 110:177402, 2013.

[127] Hui Wang, Yu He, Yu-Huai Li, Zu-En Su, Bo Li, He-Liang Huang, Xing Ding, Ming-Cheng Chen, Chang Liu, Jian Qin, Jin-Peng Li, Yu-Ming He, Christian Schneider, Martin Kamp, Cheng-Zhi Peng, Sven Höfling, Chao-Yang Lu, and Jian-Wei Pan. High-efficiency multiphoton boson sampling. *Nat Photon*, 11(6):361–365, June 2017.

[128] Xiang-Bin Wang, Cheng-Xi Yang, and Yan-Bing Liu. On-demand entanglement source with polarization-dependent frequency shift. *Appl. Phys. Lett.*, 96(20):201103, 2010.

[129] W. A. Coish and J. M. Gambetta. Entangled photons on demand: Erasing which-path information with sidebands. *Phys. Rev. B*, 80:241303, Dec 2009.

[130] M. Metcalfe, S. M. Carr, A. Muller, G. S. Solomon, and J. Lawall. Resolved sideband emission of InAs/GaAs quantum dots strained by surface acoustic waves. *Phys. Rev. Lett.*, 105:037401, Jul 2010.

[131] Zong-Quan Zhou, Chuan-Feng Li, Geng Chen, Jian-Shun Tang, Yang Zou, Ming Gong, and Guang-Can Guo. Phase compensation enhancement of photon pair entanglement generated from biexciton decay in quantum dots. *Phys. Rev. A*, 81:064302, Jun 2010. FSS, compensation.

[132] A. J. Hudson, R. M. Stevenson, A. J. Bennett, R. J. Young, C. A. Nicoll, P. Atkinson, K. Cooper, D. A. Ritchie, and A. J. Shields. Coherence of an entangled exciton-photon state. *Phys. Rev. Lett.*, 99:266802, Dec 2007.

[133] E. Poem, Y. Kodriano, C. Tradonsky, N. H. Lindner, B. D. Gerardot, P. M. Petroff, and D. Gershoni. Accessing the dark exciton with light. *Nat Phys*, 6(12):993–997, December 2010.

[134] Charles Santori, David Fattal, Matthew Pelton, Glenn S. Solomon, and Yoshihisa Yamamoto. Polarization-correlated photon pairs from a single quantum dot. *Phys. Rev. B*, 66:045308, Jul 2002.

[135] N. Akopian, N. H. Lindner, E. Poem, Y. Berlatzky, J. Avron, D. Gershoni, B. D. Gerardot, and P. M. Petroff. Entangled photon pairs from semiconductor quantum dots. *Phys. Rev. Lett.*, 96:130501, Apr 2006.

[136] N. Akopian, N. H. Lindner, E. Poem, Y. Berlatzky, J. Avron, D. Gershoni, B. D. Gerardot, and P. M. Petroff. Correlated and entangled pairs of single photons from semiconductor quantum dots. *J. Appl. Phys.*, 101(8):081712, 2007.

[137] P. Page and H. Pursey. Tunable single sideband electro-optic ring modulator. *Opto-electronics*, 2(1):1–4, 1970.

[138] G. H. Smith, D. Novak, and Z. Ahmed. Technique for optical ssb generation to overcome dispersion penalties in fibre-radio systems. *Electron. Lett.*, 33(1):74–75, Jan 1997.

[139] Chuan Qin, Hongbo Lu, Burcu Ercan, Siwei Li, and SJ Ben Yoo. Single-tone optical frequency shifting and nonmagnetic optical isolation by electro-optical emulation of a rotating half-wave plate in a traveling-wave lithium niobate waveguide. *IEEE Photonics Journal*, 9(3):1–13, 2017.

[140] Peng Gangding, Huang Shangyuan, and Lin Zonggi. Application of electro-optic frequency shifters in heterodyne interferometric systems. *Electron. Lett.*, 22(23):1215–1216, November 1986.

[141] R. Noe and D. A. Smith. Integrated-optic rotating waveplate frequency shifter. *Electron. Lett.*, 24(21):1348–1349, Oct 1988.

[142] WM Young, RS Feigelson, Martin M Fejer, Michel JF Digonnet, and Herbert J Shaw. Photorefractive-damage-resistant zn-diffused waveguides in mgo: Linbo 3. *Optics letters*, 16(13):995–997, 1991.

[143] Daley, Simon. Electro-optic rotating half-waveplate for a quantum dot fine-structure eraser, 2019.

[144] Nicolas Sangouard, Christoph Simon, Hugues De Riedmatten, and Nicolas Gisin. Quantum repeaters based on atomic ensembles and linear optics. *Reviews of Modern Physics*, 83(1):33, 2011.

[145] A. G. Radnaev, Y. O. Dudin, R. Zhao, H. H. Jen, S. D. Jenkins, A. Kuzmich, and T. A.B. Kennedy. A quantum memory with telecom-wavelength conversion. *Nat. Phys.*, 6(11):894–899, 2010.

[146] Jian-Wei Pan, Dik Bouwmeester, Harald Weinfurter, and Anton Zeilinger. Experimental entanglement swapping: entangling photons that never interacted. *Physical Review Letters*, 80(18):3891, 1998.

[147] B. J. Skromme, T. S. Low, T. J. Roth, G. E. Stillman, J. K. Kennedy, and J. K. Abrokwah. Residual donors and acceptors in high-purity GaAs and InP grown by hydride VPE. *J. Electron. Mater.*, 12(2):433–457, Mar 1983.

[148] Kevin Lan and James W. Jorgenson. A hybrid of exponential and gaussian functions as a simple model of asymmetric chromatographic peaks. *Journal of Chromatography A*, 915(1):1 – 13, 2001.

[149] T. Fokkens, A. Fognini, and V. Zwiller, 2016. Waveplates Library, available at GitHub.

[150] Daniel A Steck. Classical and modern optics. *course notes available online at http://steck. us/teaching*, 2006.

Appendix A

Supplementary information for Chapter3

A.1 Power Dependence of Exciton and Biexciton

Fig. A.1 (a) depicts the power dependent $g^{(2)}$ of the exciton excited at 870 nm, and Fig. A.1 (b) shows the same for the biexciton line. The single photon purity of the exciton lies below 1 %, even above saturation, whereas for the biexciton it saturates at 10 % because of reexcitation. Fig. A.1 (c) shows the detected count rates of the X and XX line at 830 nm excitation as a function of excitation power. The numbers indicate the slopes of the curves in the log-log graph, which are close to what is expected (slope of 1 for the exciton and 2 for the biexciton). Fig. A.1 (d) shows the detected count rates for X and XX in the case of 870 nm excitation as a function of excitation power. Here, the slopes as well as the saturation behavior differ from Fig. A.1 (c). The slopes are smaller and the saturation is less pronounced. In case of non-resonant excitation at the saturation power the single photon purity of the exciton is still below 1 % and the biexciton yields $g^{(2)}_{XX} = 0.1$.

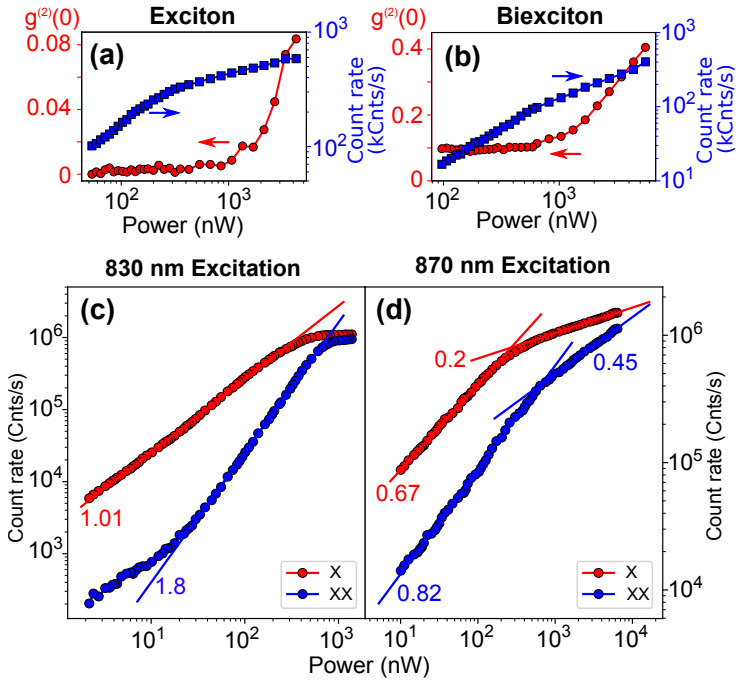

Figure A.1: Power dependence of the $g^{(2)}(0)$ excited at quasi resonance (870 nm) for **(a)** the exciton, and **(b)** the biexciton. **(c)** Power dependence dependent count rates of the exciton and the biexciton line at non-resonant excitation (830 nm). **(d)** Power dependent count rates of the exciton and the biexciton line at quasi-resonant excitation (870 nm). The numbers next to the lines indicate the slope on the log-log plot.

A.2 Quantum Dot Characteristics

The QD spectrum changed considerably by tuning from non-resonant excitation (830 nm) to quasi-resonant (870 nm), compare Fig. 1 in the main text.

We wanted to know whether the line at which we excited at 870 nm originated from the QD's p-shell or from donor/acceptor exciton transitions [147] within the InP nanowire. We investigated this question by exciting the QD at low power ($\sim$ 15nW) at 820 nm. If it was a p-shell transition the line should disappear since an exciton in the p-shell would immediately relax to the s-shell. In our case, we still see the line at low power indicative for a donor/acceptor exciton transition [147]. This implies that we did not excite directly at the p-level. This conclusion is further corroborated by cross-correlation measurements where we found that all of the emission lines around 870 nm were uncorrelated with the QD s-shell.

We further investigated the dynamics of the InAsP QD at quasi-resonance by performing cross-correlations between all of the emission lines in the QD s-shell. Fig. A.2 shows the result of the cross-correlations between X, XX, X^-, and X^+. The cascades were fitted using an exponential-Gaussian hybrid [148]. In each cascade the area of the center peak was compared to the average area of the side peaks (uncorrelated coincidence counts) by calculating their ratio. We have defined the area as the part until the curve falls below the full width at half maximum (FWHM) point. In this way, we can circumvent problems when the lifetime overlaps with the adjacent peak (e.g. Fig. A.2 (e)). These measurements imply that the holes are trapped at a higher rate than electrons. This finding is in agreement with our sample being unintentionally n-doped whereby the QD's s-level is already filled with electrons without laser excitation.

In summary we find:

1. The lines at 870 nm are not p-shell resonances from the QD, but donor/acceptor exciton transitions [147] within the wurtzite InP nanowire.

2. Both electrons and/or holes get trapped in the QD after a radiative decay.

3. Holes are trapped faster than electrons as indicated by the shorter decay time of 0.81 ns in Fig. A.2 (d) as compared to 5.5 ns in Fig. A.2 (e).

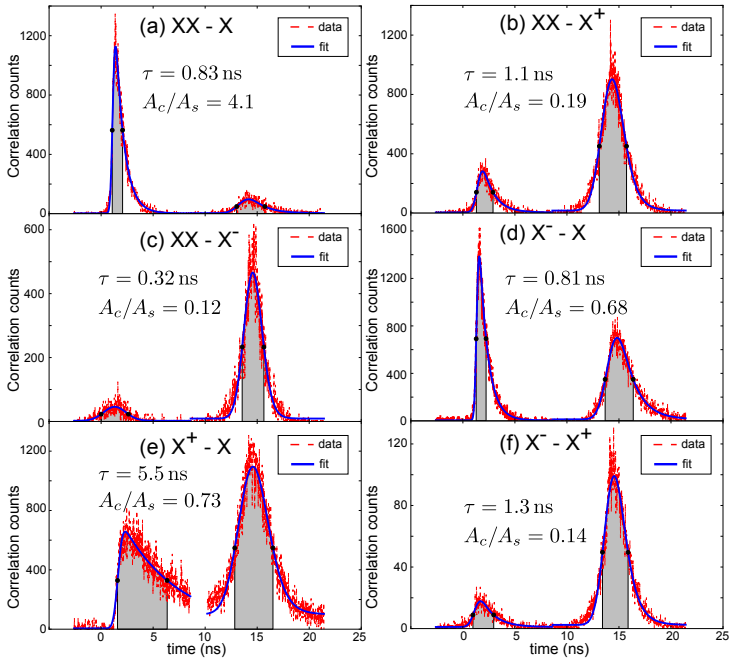

Figure A.2: In all figures τ is the time scale of the decay and A_c is the area in the FWHM region for the central peak, whereas A_s is the area in the FWHM region for the side peak. **(a)** Shows the $XX - X$ cascade as a reference. **(b)** Shows the cascade between XX and X^+ (starting on XX and stopping on X^+). This shows that after the emission of XX, in a time scale of about 1 ns, a hole can get trapped in the QD. **(c)** Depicts the cross-correlation between the XX and X^-. It suggests that the trapping of an electron after a XX decay is almost equally likely as a hole, compare (b). **(d)** Shows cross-correlations between X^- and X. **(e)** Shows the correlations between X^+ and X. Comparing this graph with (d) indicates that the rate at which electrons get trapped is slower than holes (0.83 ns compared to 5.5 ns). **(f)** Shows the X^- to X^+ cross-correlations. The numbers indicate that the process of trapping two holes within the laser repetition rate is suppressed. In all panels the first state is the start photon and the second state is the stop photon for the cross-correlation measurements.

A.3 Tomography Setup Calibration

The quantum state tomography setup was built according to Ref. [84], compare Fig. A.3. A crucial part before performing the correlation measurements is the calibration of the waveplates and polarizers. Any miscalibration reduces the quality of the quantum state tomography.

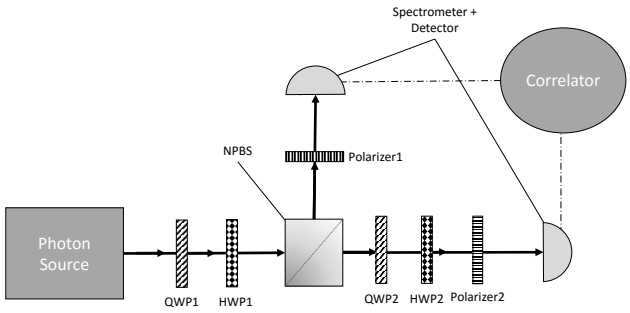

Figure A.3: Schematic view of the setup used to analyze the entangled photon pairs following Ref. [84]. The setup includes a pair of polarizers, a pair of half-waveplates (HWPs), a pair of quarter-waveplates (QWPs), a non-polarizing beam splitter (NPBS), a pair of spectrometers, single photon detectors, and finally a correlator to build the histogram from the signals of the detectors. The two polarizers are set to H polarization.

The calibration was performed in three steps:

1. **Polarization reference:** A polarizing beamsplitter served as the vertical polarization (V) reference. It was directly placed on the optical table and aligned carefully along the incoming laser beam (870 nm). In this case it only transmitted V-polarized light and we used it as the polarization reference for the polarizer calibration.

2. **Polarizer calibration:** The polarizers were calibrated to H-polarization (defined to be parallel to the optical table). The polarizers were adjusted until the V-polarized light transmission was minimal.

3. **Waveplate calibration:** Each of the two $\lambda/2$ and $\lambda/4$-waveplates were calibrated individually to find their zero-point. They were placed between the polarizing beam-splitter and the aligned polarizer. They were rotated till minimal light transmission through the polarizer was achieved which is their zero-point.

To test the waveplate's and polarizer's calibration we performed state tomography in all 36 bases (HH, HV, ...) on classical H-polarized laser light (870 nm). The measurement result is depicted in Fig. A.4 and shows only a clean peak at $|HH\rangle\langle HH|$ highlighting a very good calibration of our tomography setup. The fidelity between the measured density matrix and the density matrix describing purely H polarized light is 0.993. This very high number (in the ideal case one) reveals a very well aligned setup.

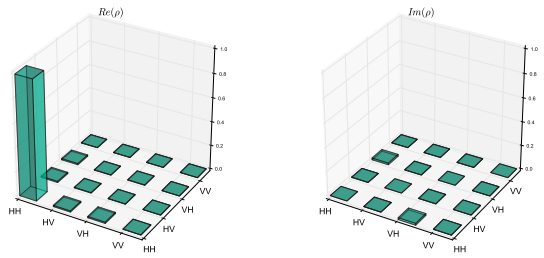

Figure A.4: Tomography of H polarized laser pulses. The fidelity between the measured density matrix and a density matrix describing purely H polarized light is 0.993.

The waveplate settings to perform the 36 bases quantum tomography are listed in Table A.1. They were calculated based on Ref. [149].

Table A.1: Summarizing all waveplate angle settings in degrees used to perform the full set of correlation measurements. Here, QP and HP are the abbreviations for $\lambda/4$- and $\lambda/2$-waveplates, respectively. The subscript numbers match the numbers in the setup schematic, compare Fig. A.3.

Basis	**QP**$_1$	**HP**$_1$	**QP**$_2$	**HP**$_2$	**Basis**	**QP**$_1$	**HP**$_1$	**QP**$_2$	**HP**$_2$
HH	0	0	0	0	HV	0	0	0	45
HD	0	0	−45	0	HA	0	0	0	−22.5
HR	0	0	−45	−22.5	HL	0	0	−45	22.5
VH	0	45	0	45	VV	0	45	0	0
VD	0	45	−45	0	VA	0	45	0	−22.5
VR	0	45	−45	22.5	VL	0	45	−45	−22.5
DH	−45	22.5	−45	0	DV	−45	22.5	0	−22.5
DD	−45	22.5	0	0	DA	−45	22.5	0	45
DR	−45	22.5	−45	22.5	DL	−45	22.5	−45	−22.5
AH	−45	−22.5	−45	0	AV	−45	−22.5	0	−22.5
AD	−45	−22.5	0	45	AA	−45	−22.5	0	0
AR	−45	−22.5	−45	−22.5	AL	−45	−22.5	−45	22.5
RH	−45	0	−45	0	RV	−45	0	0	−22.5
RD	−45	0	−45	−22.5	RA	−45	0	−45	22.5
RR	−45	0	0	0	RL	−45	0	0	45
LH	0	−22.5	−45	−22.5	LV	0	−22.5	−45	22.5
LD	0	−22.5	−45	0	LA	0	−22.5	0	−22.5
LR	0	−22.5	0	45	LL	0	−22.5	0	0

A.4 Correlation Measurements

Fig. A.5, A.6, and A.7 depict the raw data of all 36 correlation measurements used for the quantum state tomography shown in Fig. 2, 4 (a), and 4 (b) in the main text, respectively. The data was recorded with 16 ps time bins.

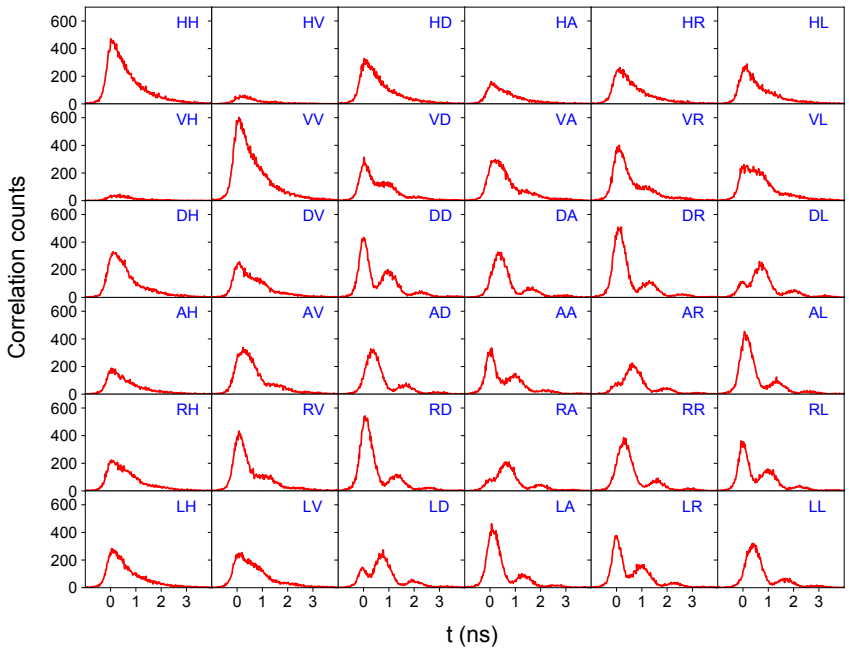

Figure A.5: Quasi-resonant excitation at 870 nm was employed. The figure depicts the raw data used for the quantum state tomography measurements presented in Fig. 2 of the main text. The integration time per basis was 370 s.

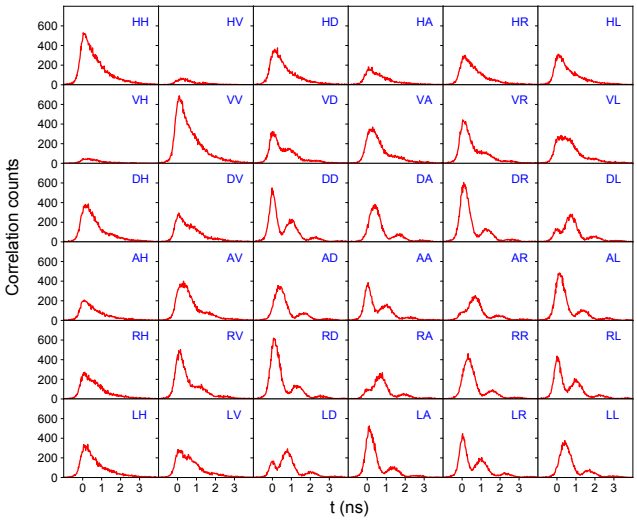

Figure A.6: Quasi-resonant excitation at 870 nm was employed. The figure depicts the raw data used for the quantum state tomography measurements presented in Fig. 4 (a) of the main text. The integration time per basis was 342 s.

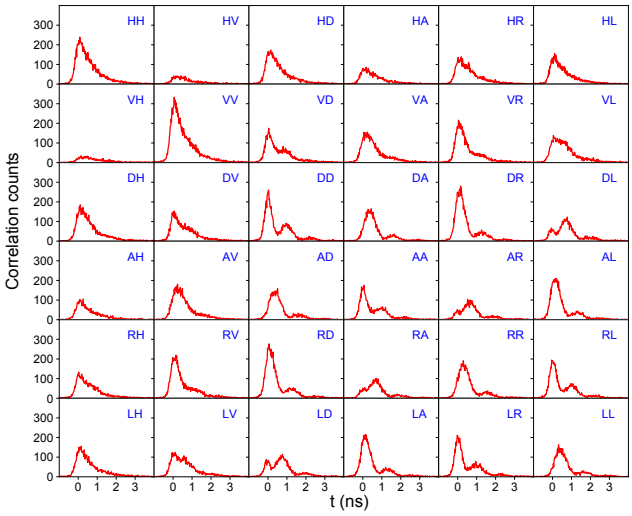

Figure A.7: Non-resonant excitation at 830 nm. The figure depicts the raw data used for the quantum state tomography measurements presented in Fig. 4 (b) of the main text. The integration time per basis was 342 s.

A.5 Birefringence

Previous studies on InAsP/InP nanowire quantum dots [85, 84] have shown the effect of birefringence in the nanowire on the quantum state. We investigated if this is also the case in our nanowire. We applied a magnetic field of 4 T along the nanowire's growth direction and analyzed the polarization state of the split exciton (X) and biexciton line (XX).

In case of no birefringence, we expect the Zeeman-split lines to be fully circularly polarized because of angular momentum conservation. Fig. A.8 depicts the photoluminescence (PL) recorded at 830 nm excitation and an applied magnetic field of 4 T. The red line shows the PL when the polarization analyzer only passed right polarized (R) photons and the dashed blue line if the analyzer only passed left polarized (L) photons. We observe that the Zeeman-split lines are either R- or L-polarized, compare Tab. A.2 for the extinction ratio values. This shows that our investigated nanowire induces an insignificant amount of

birefringence.

This implies that we expect to measure a quantum state of the form

$$|\Psi\rangle = \frac{1}{\sqrt{2}}\left(|RL\rangle + |LR\rangle\right) = \frac{1}{\sqrt{2}}\left(|HH\rangle + |VV\rangle\right), \tag{A.1}$$

in the case of no fine-structure splitting.

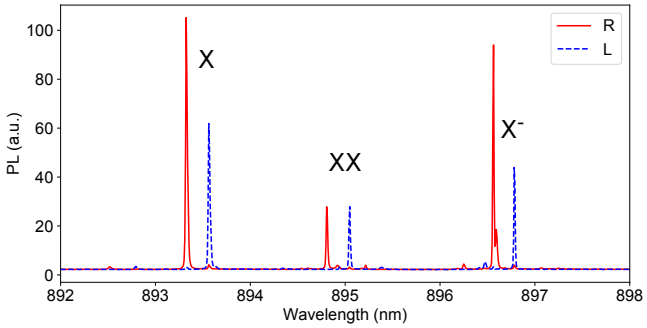

Figure A.8: Excitation at 830 nm with an applied magnetic field of 4 T along the nanowire's growth direction. The exciton (X), the biexciton (XX), and the trion (X^-) split in two lines.

Table A.2: Polarization extinctions for the exciton (X) and biexciton (XX) lines shown in Fig. A.8. The extinction ratio is defined here as the power of the suppressed peak divided by the power of the cross-polarized peak.

Peak	**Extinction ratio in %**
X Left	1.03 ± 0.03
X Right	3.32 ± 0.08
XX Left	0.85 ± 0.06
XX Right	3.76 ± 0.12

A.6 Detector Time Resolution Function

The simulation crucially depends on the used detection system's time resolution function $g(t)$. It cannot be measured with picosecond laser pulses as these pulses are spectrally too different from the QD's emission profile. The reason is that chirp introduced at the spectrometer's gratings changes the pulse length too much in case of short laser pulses. The only valid way to extract the detection time resolution function is directly from the set of correlation measurements. Namely, the rising part of the correlations without oscillations, e.g., the HH and VV correlations, allow the extraction of the system's time resolution function $g(t)$. The HH and VV correlation counts are of the form

$$f(t) = \Theta(t)e^{-t/\tau_X} * g(t), \tag{A.2}$$

where, $\Theta(t)$ is the Heaviside function, τ_X the exciton lifetime, and $*$ denotes the convolution operator. To simplify the deconvolution process we can approximate equation A.2 around time zero as

$$f(t) \approx \Theta(t) * g(t). \tag{A.3}$$

This approach is valid when the half width at half maximum of $g(t)$ ($\sim 100\,\mathrm{ps}$) is smaller than τ_X (847 ps). This is fulfilled in our case. The differentiation of $f(t)$ in equation A.3 will then directly yield $g(t)$.

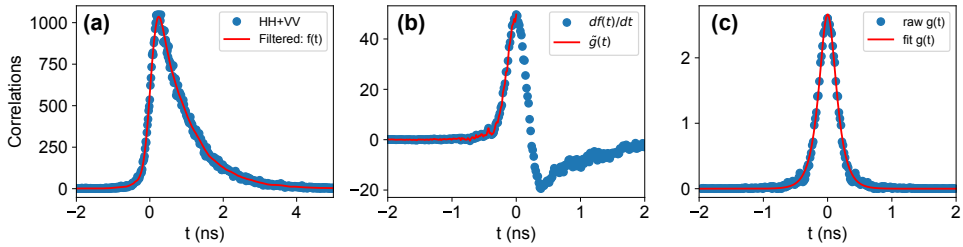

Figure A.9: Procedure to acquire the detection system's time resolution function $g(t)$ in order to perform the simulate the concurrence evolution shown in Fig. 2 of the main text. **(a)** The sum of the HH and VV correlations (dots) are smoothed with a Savitzki-Golay filter (red curve) with a polynomial of degree 6 and a window length of 65. **(b)** The filtered correlation data is numerically differentiated (dots) and the part till the maximum (red curve) is the rising part of $g(t)$. **(c)** The dots represent the mirrored $\tilde{g}(t)$. $\tilde{g}(t)$ is fitted with the function from Eq.A.5 and depicted with the red line. A perfect fit is achieved with an R^2-value of 0.998.

Numerically we performed the following algorithm: The sum of HH and VV correlation yields a better signal to noise ratio than only HH or VV alone. Therefore, we use

$$\tilde{f}(t) = HH + VV. \tag{A.4}$$

Since $\tilde{f}(t)$ is subjected to noise we use use a Savitzki-Golay filter to smoothen $\tilde{f}(t)$ and yield $f(t)$. This procedure is depicted in Fig. A.9 (a). As a next step we perform a numerical stepwise differentiation of $f(t)$ and yield the data in Fig. A.9 (b). From $df(t)/dt$ we consider the part from negative times until the maximum, which we call $\tilde{g}(t)$. This function contains the full information of the detection time resolution function $g(t)$. In our case $g(t)$ is a symmetric function since both APDs show the same impulse response, see Fig. A.10.

Therefore, we can reconstruct the raw $g(t)$ by mirroring $\tilde{g}(t)$ along its maximum, see Fig. A.9 (c). Since the raw $g(t)$ is subjected to noise we fit it with

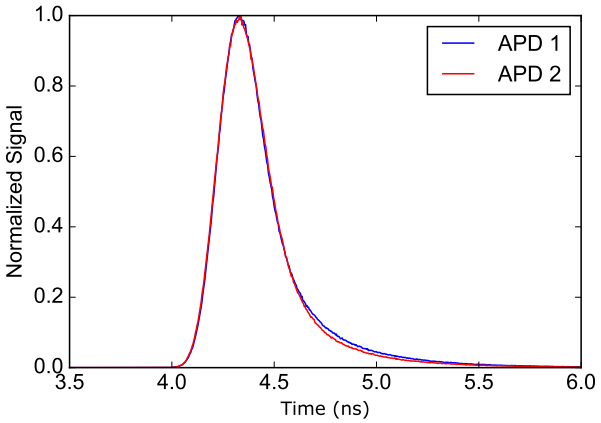

Figure A.10: APD responses to picosecond laser pulses (center wavelength 870 nm) measured after the spectrometers tuned to the laser wavelength. The two APDs have a mostly congruent pulse shape which justifies the assumption of a symmetric detection response function $g(t)$. The full width at half maximum is for both pulses 290 ps.

$$g_f(t, t_0, a, \sigma) = \frac{a}{\left(\cosh\left(\frac{t-t_0}{\sigma}\right)\right)^2} \tag{A.5}$$

where a is the amplitude, and t_0 the time origin. The fit to the data is in excellent agreement, compare Fig. A.9 (c). By normalizing g_f we yield the detection system's time resolution function as

$$g(t) = \frac{g_f(t)}{\int_{-\infty}^{\infty} g_f(t)dt}. \tag{A.6}$$

Based on $g(t)$ the simulation is performed as described in the main text. This procedure has been applied for all the simulation in the text with a Savitzki-Golay filter with a polynomial of degree 6 and a window length of 65. For the data presented in Fig. 2 of the main text the fit's R^2-value is 0.998.

A.7 Count Averaged Concurrence

The count averaged concurrence $\bar{\mathcal{C}}$ in the text is defined as:

$$\bar{\mathcal{C}} := \frac{\sum_{t_k} N^{t_k} \mathcal{C}\left(\rho\left(ij^{t_k}\right)\right)}{\sum_{t_k} N^{t_k}}, \tag{A.7}$$

where $\rho(ij^{t_k})$ is the density matrix based on the correlation counts ij^{t_k} within a time bin at time t_k ($i, j \in \{H, V, D, A, R, L\}$), $\mathcal{C}$ denotes the concurrence [60], and N_{t_k} is the total correlation counts within a time bin at time index t_k, $N^{t_k} = \sum_{i,j} ij^{t_k}$.

Appendix B

Supporting information for Chapter4

B.1 Experimental Setup

In order to perform the resonant TPE scheme, proper steps have to be taken in order to suppress the excitation laser light reflected off of the sample surface. Since the intensity of the laser is orders of magnitude greater than that of the emitted photons, the reflected light will saturate the spectrometers' and distinguishing the photons from the excitation pulse becomes impossible. One way to overcome this challenge, is to excite in one polarization, e.g., H, and collect photons in the perpendicular polarization, V. This way, a huge portion of the reflected laser light will be blocked by a polarizer set at a polarization perpendicular to that of the incoming laser pulse. Moreover, spacial filtering is also necessary in order to achieve a clean emission background in the spectrum. The emitted photons from nanowire QDs exhibit a Gaussian profile [30] and can be coupled to a single-mode fiber (SMF) with high efficiency, however, the reflected light, as it is scattered off the surface of the sample, will couple to an SMF poorly. An schematic view of our experimental setup is shown in Fig. B.1. One polarizer sets the polarization of the laser pulse at H, and a combination of a half-wave plate and a second polarizer acts as a control for the input power. On the collection side, a combination of the quarter-wave plate, half-wave plate and a polarizer rejects the reflected laser light, and a spacial filtering via an SMF further

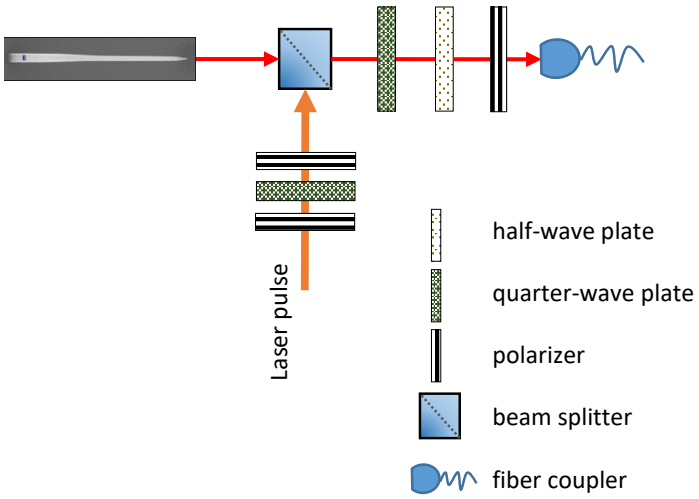

Figure B.1: **Schematic view of the resonant TPE setup.** The excitation pulse is passed through a combination of two polarizers and one half-wave plate. The polarizers are set at H polarization. Rotation of the half-wave plate will control the excitation power. A combination of quarter-wave plate, half-wave plate, polarizer and an SMF will suppress the reflected laser light.

clears the background noise.

B.2 SMF coupling

In order to have a high efficiency coupling to the SMF, a proper choice for the lens in front of the SMF has to be made. Two factors has to be considered; first, the size of the beam at the focal point of the lens must match the mode field diameter (MFD) of the fiber, and second, the numerical aperture (NA) of the fiber must be at least greater than the NA of

the focused beam. In other words [150]:

$$\omega_{0,f} = \frac{\lambda f}{\pi \omega_{0,i}} < \text{MFD} \tag{B.1}$$

$$\text{NA}_l = \frac{\omega_{0,i}}{2f} < \text{NA}_{\text{SMF}}, \tag{B.2}$$

where, $\omega_{0,i}$ and $\omega_{0,f}$ are the waist size of the beam right before and at the focal point of the lens, respectively, λ is the wavelength of light, ≈ 894nm, f is the focal length of the lens, and NA_l and NA_{SMF} are the numerical apertures of the lens and the single-mode fiber, respectively. It is straightforward to realize the condition for a proper lens is:

$$\frac{\omega_{0,i}}{2\text{NA}_{\text{SMF}}} < f < \frac{\pi \omega_{0,i}}{\text{MFD}\lambda}. \tag{B.3}$$

By imaging the emission of our nanowire QD on a CCD, the diameter of the emitted beam is found to be $\omega_{0,i} \approx 0.75\text{mm} \pm 0.05\text{mm}$. For the fiber used in our setup $\text{NA}_{\text{SMf}} = 0.13$, and $\text{MFD} = 5\mu\text{m}$. Thus the focal length of the lens falls in the range $5\text{mm} < f < 26.2\text{mm}$. Considering all the components, we have reached a setup transmission efficiency of $\epsilon = 0.27\%$.

Appendix C

Supporting information for Chapter5

To understand in detail the compensation procedure the typical equation of the entangled state with finestructure splitting δ, written as

$$\Psi(t,\delta) = \frac{1}{\sqrt{2}}\left(HH + e^{-i\frac{\delta}{\hbar}t}VV\right), \tag{C.1}$$

needs to be rewritten in terms of creation operators $a^{\dagger}_{z,k,\lambda}$ since equation C.1 is ambiguous about the time ordering of the excitons (biexciton is emitted before the exciton) and their energies. The first index of the creation operator z represent the position of the photon perpendicular to waveplate orientation, k the wave vector, and λ the polarization state. For the sake of clarity and taking in to account the actual experimental implementation, we only consider photons traveling perpendicular to the waveplate orientation and neglect any vector representation in the following. To capture the photon ordering the emission times of the biexciton t and the exciton t_X are introduced. The time t as in equation C.1 is defined as $t := t_X - t$. The energies of the excitons are described by their wave vectors k and k_X, respectively. For photons in vacuum the dispersion relation holds

$$E = \hbar\omega = \hbar kc, \tag{C.2}$$

with c the speed of light. Furthermore, for the sake of clarity the FSS is expressed as $\Delta k = \frac{\delta}{2\hbar c}$. With these definitions at hand we can write the entangled state in equation C.1

as

$$\Psi(z,t,t_X,k,k_X,\Delta k) = \frac{1}{\sqrt{2}}\left(a^\dagger_{z-tc,k+\Delta k,H}a^\dagger_{z-t_Xc,k_X-\Delta k,H} + a^\dagger_{z-tc,k-\Delta k,V}a^\dagger_{z-t_Xc,k_X+\Delta k,V}\right) \tag{C.3}$$

Which can be shown to be equal to equation C.1

$$\begin{aligned}\Psi(z,t,t_X,k,k_X,\Delta k) &= \frac{1}{\sqrt{2}}\left(a^\dagger_{z,k,H}e^{i(z\Delta k-tkc-t\Delta kc)}a^\dagger_{z,k_X,H}e^{i(-z\Delta k-t_Xk_Xc+t_X\Delta kc)}\right.\\ &\left.+\, a^\dagger_{z,k,H}e^{i(-z\Delta k-tkc+t\Delta kc)}a^\dagger_{z,k_X,H}e^{i(z\Delta k-t_Xk_Xc-t_X\Delta kc)}\right)\\ &= \frac{1}{\sqrt{2}}\left(a^\dagger_{z,k,H}a^\dagger_{z,k_X,H} + e^{-i2\Delta ktc}a^\dagger_{z,k,V}a^\dagger_{z,k_X,V}\right),\end{aligned} \tag{C.4}$$

where we have used the fact that overall phases can be factorized out.

Now we are ready to show the compensation procedure. As explained in the manuscript we first have to transform from H/V basis to R/L by means of two $\lambda/4$ plates. One $\lambda/4$ waveplate, represented by the operator $\Lambda_{1/4}$, will act on the XX and with an angle offset from the horizontal direction of $-\pi/4$ and the other on the X with an offset of $\pi/4$. In this way, horizontal and vertical polarization states are transformed to circular basis necessary for the compatibility with the the rotating $\lambda/2$ waveplate frequency shifter. In the following equation the action of the two $\lambda/4$ waveplates upon the quantum state C.3 is calculated:

$$\begin{aligned}\Phi(z,t,t_X,k,k_X,\Delta k) &= \Lambda_{1/4}(-\pi/4)\otimes\Lambda_{1/4}(\pi/4)\Psi(z,t,t_X,k,k_X,\Delta k)\\ &= \frac{1}{\sqrt{2}}\left(a^\dagger_{z,k,L}e^{i(z\Delta k-tkc-t\Delta kc)}a^\dagger_{z,k_X,R}e^{i(-z\Delta k-t_Xk_Xc+t_X\Delta kc)}\right.\\ &\left.+\, a^\dagger_{z,k,R}e^{i(-z\Delta k-tkc+t\Delta kc)}a^\dagger_{z,k_X,L}e^{i(+z\Delta k-t_Xk_Xc-t_X\Delta kc)}\right)\\ &= \frac{1}{\sqrt{2}}\left(a^\dagger_{z,k,L}a^\dagger_{z,k_X,R} + e^{-i2\Delta ktc}a^\dagger_{z,k,R}a^\dagger_{z,k_X,L}\right).\end{aligned} \tag{C.5}$$

For convenience we can in equation C.5 omit z and replace t and t_X with t, then the quantum state reads

$$\Phi(t,k,k_X,\Delta k) = \frac{1}{\sqrt{2}}\left(a^\dagger_{k,L}a^\dagger_{k_X,R} + e^{-i2\Delta ktc}a^\dagger_{k,R}a^\dagger_{k_X,L}\right). \tag{C.6}$$

The rotating $\lambda/2$-waveplate, represented by the operator

$$\Lambda_{1/2}(\omega) = \sum_k a^\dagger_{k+\frac{2\omega}{c},L}a_{k,R} + a^\dagger_{k-\frac{2\omega}{c},R}a_{k,L}, \tag{C.7}$$

where ω represents the angular rotation frequency, will consequently remove the effect of the finestructure splitting if $\omega = \frac{\delta}{4\hbar}$:

$$\begin{aligned}
\Xi(k,k_X) &= \Lambda_{1/2}\left(\frac{\delta}{4\hbar}\right)\otimes\Lambda_{1/2}\left(\frac{\delta}{4\hbar}\right)\Phi(z,t,t_X,k,k_X,\Delta k)\\
&= \Lambda_{1/2}\left(\frac{\delta}{4\hbar}\right)\otimes\Lambda_{1/2}\left(\frac{\delta}{4\hbar}\right)\frac{1}{\sqrt{2}}\left(a^\dagger_{z-tc,k+\Delta k,L}a^\dagger_{z-t_Xc,k_X-\Delta k,R}\right.\\
&\left.+\ a^\dagger_{z-tc,k-\Delta k,R}a^\dagger_{z-t_Xc,k_X+\Delta k,L}\right)\\
&= \frac{1}{\sqrt{2}}\left(a^\dagger_{z-tc,k,R}a^\dagger_{z-t_Xc,k_X,L} + a^\dagger_{z-tc,k,L}a^\dagger_{z-t_Xc,k_X,R}\right)\\
&= \frac{1}{\sqrt{2}}\left(a^\dagger_{z,k,R}a^\dagger_{z,k_X,L}e^{-ikt_Xc-ik_Xt_Xc} + a^\dagger_{z,k,L}a^\dagger_{z,k_X,R}e^{-ikt_Xc-ik_Xt_Xc}\right)\\
&= \frac{1}{\sqrt{2}}\left(a^\dagger_{z,k,R}a^\dagger_{z,k_X,L} + a^\dagger_{z,k,L}a^\dagger_{z,k_X,R}\right).
\end{aligned} \tag{C.8}$$

The last line in equation C.8 is a fully entangled state without FSS in circular basis. Therefore, it is not yet precisely the starting state as described in equation C.1 without the exponential phase term. But with the addition of two $\lambda/4$-waveplates the state can be translated in to H/V basis and is then equivalent to our initial state described in equation C.1 without FSS:

$$\Lambda_{1/4}(-\pi/4)\otimes\Lambda_{1/4}(\pi/4)\,\Xi(k,k_X) = \frac{1}{\sqrt{2}}\left(a^\dagger_{z,k,H}a^\dagger_{z,k_X,H} + a^\dagger_{z,k,V}a^\dagger_{z,k_X,V}\right). \tag{C.9}$$